

國立交通大學

光電工程研究所

博士論文

雙光纖探針近場光學頭於儲存系統的應用

**Dual-probe near-field fiber head  
for data storage applications**

研究生：方仁宇

指導教授：謝漢萍 教授

田仲豪 助理教授

中華民國九十六年十一月

# 雙光纖探針近場光學頭於儲存系統的應用

## Dual-probe near-field fiber head for data storage applications

研 究 生: 方仁宇  
指 導 教 授: 謝漢萍  
                  : 田仲豪

Candidate: Jen-Yu Fang  
Advisors: Han-Ping D. Shieh  
                  : Chung-Hao Tien



A DISSERTATION  
SUBMITTED TO THE GRADUATE SCHOOL  
IN PARTIAL FULFILLMENT OF THE REQUIREMENTS  
FOR THE DEGREE OF  
DOCTOR OF PHILOSOPHY  
IN  
INSTITUTE OF ELECTRO-OPTICAL ENGINEERING  
  
COLLEGE OF ELECTRICAL ENGINEERING  
NATIONAL CHIAO-TUNG UNIVERSITY

November 2007  
Hsinchu, Taiwan, R.O.C.

# 雙光纖探針近場光學頭於儲存系統的應用

博士研究生：方仁宇

指導教授：謝漢萍，田仲豪

國立交通大學 光電工程研究所

## 中文摘要

為了滿足儲存系統對於高效率高精度之近場光源的需求，本論文提出一新穎的雙光纖探針近場光學頭，此近場光學頭包含一個斜切的寫入端以及一個間隙感測端。



斜切的寫入端使用一個次波長 C 型微孔來產生一個次波長尺寸的近場光點以提高空間解析度。為提高次波長微孔的穿透率，本論文提出了一個創新的複合效應。藉由一特定偏振方向的入射光，照射於一被週期性溝槽所環繞的次波長光波導，或斜向照射於該次波長光波導上，可同時激發表面電漿波與傳播模態。被金屬薄膜所遮蔽之入射光可經由表面電漿波的傳遞，將能量傳遞至光波導的傳播模態，並促使在出射面上表面電漿波的激發。此複合效應可大幅增加次波長微孔的穿透率，模擬數據上顯示，其穿透率可較傳統圓孔高  $10^3$  以上。經由實驗亦證明，此複合效應的存在。遠場的穿透率量測顯示，此複合效應可比單一光波導，增加 1.3 到 1.9 倍；近場光強度分佈量測也顯示，出射峰值強度較單一光波導，提高 1.6 到 2.8 倍。

由於近場光源包含消散波，所以光學系統與儲存媒體的間隙必須維持在次波長

範圍內，通常在 100 nm 以內。因此藉由引入自混干涉效應，本論文使用一雷射半導體做為間隙感應器。首先我們模擬了雷射感應器的回饋訊號，並根據此訊號設計了一控制器。從實驗結果中得知，當一驅動表面有 4.8 $\mu\text{m}$  的位移時，此系統之殘留位置誤差低於 $\pm 1.5$  nm；當一旋轉碟片旋轉速度高達 1500rpm，並產生 16 $\mu\text{m}$  的位移時，此系統之殘留位置誤差可控制在 $\pm 9$  nm 內。

由於寫入端的高穿透率與感測端的高精度，本論文所提出的雙光纖探針近場光學頭具有高效率、精巧、簡單以及易於與其他系統整合的優勢，將可應用於資料儲存系統。而本論文所提出的複合效應與自混干涉效應，亦開啟了近場光學與近場伺服控制的新方向。



# Dual-probe near-field fiber head for data storage applications

Doctoral candidate: Jen-Yu Fang

Advisor: Dr. Han-Ping D. Shieh

and Dr. Chung-Hao Tien

Institute of Electro-Optical Engineering  
National Chiao Tung University

## Abstract

To meet demands of an efficient near-field light source with precisely active gap control in either magnetic or optical storage systems, we demonstrate a novel dual-probe fiber head with gap servo control. The fiber head consists of a straw-shaped writing probe for delivering optical power to the disk surface and a gap sensing probe for detecting the spacing between the probe and the disk surface.

The straw-shaped writing probe utilizes a C-shaped aperture in a metallic film on the end face to yield a near-field subwavelength spot. To break through the theoretic limit on the transmission through subwavelength apertures, we introduce a novel hybrid effect by illuminating the C-shaped aperture surrounded with a corrugated structure or with obliquely incident light. The light obstructed behind the film simultaneously excites surface plasmons waves and couples into propagation modes inside the aperture. The transmission of the straw-shaped writing probe employing the hybrid effect is  $10^3$  times higher than that of a conventional fiber probe. Compared to a single C-shaped aperture, the

far-field transmission measurement indicates that the hybrid effect results in further enhancement on the power throughput by a factor of 1.3 to 1.9. Near-field intensity distribution also shows that the signal amplitude is increased 1.6 to 2.8 times higher than that of a single C-shaped aperture.

Near-field optical systems increase spatial resolution by employing evanescent waves, so the spacing between the optical device and the medium surface must be maintained within a wavelength, typically less than 100 nm. By employing a self-mixing interferometric effect, a laser diode functions as a position sensor with nano-meter precision. We model and characterize the self-mixing interferometric signal and design a proportional integral controller accordingly. The residual position error is as small as  $\pm 1.5$  nm and  $\pm 9$  nm under an actuated surface with displacement of  $4.8 \mu\text{m}$  and a spinning disk with displacement of  $16 \mu\text{m}$ , respectively.

In addition to high transmission through the straw-shaped writing probe and high precision of the gap sensing probe, the dual-probe system has advantages of compactness, lightness, simplicity, and integration capability. The results that this thesis achieves open a new avenue to near-field transmission and servo control and provide a practical solution for data storage applications.

## Acknowledgement

It's a long journey to finish the PhD. If there were no numerous help and strong support from countless people along the way, I could not have made it.

First of all, I would like to express my sincere gratitude to my advisor, Prof. Han-Ping D. Shieh, for his full support in my academic life. He not only shows me a model of active attitude to work but also influences my perspective on the world. I would like to thank my co-advisor, also my senior classmate, Prof. Chung-Ho Tien. He has given me countless help in my research since I joined Prof. Shieh's group. I am also grateful to my committee, Prof. Ken Y. Hsu, Prof. Chuang-Chuang Tsai, Dr. Min-Shyong Lin, Prof. Jin-Chern Chiou, Prof. Cheng-Chung Lee, and Prof. Yung S. Liu for their constructive advice on my thesis.

In May 2005, I got a chance to work as a visiting research scholar at Carnegie Mellon University for fifteen months. Thank my advisors at CMU, Prof. T. E. Schlesinger and Prof. James Bain, who guided me in the research project of a near-field servo control system. That is an essential part of my thesis. Dr. Philipp Herget whom I worked with helped me a lot in the experimental direction and setup. Also thank Chris Bowman for his help in training me to make apertures using focused ion beam milling and device fabrication in the clean room.

I am very grateful to my team members, Wan-Ting Lin, Chi-Chin Lee, and Yu-Chieh Chen. They contributed a lot to the simulation and fabrication of nano-apertures. Our collaboration and achievements showed the power of good team work. Thank Hong-Long Hsu for making a lot samples at Precision Instrument Development Center (PIDC) for my experiment. I would also like to thank Dr. Pei-Kuen Wei and Hsieh-Li Chou of Research Center for Applied Science, Academia Sinica, for their technical support, discussion and help in the

near-field intensity measurement.

Except for research life, Prof. Shieh's lab is more like a big family. Working in this group was one of the most wonderful experiences that I have ever had. Thank Yi-Pai Huang, Ko-Wei Chien, An-Chi Wei, Chi-Hung Lee, Kevin Ni, Chun-Ho Chen, Bo-Ru Yang, and Moca Chen. Their friendship made my life here colorful. I also appreciated assistants' patience and aid no matter what kind of help I needed. They are Vivian Ni, Ms. Huang, Ms. Chang, and Ms. Chu.

Fifteen-month stay in Pittsburgh was a beautiful memory because I met so many good friends there. I enjoyed every seconds being with my cute roommates, Bamboo, Steve, Kursat and Tingfang. I never forget every happy moment that we spent together. I was also so grateful to them for everything they did for me, especially their accompanying me when I was upset. I would like to express my thanks to Yung-Hui and Hwaning. I appreciated their care about me and sincere friendship. I also want to thank my office mate, Jingwei Liu. No matter how late I worked in office, he was always the only one to stay with me.

Many friends of mine gave me a lot of support on my road to the PhD. Jennifer motivated me to look forwards to a higher degree and also gave me courage when I suffered frustration. Hsianghwa never hesitated to accompany me or lost her patience to help me no matter what and when my request was even though she was thousands miles away from me. I appreciated Ricca's help to push me to progress in my research before I went to the US. I also want to thank Sophia for her time and encouragement in the last year.

Finally, I present my deepest gratitude to my family. My parents not only gave me my life but also provided me a good environment that I can concentrate on my job. My brothers and sister always paid their full attention and love to their youngest brother. They always tried their best to support me in any ways



they can do for me. My cute nephews and nieces also gave me the power to keep moving on. In addition, I will like to express my special acknowledgement to my second elder brother and sister-in-law for their unconditionally taking care about me during the past five years when I lived in their place.



# Table of Content

<b>Abstract</b> .....	i
<b>Acknowledgement</b> .....	v
<b>Table of Content</b> .....	viii
<b>List of Publications</b> .....	x
<b>List of Tables</b> .....	xii
<b>List of Figures</b> .....	xii
<b>Chapter 1 Introduction</b> .....	<b>- 1 -</b>
1.1 Introduction to Data Storage System .....	- 1 -
1.2 Near-field Optical System .....	- 4 -
1.2.1 Subwavelength Aperture.....	- 4 -
1.2.2 Solid Immersion Lens .....	- 8 -
1.3 Dual-probe Fiber Head.....	- 10 -
1.4 Objective .....	- 12 -
1.5 Organization .....	- 12 -
<b>Chapter 2 Theories of Near-field Transmission</b> .....	<b>- 15 -</b>
2.1 Bethe’s Theory .....	- 15 -
2.2 Waveguide Theory .....	- 21 -
2.3 Surface Plasmon Polaritons.....	- 26 -
2.4 Summary .....	- 32 -
<b>Chapter 3 Modeling of Hybrid Effect in Transmission Enhancement</b> .....	<b>- 35 -</b>
3.1 Methodology and Parameters .....	- 35 -
3.1.1 Optical Model and Premises.....	- 36 -
3.1.2 Parameters .....	- 39 -
3.2 Nano-waveguide Design.....	- 41 -
3.2.1 Rectangular Aperture .....	- 41 -
3.2.2 Optimization of Ridge Part .....	- 42 -
3.2.3 Optimization of Aperture Part .....	- 44 -
3.3 Nano-waveguide with Corrugation .....	- 46 -
3.3.1 Corrugation in Entrance Interface .....	- 46 -
3.3.2 Corrugation in Exit Interface .....	- 48 -
3.4 Nano-waveguide with Oblique Illumination.....	- 51 -
3.4.1 Effect of SPP Mode by Oblique Illumination .....	- 51 -

3.4.2 Effect of Propagation Mode of Aperture .....	- 55 -
3.5 Summary .....	- 58 -
<b>Chapter 4 Experiment in Enhanced Transmission of Hybrid Effect.....</b>	<b>- 59 -</b>
4.1 Fabrication of Subwavelength Aperture.....	- 59 -
4.1.1 Preparation of Metal Film.....	- 59 -
4.1.2 Focused Ion Beam Milling.....	- 61 -
4.2 Measurement Instrument .....	- 64 -
4.2.1 Near-field Scanning Optical Microscope.....	- 64 -
4.2.2 Far-field Transmission Measurement System.....	- 68 -
4.3 Experimental Results.....	- 69 -
4.3.1 Preparation of Aperture.....	- 70 -
4.3.2 Far-field Power Throughput .....	- 71 -
4.3.3 Near-field Intensity Distribution .....	- 73 -
4.4 Summary .....	- 76 -
<b>Chapter 5 Near-field Servo Control System Employing Self-mixing Sensor-</b>	<b>77 -</b>
5.1 System Configuration.....	- 78 -
5.2 Characterization of Self-mixing Signal .....	- 78 -
5.2.1 Modeling of Self-mixing Signal .....	- 79 -
5.2.2 Experiment of Characterizing Self-mixing Signal.....	- 82 -
5.3 Fabrication of Laser Diode Sensor.....	- 84 -
5.4 Approach Limit .....	- 85 -
5.5 Controller Design.....	- 86 -
5.5.1 Dynamic Response of Actuator .....	- 86 -
5.5.2 Controller Design.....	- 87 -
5.6 Operation Test .....	- 89 -
5.6.1 Actuated Surface Test.....	- 89 -
5.6.2 Spinning Disk Test.....	- 90 -
5.7 Summary .....	- 91 -
<b>Chapter 6 Conclusions and Future Works .....</b>	<b>- 93 -</b>
6.1 Conclusions.....	- 93 -
6.2 Future Works .....	- 95 -
<b>Reference .....</b>	<b>- 97 -</b>

## List of Publications

### Journal Papers

- [1 ] **Jen-Yu Fang**, Chung-Hao Tien, Han-Ping D. Shieh, Philipp Herget, James A. Bain, and T. E. Schlesinger, "Optical feedback height control system using laser diode sensor for near-field data storage applications," IEEE/OSA Journal of Lightwave Technology, Vol. 25, No. 12, pp. 3704-3709 (2007).
- [2 ] **Jen-Yu Fang**, Chung-Hao Tien, and Han-Ping D. Shieh, "Dual-probe near-field fiber head with gap servo control for data storage applications," Optics Express, Vol. 15, No. 22, pp. 14619-14628 (2007).
- [3 ] **Jen-Yu Fang**, Chung-Hao Tien, and Han-Ping D. Shieh, "Hybrid-effect transmission enhancement induced by oblique illumination in nano-ridge waveguide," Optics Express, Vol. 15, No. 18, pp. 11741-11749 (2007).
- [4 ] **Jen-Yu Fang**, Philipp Herget, James a. Bain, and T. E. Schlesinger, "Laser diode active height control system for data storage application," Proceeding of SPIE, v6282, p62820p (2006).
- [5 ] Yu-Chieh Chen, **Jen-Yu Fang**, Chung-Hao Tien, and Han-Ping D. Shieh, "High-transmission hybrid-effect-assisted nanoaperture," Optics Letter, Vol. 31, No. 5, pp. 655-657 (2006).
- [6 ] Yu-Chieh Chen, **Jen-Yu Fang**, Chung-Hao Tien, and Han-Ping D. Shieh, "Double-corrugated C-shaped aperture for near-field recording," Japanese Journal of Applied Physics, Vol. 45, No. 2B, pp. 1348-1350 (2006).

### International Conference Papers

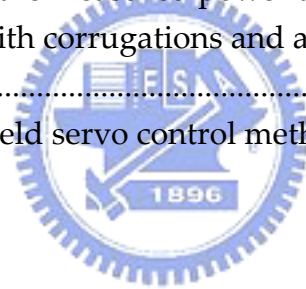
- [1 ] **Jen-Yu Fang**, Philipp Herget, James a. Bain, and T. E. Schlesinger, "Laser Diode Active Height Control System for Near-field Recording," APDSC 2006, Taipei, Taiwan (2006).
- [2 ] **Jen-Yu Fang**, Chung-Hao Tien, and Han-Ping D. Shieh, "Fiber-based Light Delivery System for Near-field Recording," APDSC 2006, Taipei, Taiwan (2006).
- [3 ] **Jen-Yu Fang**, Philipp Herget, James a. Bain, and T. E. Schlesinger, "Laser Diode Active Height Control System for Data Storage Application," ODS 2006, Montreal, Canada (2006).

- [4 ] **Jen-Yu Fang**, Yu-Chieh Chen, Chung-Hao Tien, and Han-Ping D. Shieh, “Microprobe with Wedge-shaped Graded-index Fiber Lens for Near-field Recording Applications,” ISOM/ODS 2005, Honolulu, USA (2005).
- [5 ] Yu-Chieh Chen, **Jen-Yu Fang**, Chung-Hao Tien, and Han-Ping D. Shieh, “Ultrahigh Optical Transmission through a C-aperture with Surface Corrugation,” ISOM/ODS 2005, Honolulu, USA (2005).
- [6 ] **Jen-Yu Fang**, Wan-Ting Lin, Chung-Hao Tien, Yi Chiu, and Han-Ping D. Shieh, “C-shaped aperture for near-field recording,” ISOM 2004, Jeju, Korea (2004).
- [7 ] Chung-Hao Tien, Yin-Ting Sun, **Jen-Yu Fang**, Meng-Yu Wu, Wensyang Hsu, Yi Chiu, and Han-Ping D. Shieh, “Integrated Planar Pickup with SIL/ Aperture for Near-Field Recording,” ISOM 2003, Nara, Japan (2003).



## List of Tables

Table 3-1 Spot sizes at 50 nm away from square apertures.....	- 42 -
Table 3-2 Comparison of SPP wavelength by using SPP theory and FDTD method .....	- 54 -
Table 3-3 The calculated power throughput and enhancement of a single C-shaped aperture, a C-shaped aperture with corrugations, and a C-shaped aperture with oblique illumination .....	- 58 -
Table 4-1 Far-field transmission of a circular aperture, a C-aperture, and a C-aperture with a corrugation and calculated power throughput enhancement induced by the hybrid effect .....	- 72 -
Table 4-2 Far-field transmission of a circular aperture, a C-aperture with two different illuminating angles and calculated power throughput enhancement induced by the hybrid effect .....	- 72 -
Table 4-3 Comparison between the measured power throughput enhancement of a C-shaped aperture with corrugations and a C-shaped aperture with 44-degree illumination.....	- 76 -
Table 5-1 Comparison of near-field servo control methods .....	- 92 -



## List of Figures

Fig. 1-1 Road map of optical storage systems.....	- 2 -
Fig. 1-2 Schematic illustration of a subwavelength aperture.....	- 5 -
Fig. 1-3 (a) A bow-tie antenna and (b) dipole antennas.....	- 6 -
Fig. 1-4 Configuration of a conventional NSOM fiber probe and a sample surface .....	- 8 -
Fig. 1-5 Schematic illustration of a solid immersion lens.....	- 8 -
Fig. 1-6 The reflected power as a function of the air gap .....	- 9 -
Fig. 1-7 Schematic illustration of the configuration of a dual-probe fiber head system .....	- 11 -
Fig. 2-1 Model of Bethe's theory.....	- 16 -
Fig. 2-2 Diagram of source point and field point .....	- 18 -
Fig. 2-3 A typical planar waveguide consisting of three layers arranged that guiding index of refraction ( $n_f$ ) is larger than the substrate ( $n_s$ ) and cover ( $n_c$ ) indices.....	- 21 -
Fig. 2-4 Geometric relationship between longitudinal and transverse components $\beta$ , $\kappa$ of the wavevector $k$ .....	- 22 -
Fig. 2-5 (a) A buried waveguide and its equivalent structure: (b) a thin and (c) a thick waveguide .....	- 24 -
Fig. 2-6 $ E ^2$ distribution at 48 nm from (a) C-shaped, (b) square, and (c) modified C-shaped apertures and $ E ^2$ cross section along (d) X and (e) Y axis.....	- 25 -
Fig. 2-7 Schematic illustration of surface plasmons propagating along the dielectric-metal interface induced by a p-polarized incident light ....	- 27 -
Fig. 2-8 Dispersion curve of surface plasmons and incident light.....	- 28 -
Fig. 2-9 Excite surface plasmon polaritons by (a) a grating structure and (b) attenuated total reflection.....	- 29 -
Fig. 2-10 Transmission spectrum of (a) a circular aperture surrounded with a corrugation structure and (b) a hole array .....	- 30 -
Fig. 2-11 Configuration of a hole array in a metal film sandwiched with two dielectric materials.....	- 31 -
Fig. 3-1 Dimensional parameters of (a) a C-shaped aperture and (b) a groove surrounding a C-shaped aperture and transmission model through (c) a C-shaped aperture, (d) a C-shaped aperture surrounded with a corrugation, and (e) a C-shaped aperture with oblique illumination	- 39 -
Fig. 3-2 The PT as a function of the side length of a square aperture .....	- 42 -
Fig. 3-3 The PT as a function of gap $g$ with various ridge lengths $c$ .....	- 43 -

Fig. 3-4 The PT as a function of aspect ratio  $AR$  with various aperture lengths  $a$  as ridge width  $d$  is 46 nm ..... - 44 -

Fig. 3-5 The PT as a function of aspect ratio  $AR$  with various aperture lengths  $a$  as ridge width  $d$  is 34 nm ..... - 45 -

Fig. 3-6 The PT as a function of the interval  $i$  with various widths  $w$ ..... - 47 -

Fig. 3-7 The PT as a function of pitch  $p$  with various interval  $i$  ..... - 48 -

Fig. 3-8 The PT as a function of the interval  $i$  on the exit plane with various widths  $w$ ..... - 50 -

Fig. 3-9 The power throughput (PT) at a distance of 50 nm from the aperture and reflection coefficient  $r_p$  as a function of the incident angle ..... - 52 -

Fig. 3-10 (a)  $E_z$ , (b)  $E_x$ , and (c)  $H_y$  field profile, and (d) magnitude of Poynting vector plot when the incident angle is 44 degree. The dashed line showed the contour of the metal film and the C-aperture..... - 54 -

Fig. 3-11 The spectral response of the power throughput through the C-shaped aperture with a incident angle of 44 degree ..... - 55 -

Fig. 3-12 Electric intensity distribution inside the waveguide at a position of (a) 1/4, (b) 1/2, (c) 3/4 of the length from the entrance plane when propagating along the waveguide, and (d) the power throughput decay as a function of the distance from the waveguide..... - 56 -

Fig. 3-13 Power throughput as the waveguide scales up or down by the scale factor in the model of 44-degree illumination..... - 57 -

Fig. 4-1 Fabrication process of a free-standing metal film (a) deposit silicon nitride on silicon wafer, (b) pattern on photo resist, (c) remove silicon nitride by RIE, (d) wet etch using KOH, (e) deposit silver film, and (f) remove silicon nitride by ICP-RIE ..... - 60 -

Fig. 4-2 Parameters determining the quality of a special-shaped aperture ..... - 62 -

Fig. 4-3 Operation modes of an apertured NSOM (a) illumination, (b) collection, (c) illumination collection, (d) reflection, and (e) reflection collection ..... - 65 -

Fig. 4-4 Configuration of far-field measurement system..... - 68 -

Fig. 4-5 SEM photos of (a) a circular aperture, (b) a C-shaped aperture, and (c) a C-shaped aperture surrounded by a groove ..... - 70 -

Fig. 4-6 SEM photo of a single C-shaped aperture for oblique illumination.... - 70 -

Fig. 4-7 Intensity distributions measured by NSOM (a) background noise and (b) the C-shaped aperture ..... - 74 -

Fig. 4-8 Near-field distribution observed by NSOM with (a) normal and (b) 44-degree incidence..... - 74 -

Fig. 4-9 Calculated electric intensity distribution at 50nm from the



nano-waveguide with the experimental dimensions at (a) normal incidence and (b) 44-degree incidence.....	- 75 -
Fig. 4-10 Calculated (a) $E_x$ and (b) $E_z$ field profile with the experimental dimensions .....	- 75 -
Fig. 5-1 Schematic illustration of system configuration .....	- 78 -
Fig. 5-2(a) Configuration of an external-cavity laser diode with a length of fiber and (b) an equivalent laser diode .....	- 80 -
Fig. 5-3 Simulated self-mixing interferometric fringe .....	- 81 -
Fig. 5-4 (a) Experimental setup for feedback signal characterization and (b) measured signal from the photodiode.....	- 82 -
Fig. 5-5 Comparison of a measured feedback signal and a calculated self-mixing interferometric signal .....	- 83 -
Fig. 5-6 (a) photo of the pickup with laser diode mounted and (b) side view of modified laser package .....	- 84 -
Fig. 5-7 (a) Angular variation of the disk and the laser size determines the approach limit and (b) the measured angular variation of the glass disk at different radial position along tangential and radial direction .....	- 85 -
Fig. 5-8 (a) Measured open-loop frequency response of the actuator and (b) calculated step response of the actuator according to the modeling transfer function.....	- 86 -
Fig. 5-9 Block diagram of the gap sensing probe system.....	- 87 -
Fig. 5-10 Open-loop frequency response of the active height control system .	- 88 -
Fig. 5-11 (a) Configuration of actuated surface test system and (b) experimental results when the displacement of the actuated surface is $4.8 \mu\text{m}$ at 1500 rpm.....	- 90 -
Fig. 5-12 (a) Configuration of spinning disk test system and (b) experimental results with a disk runout of $16 \mu\text{m}$ at 1500 rpm .....	- 91 -



# Chapter 1 Introduction

## 1.1 Introduction to Data Storage System

Based on the recording mechanism, data storage can be classified into three groups: electric, magnetic, and optical storage systems. In electric storage systems, information is stored in the form of electric charges, either in transistors or capacitors. Magnetic storage systems store information in the magnetic state of atoms of recording medium, which is written by an external magnetic field and read out by a magnetic transducer. Instead, optical storage systems store information by the modulation in the reflectivity of disk surfaces, for example, by either physical structures or crystalline states [1].

In contrast to electric storage, magnetic and optical storage systems have features in common. Both of them require a pickup head to fly over disk surfaces for recording or picking up data on the disk so that a flying head and a servo control system are essential components in these two types of systems. Furthermore, the capacity of these two systems is comparatively higher than that of electric storage systems. However, data access rate of magnetic and optical storage systems is relatively low compared to that of electric ones. Therefore, both magnetic and optical storage systems are categorized in the secondary memory for storing and backing up data while electric storage systems are used as the primary memory for processing information. Because of divergences in the nature between the primary and the secondary memory, our study will focus only on the secondary memory.

Due to the explosively increasing demand for storing information as multimedia is spread out over the world and widely used in daily life, data storage systems with higher recording capacity are undoubtedly desired.

Moreover, mobility, miniaturization and power consumption are also considerable issues in data storage systems. Therefore, those requirements drive the development of storage systems toward higher recording density and efficiency. A road map of optical storage systems shown in Fig. 1-1 illustrates an example of the development of the storage capacity. From the first CD launched in the 80s to the latest near-field disc, the capacity increases hundreds times or even higher. However, the increase of the recording density is not unlimited. The principles of recording mechanisms and the physical characteristics of recording materials determine the theoretic ceiling of the recording density.

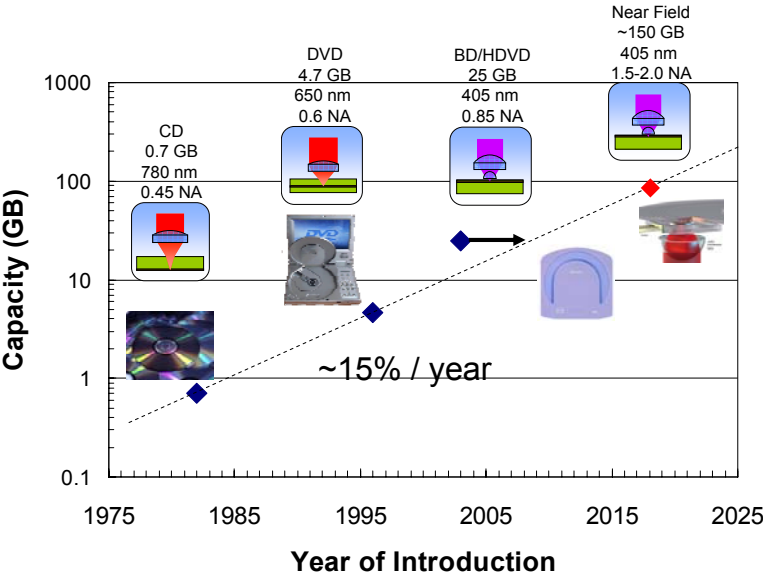


Fig. 1-1 Road map of optical storage systems

In magnetic storage systems, the recording density depends on mark sizes, i.e. a minimum magnetic domain. With the decrease of mark sizes, grain sizes in the recording medium must be smaller than the mark sizes to obtain a sufficient signal-to-noise ratio. However, if grain sizes are too small, random thermal fluctuations cause magnetic domain switching and consequent destruction of data in a conventional recording medium. The size at which the magnetic state of a grain is no longer thermally stable is the so-called super-paramagnetic limit. The criterion for thermal stability is shown in Eq. (1-1) as below [2],

$$\frac{K_u V}{k_B T} > 70, \quad (1-1)$$

where  $K_u$  is the uniaxial anisotropy coefficient,  $V$  is the grain volume,  $k_B$  is Boltzmann's constant, and  $T$  is temperature. Although some recording materials have a sufficiently large  $K_u$  for thermal stability, the coercivity of these materials at room temperature is too large to be switched by an external magnetic field generated by conventional heads. One solution to overcome this issue is to introduce a heat-assistance method by employing a laser beam to heat a local area of the recording material. When the temperature of the medium is close to its Curie point, the coercivity drops dramatically so that only a small magnetic field is needed to record data in the medium. Therefore, an optical system that can confine sufficient optical power into a spot with a diameter of less than 50 nm is necessary for heat-assisted magnetic recording (HAMR) [3].

In optical storage systems, a laser stylus, a spot focused by an objective lens, is used to illuminate disk surfaces. The reflected light from the disk surface is collected by the objective lens and delivered to an optical detector. The storage density is dependent on the spatial resolution of the laser stylus, which corresponds to the spot size of the optical system. According to the diffraction theory, the theoretic minimum spot size of a far-field focusing system, also called the diffraction limit, is proportional to the ratio of the incident wavelength to the numerical aperture (NA) of the optical system,

$$d \propto \frac{\lambda}{NA}, \quad (1-2)$$

where  $d$  is the diameter of the focused spot,  $\lambda$  is the incident wavelength, and  $NA$  is the numerical aperture. Thus, the only way to increase the storage density is to reduce the wavelength or increase the numerical aperture. However, aberrations, which are inversely proportion to the square or cubic of the spot size, become significantly worse with the decrease of the wavelength or the increase of  $NA$ .

Therefore, in order to break through the theoretic limit, both magnetic and optical storage systems need an optical system that can bring a subwavelength spot to the recording medium. According to near-field theories, in a distance of less than a wavelength from optical devices, evanescent waves are taken into account and thus the field behavior is distinctively different from that after propagating far away from the devices. Because the evanescent waves have higher spatial frequency information than that of the propagating waves, a subwavelength spatial resolution beyond the diffraction limit can be obtained in the near field. Since the evanescent waves decay exponentially with the distance from the optical device, the spacing between the device and the medium surface has to be kept within a wavelength, typically less than 100 nm. Therefore, remaining the spacing with nanoscale precision is a challenging issue for near-field optical systems.

## 1.2 Near-field Optical System



A near-field optical system uses near-field optical techniques to achieve subwavelength resolution. However, challenging issues accompany the shrinkage of spot sizes and gaps between optical devices and media. Based on mechanisms employed, near-field optical systems are categorized in two groups, subwavelength apertures and solid immersion lenses, and explained in the following.

### 1.2.1 Subwavelength Aperture

#### 1. Principle

A subwavelength aperture in a metal film blocks part of incident fields to confine optical energy into a tiny area, as shown in Fig. 1-2. Subwavelength resolution of  $\lambda/20$  was first demonstrated by employing a nano-aperture in

near-field microscopy [3]. This novel breakthrough gave the birth to near-field scanning optical microscopes (NSOM) and opened a new avenue of near-field optics [4-8]. In conventional NSOMs, a tapered fiber probe was used to generate a tiny stylus for resolving the image. By depositing a metal film on the side wall of the stylus, a nano-aperture with a symmetric shape was consequently formed at the tip.

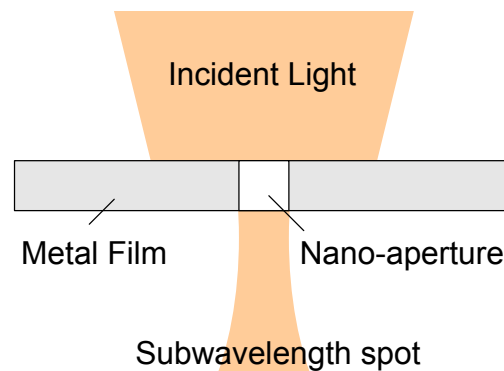


Fig. 1-2 Schematic illustration of a subwavelength aperture

Subwavelength apertures have advantages of simple configuration and easy fabrication. However, because the field inside the fiber suffered a serious energy loss in the tapered area and through the aperture, the transmission of a tapered fiber probe typically ranged from  $10^{-3}$  to  $10^{-5}$  [9-11]. Thus the picked-up signal was relatively noisy and complex signal processing was necessarily required in the system. Therefore, a lot of effort was made to increase the transmission of subwavelength apertures.

#### (1) Special-shaped Apertures

Special-shaped apertures were designed to enhance the transmission by exciting either radiation from the aperture which functions as an antenna or propagation modes inside the aperture. A bow-tie antenna or dipole antenna was proposed to generate radiation from resonance of electric fields on the

antenna induced by incident waves, as shown in Figs. 1-3 (a) and (b) [12-14]. The resonance coupled from incident light, highly dependent on the geometry and dimensions of the antenna, radiated electromagnetic waves and thus generated a spot of a diameter much less than a wavelength. An alternative approach was to employ an aperture as a waveguide. Either a C- or I-shaped aperture functioning as a ridge waveguide supported propagation modes and thus reduced the energy dissipation through the aperture [15-19]. According to waveguide theories, the propagation modes of a waveguide are particular patterns of field which fulfill the boundary condition and can propagate through the waveguide without significant energy loss. The refractive indices and the geometry of the waveguide determine the propagation modes that can be supported inside the waveguide. Therefore, the dimensions of the aperture dominate the transmission and the spot size through the aperture.

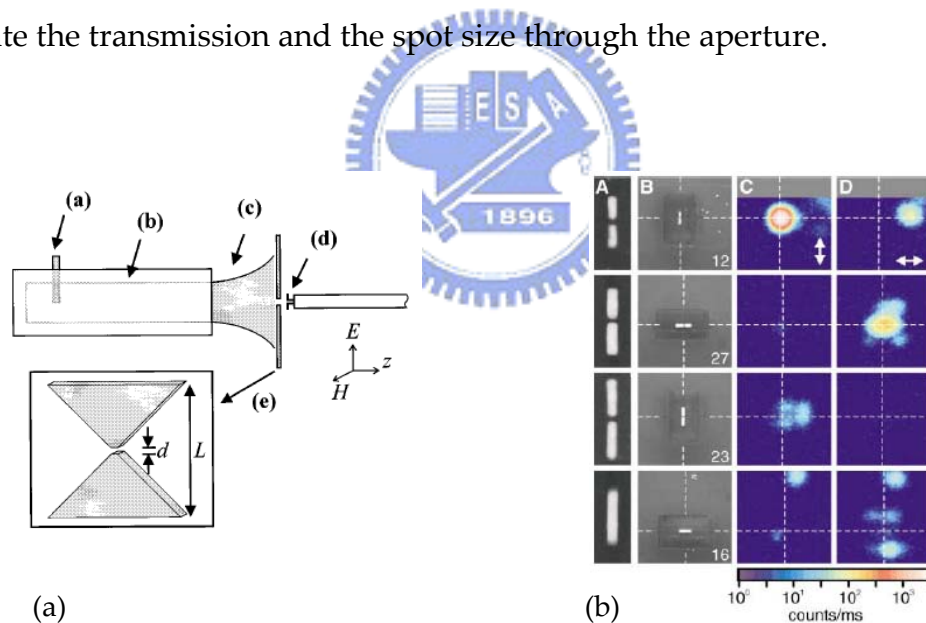


Fig. 1-3 (a) A bow-tie antenna and (b) dipole antennas

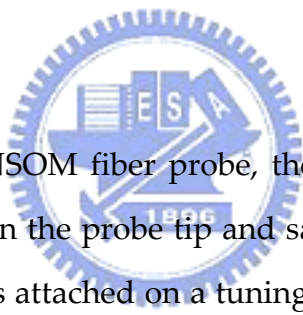
## (2) Surface Plasmon Polaritons

Another solution is to induce the surface plasmon excitation in dielectric-metal interfaces of a metal film [20-23]. The resonance of surface plasmon polaritons induced by the incident light will result in oscillation of



electrical fields and re-radiation in the vicinity of the film surface. The metal structure itself then functions like an active light source. It means that the resonance of surface plasmons modes on both sides of a metallic film makes the energy transfer between incident light and surface plasmons as well as between surface plasmons and emitted light possible. Consequently, under a proper design, the energy carried by photons obstructed behind the film contributes to the transmission through the film and thus breaks through the theoretic limit. Unfortunately, because the dispersion curve of surface plasmons lies right of the light line of the same energy, surface plasmons have a longer wave vector than that of light. An additional wave vector has to be added to excite surface plasmons by introducing periodic structures, such as hole arrays and corrugations, or attenuated total reflection.

## 2. Gap Control



For a conventional NSOM fiber probe, the shear force method is used to detect the spacing between the probe tip and sample surfaces, as shown in Fig. 1-4 [24]. The fiber probe is attached on a tuning fork which is driven by a piezo actuator. In the absence of the sample surface, the fiber probe with the tuning fork is driven to resonate at its nature resonant frequency. As the fiber probe is approaching to the surface, the shear force between the fiber tip and the sample surface alters the resonant amplitude and then can be detected by the piezo actuator which can alternatively function as a sensor.

Because the change in the resonant amplitude is a function of the gap and then can be used as a feedback servo signal, the shear force method has an advantage of extremely high sensitivity. Typically, a residual position error of less than 0.1 nm can be achieved. However, since the amplitude of the feedback signal is too low to be detected, the signal-to-noise ratio (SNR) is so low that a complicated signal processing system is required to filter out the signal.

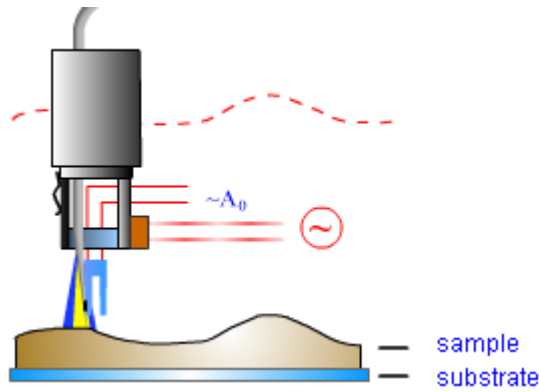


Fig. 1-4 Configuration of a conventional NSOM fiber probe and a sample surface

## 1.2.2 Solid Immersion Lens

### 1. Principle

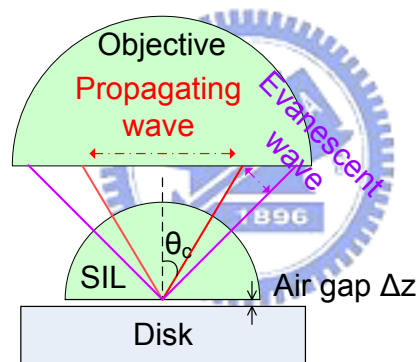


Fig. 1-5 Schematic illustration of a solid immersion lens

Since the diffraction limit is determined by the ratio of the incident wavelength to the numerical aperture, the spot size of far-field optical systems can be further reduced by increasing the effective NA if the incident light experiences a refractive index of greater than air. As a result, a semi-spherical solid immersion lens (SIL) was proposed to insert into the optical path of a focusing beam, as shown in Fig. 1-5 [25-27]. The incident light which arrived at the bottom of the solid immersion lens at an angle of greater than the critical angle suffered a total internal reflection at the dielectric-air interface where evanescent waves were generated and penetrated through. Spatial resolution

can be improved by a factor of refractive index of the material of SIL because evanescent waves carried information with higher spatial frequencies. However, the amplitude of evanescent waves dropped exponentially with an increase of the distance from SIL. An extremely precise gap control system was necessary for remaining the spacing between the SIL and the medium less than a wavelength, typically less than 100 nm in the case of blue lasers [28-29]. Moreover, a semi-spherical SIL was difficult to fabricate and also too bulky to be integrated into flying heads.

## 2. Gap Control

In a solid immersion lens system, when a surface is in close proximity to the bottom of the solid immersion lens, the coupling between the evanescent wave and the surface will generate an orthogonal polarization component to the reflected field. And the polarization component decays as the increase of the spacing between the surface and the bottom of the SIL. Therefore, a polarized beam splitter is used to filter out the orthogonal component and then the filtered reflected power is a function of the spacing, as shown in Fig. 1-6 [30]. The linear region of this signal can be used as a feedback signal to remain the spacing with nanoscale precision.

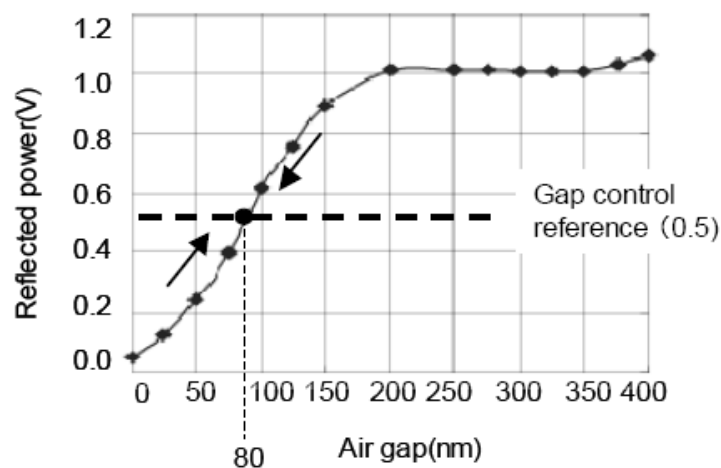


Fig. 1-6 The reflected power as a function of the air gap

Similar to the shear force method, the reflected power method also has an advantage of high sensitivity. A residual position error of less than 5 nm was successfully demonstrated. However, a complex optical system is necessary for delivering and filtering optical signals. Due to numerous lenses, the alignment among those lenses becomes a challenging issue.

### **1.3 Dual-probe fiber head**

Upon the demand of recording density, either magnetic or optical storage systems require a near-field light source with active gap control that can confine optical power into a subwavelength spot with sufficient transmission. A conventional fiber probe has advantages of compactness, ease of fabrication, and integration capability; however, low transmission results in high power consumption and heat dispersal issues. The gap control employing shear force between the fiber tip and the sample surface as the feedback signal encounters an issue of low speed and low SNR. In contrast, solid immersion lens efficiently brings optical power to the medium but a complex and costly process is necessary for fabricating the SIL. In addition, the SIL is too bulky to be installed on a flying head and significantly degrades the dynamic characteristics of the optical head. The reflected power method used for focusing servo control requires a complicated external optical system to filter out and process the signal.

Due to the issues that conventional systems encounter, by taking advantage of fiber for compactness, lightness, simplicity, and integration capability, we propose a novel dual-probe near-field fiber head system. The system consists of a straw-shaped writing probe that delivers optical power to the medium and a gap sensing probe that detects the spacing and sends a feedback signal to the controller. The writing probe with a straw shape yields a high transmission

resulting from the hybrid effect we discover and the gap sensing probe exhibits nano-scale precision as a result of the self-mixing effect.

The system configuration is schematically illustrated in Fig. 1-7. In the writing probe, a 1X2 10/90 fiber coupler is inserted into the optical path to split the light into two. 90% of the light goes to the straw-shaped probe, where the end face is coated with a metallic film and perforated by a C-shaped aperture at the center, while the remaining 10% light goes to the bare flat reference probe where the emitted power is measured to monitor the output from the straw-shaped probe. In the gap sensing probe, the spacing between the probe end and the target surface functions as an external cavity for the laser diode. The interference between the reflected light and the field inside the laser cavity modulates the output power as a function of the spacing. The output power is detected by the photodiode and sent to the controller as a feedback signal. The dual-probe fiber head is installed on a conventional biaxial actuator driven by the controller to maintain the spacing with nanometer position precision.

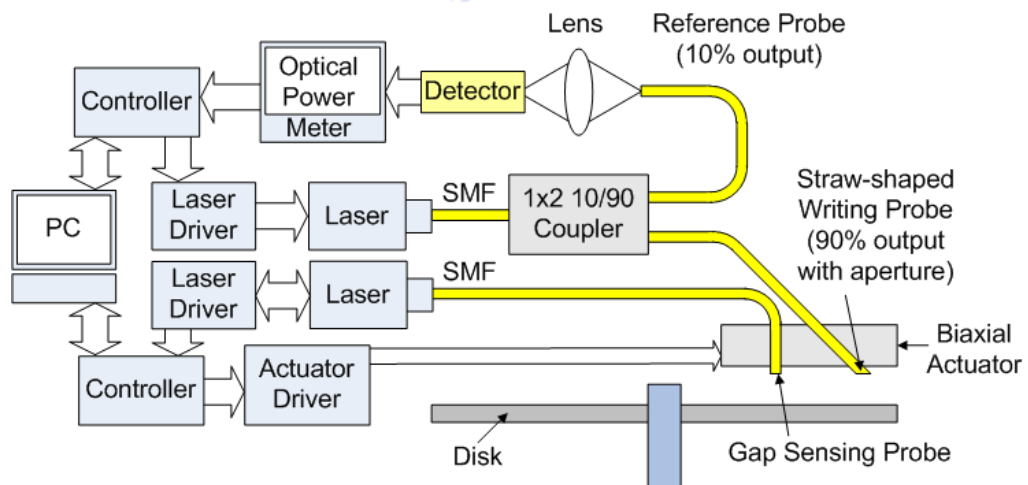


Fig. 1-7 Schematic illustration of the configuration of a dual-probe fiber head system

## 1.4 Objective

The objective of this thesis is to present an efficient, miniaturized, compact, highly integrated dual-probe fiber-based optical head with simple and precise gap servo control. The dual-port fiber head consists of a straw-shaped writing probe with a subwavelength C-shaped aperture and a gap sensing probe employing a self-mixing laser sensor. To resolve the issue of low transmission through a subwavelength aperture in conventional fiber probes, we propose a novel configuration, a C-shaped aperture surrounded by corrugations or illuminated with obliquely incident light, to excite a hybrid effect. Propagation modes and surface plasmon waves exist simultaneously and contribute to the further enhancement of transmission through the waveguide. A high-transmission writing probe is then designed and realized by employing the hybrid effect. On the other hand, to overcome the issue of a complicated optical system that conventional detecting methods need, we design a gap sensing probe employing self-mixing interferometric effect. We characterize the modulation of output power as a function of the spacing between the probe and the disk surface and use it as a feedback signal. According to the feedback signal, we also design a controller and circuits for driving a conventional biaxial actuator to remain the spacing with nanometer position precision.

## 1.5 Organization

In Chapter 2, we review theories of near-field transmission, including Bethe's theory, waveguides, and surface plasmons. Based on those theories, in Chapter 3, we propose a novel optical design, a C-shaped aperture in a metal film as a waveguide surrounded with a circular corrugation or illuminated with obliquely incident light. This design induces a hybrid effect consisting of propagation modes inside the waveguide and surface plasmon modes in the

dielectric-metal interfaces to enhance the transmission through the aperture. Modeling and optimization of this design are presented. The simulation results, including mechanisms of the hybrid effect and the transmission enhancement, are also explained and discussed. In Chapter 4, the fabrication of hybrid-effect apertures and measurement instruments are presented and followed by the experimental results that demonstrated the proposed hybrid effect.

Chapter 5 focuses on the development of a near-field servo control system employing a self-mixing interferometric laser sensor. We characterize the interferometric signal in a laser diode and realize a laser sensor by modifying a commercial laser diode. The frequency response of a biaxial actuator with a laser sensor installed is measured and a controller is designed for the laser sensor system accordingly. Under an actuated surface test system and a spinning disk system, we demonstrate the operation of a near-field control system using a laser sensor on a biaxial actuator.

The summary of the findings and throughputs of this thesis is presented in Chapter 6. We also suggest prospective works for near-field light delivery systems.





# Chapter 2 Theories of Near-field Transmission

In this chapter, we briefly review the relevant literature on near-field transmission through subwavelength apertures. Based on the assumption of a perfect conducting film, Bethe revealed that the transmission through a subwavelength aperture is proportional to the fourth power of the aperture size. Although some premises of Bethe's theory do not work out well in the real world, it still discloses a theoretic fundament of the transmission through a subwavelength aperture. A lot of effort thus has been made to break through the theoretic limit. Special-shaped apertures that can function as waveguides are one of promising solutions. If an incident field couples into propagation modes supported by a waveguide, the field can propagate through the waveguide with less energy dissipation. On the other hand, the oscillation of surface plasmon waves on both sides of a metallic film results in the enhancement of the transmission if the satisfaction of the momentum matching condition induces coupling between incident photons and surface plasmon polaritons. Propagation modes of a waveguide and surface plasmon polaritons stimulate the development of a hybrid effect, which is the fundamental theory of a novel light source system we propose.

## 2.1 Bethe's Theory

Consider a normal incident light impinging on a perfect conducting film at plane  $z=0$ , which divides the space into two parts: the left space of  $z<0$  and the right one of  $z>0$ , as shown in Fig. 2-1 [31]. Assume  $E_0$  and  $H_0$  to be the field on the left-hand side of the film if there is no aperture. The field fulfills the boundary conditions for  $z=0$ ,

$$\vec{n} \times \vec{E}_0 = \vec{0} \quad (2-1a)$$

$$\vec{n} \cdot \vec{H}_0 = 0 \quad (2-1b)$$

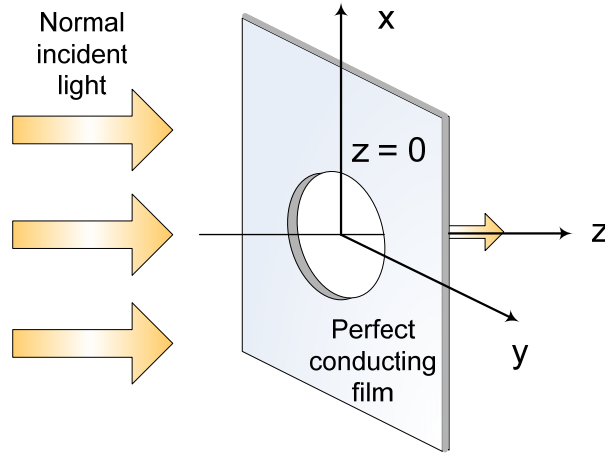


Fig. 2-1 Model of Bethe's theory

The field on the right-hand side vanishes identically and the zero approximation field satisfies the boundary condition everywhere on the film but not in the aperture where  $H$  and the normal component of  $E$  are discontinuous. The field is written as

$$\vec{H} = \vec{H}_0 + \vec{H}_1 \quad \text{for } z < 0 \quad (2-2a)$$

$$\vec{H} = \vec{H}_2 \quad \text{for } z > 0 \quad (2-2b)$$

Then the boundary conditions are:

$$\vec{E}_{1tan} = \vec{E}_{2tan} \quad \text{in the aperture} \quad (2-3a)$$

$$\vec{H}_{2tan} - \vec{H}_{1tan} = \vec{H}_{0tan} \quad \text{in the aperture} \quad (2-3b)$$

$$\vec{E}_{1tan} = \vec{E}_{2tan} = 0 \quad \text{for } z=0 \text{ outside the aperture} \quad (2-3c)$$

If we assume the aperture is symmetric with respect to  $z=0$ ,  $x$ - and  $y$ -components of  $E$  as well as  $z$ -component of  $H$  automatically fulfill the condition of symmetric distribution. Then Eqs. (2-3a) and (2-3b) are rewritten in the

following form:

$$\vec{E}_{2z} = \frac{1}{2} \vec{E}_{0,z} \quad (2-4a)$$

$$\vec{H}_{2\tan} = \frac{1}{2} \vec{H}_{0\tan} \quad (2-4b)$$

Since the aperture size is extremely small compared to the wavelength  $\lambda$ ,  $H_{0x}$ ,  $H_{0y}$ , and  $E_{0z}$  are approximated as constants over the aperture. Moreover, the aperture shape is assumed to be circular with radius  $a$ .

By introducing Stratton's formula,  $E$  is represented by a full-vector theory [33].

$$\vec{E}(r) = \frac{1}{4\pi} \int d\sigma [ik\vec{n} \times \vec{H}(r)\phi - (\vec{n} \times \vec{E}(r)) \times \nabla\phi - \vec{n} \cdot \vec{E}(r)\nabla\phi] \quad (2-5)$$

In the absence of electric charges or electric currents, the first item in the integral equation can be omitted. Consequently, magnetic current density  $K$  and surface charge density  $\eta$  are introduced as the sources of the electric field in the aperture. The continuity equation corresponding to magnetic current density and surface charge density is fulfilled. The time dependence of all quantities is assumed to be harmonic oscillation.

$$e^{i\omega t} \text{ and } \omega = ck \quad (2-6)$$

The electric field  $E$  and magnetic field  $H$  can be expressed in terms of  $K$  and  $\eta$  with the aid of scalar potential  $\Psi$  and vector potential  $F$ :

$$\vec{E} = \nabla \times \vec{F} \quad (2-7a)$$

$$\vec{H} = \frac{1}{c} \frac{\partial \vec{F}}{\partial t} - \nabla \Psi \quad (2-7b)$$

where  $F$  and  $\Psi$  are in exact analogy to the electric case, which is represented by the integral of  $K$  and  $\eta$  over the plane of  $z=0$ ,

$$\vec{F}(r) = - \int K(r') \phi(|r - r'|) dr' \quad (2-8a)$$

$$\Psi(r) = \int \eta(r') \phi(|r - r'|) dr' \quad (2-8b)$$

In Eqs. (2-8a) and (2-8b),  $\phi$  is the retarded radiation between the source vector  $r'$  to the field vector  $r$ , as shown in Fig. 2-2.

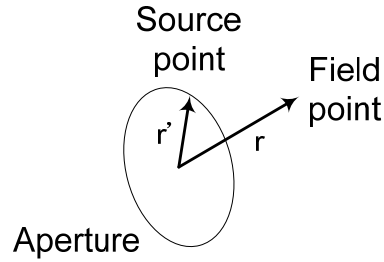


Fig. 2-2 Diagram of source point and field point

By inserting these results into Eqs. (2-7a) and (2-7b),  $E$  and  $H$  can be obtained by the integral of magnetic surface current  $K$  and charge  $\eta$  over the aperture area.

$$\vec{E}(r) = \int \vec{K}(r') \times \nabla \Phi d\sigma \quad (2-9a)$$

$$\vec{H}(r) = \int [i\kappa \vec{K}(r') \Phi - \eta(r') \nabla \Phi] d\sigma \quad (2-9b)$$

Based on the assumption that the aperture size is much smaller than the wavelength,  $H$  is considered as a static field corresponding to the surface charge density  $\eta$ . Thus, the first term in Eq. (2-9b) is neglected. Then we assume a constant magnetic field component  $H_{tan}$  equal to  $\frac{1}{2}H_0$  over the aperture. In addition, the retardation term in Eq. (2-8b) is also omitted because the field point is in proximity to the aperture. Under these assumptions, the scalar potential is written as

$$\Psi(r) = \int \eta(r') \frac{dr'}{|r - r'|} = -\frac{1}{2} \vec{H}_0 \cdot \vec{r} \quad (2-10)$$

This constant field is produced by a uniform distribution of dipoles in an ellipsoid, of which the direction is identical to that of the field. If the axis of the ellipsoid is assumed to be small, the cross section of the ellipsoid in  $XY$  plane

should be equivalent to the aperture area. Thus, the surface density of dipoles  $\mu$  is proportional to the ordinate of the ellipsoid:

$$\mu = (a^2 - r'^2)^{\frac{1}{2}} \quad (2-11)$$

The surface charge density  $\eta$  is then in the form of

$$\eta = -C \frac{\vec{H}_0 \cdot \vec{r}'}{(a^2 - r'^2)^{\frac{1}{2}}} \quad (2-12)$$

where  $C$  is a proportional constant. Then the magnetic surface charge density  $\eta$  and current density  $K$  are

$$\eta = -\frac{\vec{H}_0 \cdot \vec{r}'}{\pi^2 (a^2 - r'^2)^{\frac{1}{2}}} \quad (2-13a)$$

$$\vec{K} = \frac{ik(a^2 - r'^2)^{\frac{1}{2}} \vec{H}_0}{\pi^2} \quad (2-13b)$$

From Eq. (2-9a), it is clear that the distribution of the surface magnetic current density  $K$  obtained in Eq. (2-13b) does not contribute appreciably to  $E$ . In Eq. (2-13b), the  $K$  is of the order of  $kaH_0$  and  $\text{grad } \Phi$  is of order  $1/a^2$ . The integral in Eq. (2-9a) over an area of order  $a^2$  makes the contribution of current density  $K$  to  $E$  of order  $kaH_0$ . Therefore, the normal component of  $E_0$  shall be of the same order as  $H_0$ . An additional magnetic current distribution  $K_E$  then is necessary for matching the boundary condition for  $E_n$ . This new current distribution, however, does not give rise to any extra magnetic charge density  $\eta$ . Thus,  $K_E$  must be:

$$\nabla \cdot \vec{K}_E = 0 \quad (2-14)$$

According to Eq. (2-7a) we can obtain

$$\vec{F} = \frac{1}{4} \vec{E}_0 \times \vec{r} \quad (2-15)$$

and from Eqs. (2-10) and (2-13a), the current for the required  $E$  is

$$\vec{K}_E = \frac{\vec{r}' \times \vec{E}_0}{2\pi^2 (a^2 - r'^2)^{\frac{1}{2}}} \quad (2-16)$$

Then the total magnetic current density in the aperture is

$$\vec{K} = \vec{K}_H + \vec{K}_E = \frac{1}{\pi^2} [ik(a^2 - r'^2)^{\frac{1}{2}} \vec{H}_0 + \frac{\vec{r}' \times \vec{E}_0}{2(a^2 - r'^2)^{\frac{1}{2}}}] \quad (2-17)$$

while the magnetic charge density is the same as Eq. (2-13b).

According to Eqs. (2-9a), (2-9b), and (2-17),  $E$  and  $H$  can be obtained by imposing them into Maxwell equations:

$$\vec{E} = \frac{1}{3\pi} \kappa^2 a^3 \phi_0 \hat{r} \times (2\vec{H}_0 + \vec{E}_0 \times \hat{r}) \quad (2-18a)$$

$$\vec{H} = -\frac{1}{3\pi} \kappa^2 a^3 \phi_0 \hat{r} \times (2\vec{H}_0 \times \hat{r} - \vec{E}_0) \quad (2-18b)$$

where  $\Phi_0 = e^{ikr} / r$  for  $r'=0$  and  $\hat{r}$  is unit vector in the direction of  $\vec{r}$ . Then, the Poynting vector  $S$  of the diffracted field is:

$$\vec{S} = \frac{c}{4\pi} \vec{E} \times \vec{H} = \frac{1}{36\pi^2} \frac{\kappa^4 a^6 \hat{r}}{r^2} (2\hat{r} \times \vec{H}_0 - \hat{r} \times \hat{r} \times \vec{E}_0)^2 \quad (2-19)$$

and the total transmitted radiation in all directions is:

$$S_{total} = \int_0^{\pi/2} \sin \theta \cdot d\theta \int_0^{2\pi} d\alpha r^2 |\vec{S}| = \frac{c}{27\pi^2} \kappa^2 a^6 (4|\vec{H}_0|^2 + |\vec{E}_0|^2) \quad (2-20)$$

The solution indicates that the total transmitted radiation through an aperture is proportional to the sixth power of the aperture size  $a$ . If we define the power throughput (PT) as the ratio of the total transmitted power to the incident power over the aperture. According to Bethe's theory, PT of a subwavelength aperture is proportional to the fourth power of the aperture size. Although this analytical solution provides a fundamental theory for calculating the transmission through an aperture, there are some theoretic restrictions and

premises. First, the metallic screen is assumed as a perfect conductor. Second, the assumption of symmetry of the aperture simplifies the field distribution. Furthermore, this solution is valid only when the aperture size is much smaller than the wavelength. Even through some literatures tried to modify Bethe's formula for greater accuracy, it is still impossible to derive analytical solution without any approximations and assumptions, especially for complex-shaped apertures. Therefore, in this thesis, we employ Finite-Difference Time Domain method (FDTD) to calculate power throughput and field profiles through our designed apertures.

## 2.2 Waveguide Theory

A waveguide is a special-designed structure that can guide waves through a long distance with acceptable energy loss. A typical waveguide structure consists of a high-index dielectric layer with a height  $h$  sandwiched with two lower-index materials, as shown in Fig. 2-3 [32]. The index of refraction of the guiding slab  $n_f$  must be larger than that of the cover material  $n_c$  or the substrate material  $n_s$  in order for total internal reflection to occur at the interfaces. If the slab is ideally infinite in extent in the  $yz$  plane, but finite in  $x$  direction, we can develop a basic form of guided modes using boundary conditions, which is applicable to real problems.

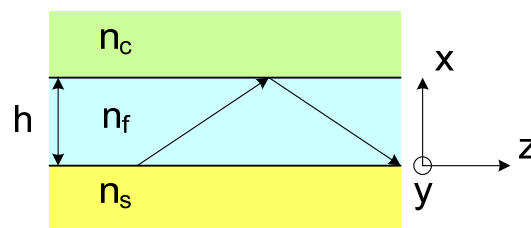


Fig. 2-3 A typical planar waveguide consisting of three layers arranged that guiding index of refraction ( $n_f$ ) is larger than the substrate ( $n_s$ ) and cover ( $n_c$ ) indices

For a sinusoidal transverse electric (TE) wave with a wave vector  $k$  and frequency  $\omega_0$ , the wave equation in each region can be put in the scalar form:

$$\nabla^2 E_y + k_0^2 n_i^2 E_y = 0 \quad (2-21)$$

where  $n_i = n_f, n_s,$  or  $n_c$ . Because the slab is infinite in  $y$  direction,  $E_y$  is a function of both  $x$  and  $z$  but independent of  $y$ . Due to the translational invariance of the structure along  $z$  direction, we assume that the amplitude does not vary along  $z$  axis but the phase does. If we choose a trial solution to Eq. (2-21) in the form:

$$E_y(x, z) = E_y(x) e^{-j\beta_i z} \quad (2-22)$$

where  $\beta$  is a propagation coefficient along  $z$  direction. Then by putting Eq. (2-22) into Eq. (2-21), we can obtain

$$\frac{\partial^2 E_y}{\partial x^2} + (k_0^2 n_i^2 - \beta^2) E_y = 0 \quad (2-23)$$

In the case  $\beta > k_0 n_i$ , we have a general solution with a real exponential form:

$$E_y(x) = E_0 e^{\pm \sqrt{\beta^2 - k_0^2 n_i^2} x} \quad (2-24a)$$

where  $E_0$  is the field amplitude at  $x = 0$ . This solution is the evanescent field of a total internal reflected wave at an interface.

In the case  $\beta < k_0 n_i$ , the solution has an oscillatory form:

$$E_y(x) = E_0 e^{\pm j \sqrt{k_0^2 n_i^2 - \beta^2} x} \quad (2-24b)$$

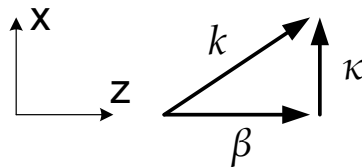


Fig. 2-4 Geometric relationship between longitudinal and transverse components  $\beta, \kappa$  of the wavevector  $k$



If a transverse wavevector  $\kappa$  is defined as  $\kappa = \sqrt{k_0^2 n_i^2 - \beta^2}$ ,  $\beta$  and  $\kappa$  are geometrically related to the total wavevector  $k = k_0 n_i$ , as shown in Fig. 2-4, inside the guiding layer.

The longitudinal wavevector  $\beta$  is used to identify individual modes and also defined as the eigenvalue of the mode. A guided wave must satisfy the condition,

$$k_0 n_s < \beta < k_0 n_f \quad (2-25)$$

where it is assumed that  $n_c \leq n_s$ . To find the values of  $\beta$  that lead to solutions to the wave equation, the boundary condition is applied to Eqs. (2-24a) and (2-24b). Then the transverse electric field amplitudes in the three regions are

$$E_y(x) = Ae^{-\gamma_c x} \quad 0 < x \quad (2-26a)$$

$$E_y(x) = B \cos(\kappa_f x) + C \sin(\kappa_f x) \quad -h < x < 0 \quad (2-26b)$$

$$E_y(x) = De^{-\gamma_s(x+h)} \quad x < -h \quad (2-26c)$$

where  $A$ ,  $B$ ,  $C$ , and  $D$  are amplitude coefficients to be determined,  $\gamma_c$  and  $\gamma_s$  are attenuation coefficients in the cover and substrate, respectively, and  $\kappa_f$  is the transverse component of  $k$  in the guiding layer. According to the boundary condition that tangential component of field is continuous at the interfaces, the characteristic equation to get the eigenvalue of propagation coefficient for a TE wave is

$$\tan(h\kappa_f) = \frac{\gamma_c + \gamma_s}{\kappa_f \left(1 - \frac{\gamma_c \gamma_s}{\kappa_f^2}\right)} \quad (2-27)$$

The characteristic equation clearly shows that the propagation mode supported by the waveguide is highly dependent on the refractive indices of materials and the dimension of the guiding layer, height  $h$ .

For a complex waveguide, a two-dimensional structure can be decomposed into two spatially orthogonal waveguides: a horizontal and a vertical slab waveguide. The propagation coefficient  $\beta$  of the waveguide can be found by using the solutions to these two orthogonally oriented waveguides based on the techniques developed. This method is known as the effective index method. Consider a buried rectangular waveguide shown in Fig. 2-5. The waveguide is decomposed into a thin waveguide and a thick one. The thin part is analyzed in terms of the actual indices of the structure; while the thick part is analyzed using the effective index from the first analysis.

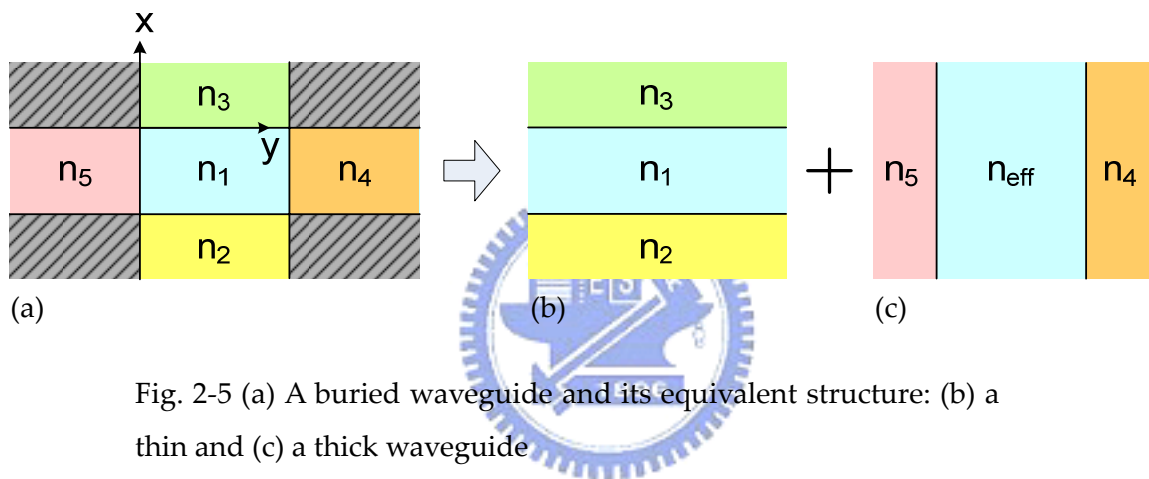


Fig. 2-5 (a) A buried waveguide and its equivalent structure: (b) a thin and (c) a thick waveguide

Once the propagation coefficient  $\beta$  of the thin slab waveguide is obtained for a specific wavelength and mode of interest, the effective index of the slab is determined through the following expression

$$n_{eff} = \frac{\beta}{k_0} \quad (2-28)$$

where  $k_0$  is the vacuum wavevector of the light being guided. The effective index then is used to replace the original refractive index for the guiding layer in the thick waveguide to calculate the propagation coefficient of this waveguide. Then the value of propagation coefficient found from the last step is the value for the mode we want.

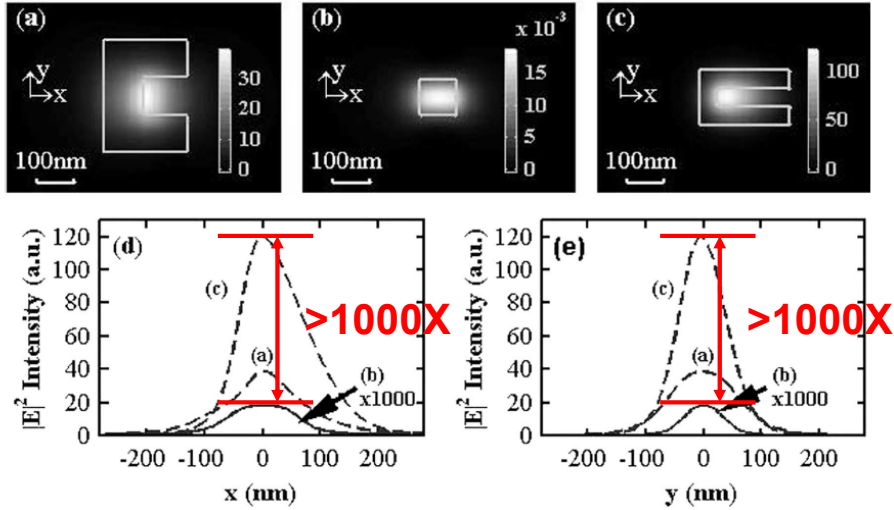


Fig. 2-6  $|E|^2$  distribution at 48 nm from (a) C-shaped, (b) square, and (c) modified C-shaped apertures and  $|E|^2$  cross section along (d) X and (e) Y axis

Due to the nature of low energy loss, the waveguide theory was applied to enhance the transmission through subwavelength apertures. X. Shi *et al.* first proposed a C-shaped aperture that enhances the peak transmitted electric field intensity by 3 orders of magnitude compared to that of a square aperture, as shown in Fig. 2-6 [33]. The enhancement was explained by considering the C-shaped aperture as a waveguide. Owing to the boundary condition, the cut-off wavelength and the propagation modes of the aperture are determined by the dimensions of the gap area, especially the gap width. Because of the particular orientation of the polarization of the propagation modes, an incident field with the polarization perpendicular to the ridge edge induces strong coupling into the propagation modes and results in higher transmission. A peak in the spectral response corresponding to a wavelength close to that of the incident light also confirmed that a resonant transmission at the incident wavelength is related to the propagation mode of the aperture. Moreover, because the mode field is confined to a relatively small area around the concave part of the aperture, the spot size is almost the same as the ridge width. It means a subwavelength spatial resolution can be achieved by reducing the

ridge size of a C-shaped aperture.

## 2.3 Surface Plasmon Polaritons

In physics, plasma is an ionized state of matter. The presence of free electrons which is not bound to an atom or molecule makes the plasma electrically conductive. Therefore plasma, the electron density, responds strongly to electromagnetic fields and resonates at a specific frequency defined as the plasma frequency. In free-electron-like metals, the dielectric constant can be expressed by Drude model [34]

$$\varepsilon_m(\omega) = 1 - \left(\frac{\omega_p}{\omega}\right)^2 \quad (2-29a)$$

$$\omega_p = \sqrt{\frac{4\pi n e^2}{m}} \quad (2-29b)$$

where  $\omega_p$  is the plasma frequency,  $n$  is the electron density,  $e$  is the electric charge of a electron, and  $m$  is the mass. Then according to the wave equation, the dispersion relation can be obtained

$$k^2 = \frac{\omega^2}{c^2} \varepsilon(\omega) = \frac{\omega^2}{c^2} \left(1 - \frac{\omega_p^2}{\omega^2}\right) \quad (2-30)$$

Eq. (2-30) indicates that if the frequency of incident light is below the plasma frequency, the light can not penetrate through the metal and the skin depth is  $1/|k|$ .

As photons are quantization of light, plasmon is the quasiparticle resulting from the quantization of plasma oscillations. Thus, plasmons are collective oscillations of the free electron gas density, often at optical frequencies. If those plasmons occur at the interface between a vacuum or material with a positive dielectric constant and that of a negative dielectric constant and are confined to surfaces, they are defined as surface plasmons. Consequently, surface plasmons

are charge density waves propagating along a dielectric-metal interface. Furthermore, the quasiparticles resulting from the strong coupling of electromagnetic waves with an electric or magnetic dipole-carrying excitation are called polaritons. Therefore, a surface plasmon polariton (SPP) is a combined excitation consisting of a surface plasmon and a photon. Since the wave is on the boundary of the metal and the external medium, these oscillations are very sensitive to boundary conditions.

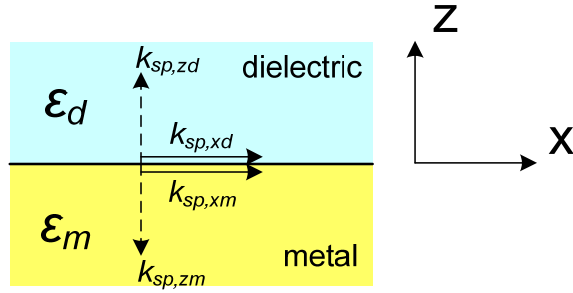


Fig. 2-7 Schematic illustration of surface plasmons propagating along the dielectric-metal interface induced by a p-polarized incident light

To characterize surface plasmon polaritons, consider a p-polarized electromagnetic wave propagating along a dielectric-metal interface, as shown in Fig. 2-7. According to Maxwell's equations and boundary conditions, the dispersion relation of surface plasmon polaritons can be obtained,

$$k_{sp,xd} = k_{sp,xm} = \frac{\omega}{c} \left( \frac{\epsilon_d \cdot \epsilon_m}{\epsilon_d + \epsilon_m} \right)^{1/2} \quad (2-31a)$$

$$k_{sp,zi} = \left[ \epsilon_i \left( \frac{\omega}{c} \right)^2 - k_x^2 \right]^{1/2}, \quad i = d, m \quad (2-31b)$$

where  $\epsilon_d$  and  $\epsilon_m$  is the dielectric constant of dielectric material and metal, respectively. For most dielectric materials, their dielectric constants are positive; while dielectric constants of metal are negative and usually their absolute values are greater than that of dielectric materials when the frequency of incident light is below the plasma frequency. Therefore, from Eq. (2-31a),

wavevector along x direction is real, i.e. surface plasmons propagate along the metallic surface.

The wavevector of surface plasmons along z direction, i.e. perpendicular to the surface, is always imaginary according to Eq. (2-31b). It implies that magnitude of electromagnetic fields along z direction decays exponentially. Therefore, we can conclude that surface plasmons are an evanescent field which will not propagate out of the surface. Since the dielectric constants of real metal are also complex, the imaginary part represents exponential decay on magnitude when surface plasmons propagate along the surface.

In addition, we can find

$$k_{sp,x} = \frac{\omega}{c} \left( \frac{\epsilon_d \cdot \epsilon_m}{\epsilon_d + \epsilon_m} \right)^{1/2} > \frac{\omega}{c} \epsilon_d^{1/2} \quad (2-32)$$

It means that the magnitude of the wavevector of surface plasmons is greater than that of incident light. Fig. 2-8 shows the comparison of dispersion curves of surface plasmons and incident light. Because the dispersion curve of surface plasmons lies right of that of incident light, the incident light with frequency of  $\omega$  will not be able to excite surface plasmons.

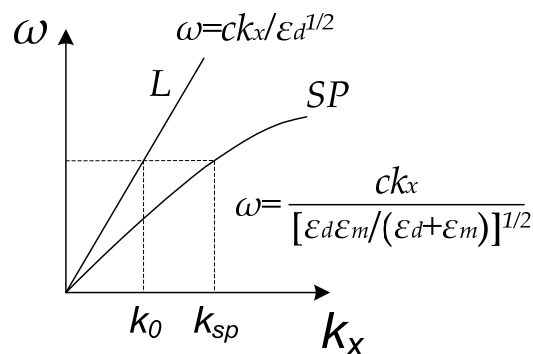


Fig. 2-8 Dispersion curve of surface plasmons and incident light

Therefore, to excite SPPs by photons, an additional wavevector is necessary

for fulfilling the momentum matching condition. There are two common methods: either introducing a periodic structure, such as gratings, corrugations, or a hole array, to provide an additional wavevector or inducing attenuated total reflection (ATR) in the interface to increase the wavevector of incident light, as shown in Figs. 2-9 (a) and (b).

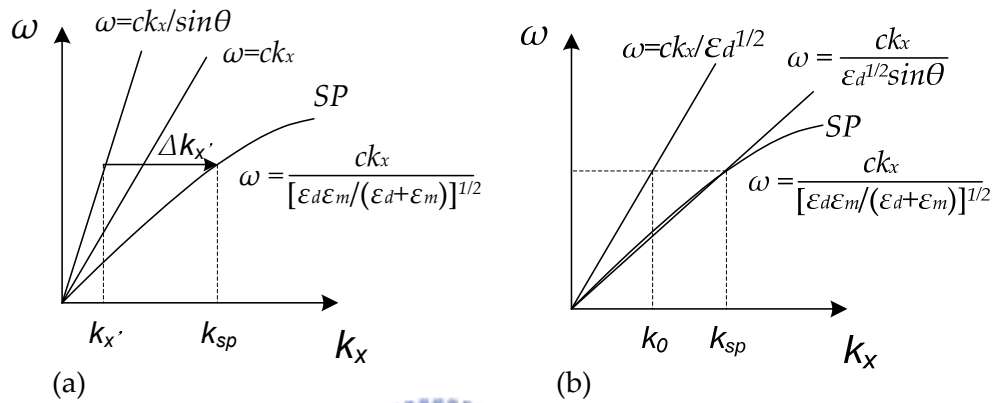


Fig. 2-9 Excite surface plasmon polaritons by (a) a grating structure and (b) attenuated total reflection

Due to the sensitive dependence of excitation of surface plasmons on the boundary conditions of a metal-dielectric interface, the excitation of surface plasmons is used in surface plasmon resonance (SPR). In SPR, the excitation of surface plasmons as a function of incident angle or wavelength is obtained by detecting the reflected power from a prism coupler. Any perturbation in the refraction index, the absorption, or topography will reflect a substantial change in SPR reflectivity. Therefore, this technique can be widely used to observe insignificant variation in thickness, density fluctuations, or molecular adsorption.

Another remarkable application of surface plasmons is to enhance the transmission through subwavelength apertures. T. W. Ebbesen *et al.* demonstrated extraordinary transmission through subwavelength hole arrays or a aperture surrounded with corrugations that breaks through the theoretic

limit predicted by Bethe's theory, as shown in Fig. 2-10 [35-36]. According to the surface plasmon theory, with the aid of a periodic structure, such as hole arrays or corrugations, surface plasmon waves that propagate along the interface can be induced. When the period of the structure is half of the effective wavelength of the SPP mode, SPP standing waves which are a combination of electromagnetic waves and surface charges are generated. The electromagnetic field perpendicular to the surface is evanescent, i.e. an exponential decay with the distance away from the surface. It indicates a non-radiative wave to prevent power propagating from the surface. The enhancement of the transmission can be explained by considering the interaction between the incident light and the surface plasmon modes.

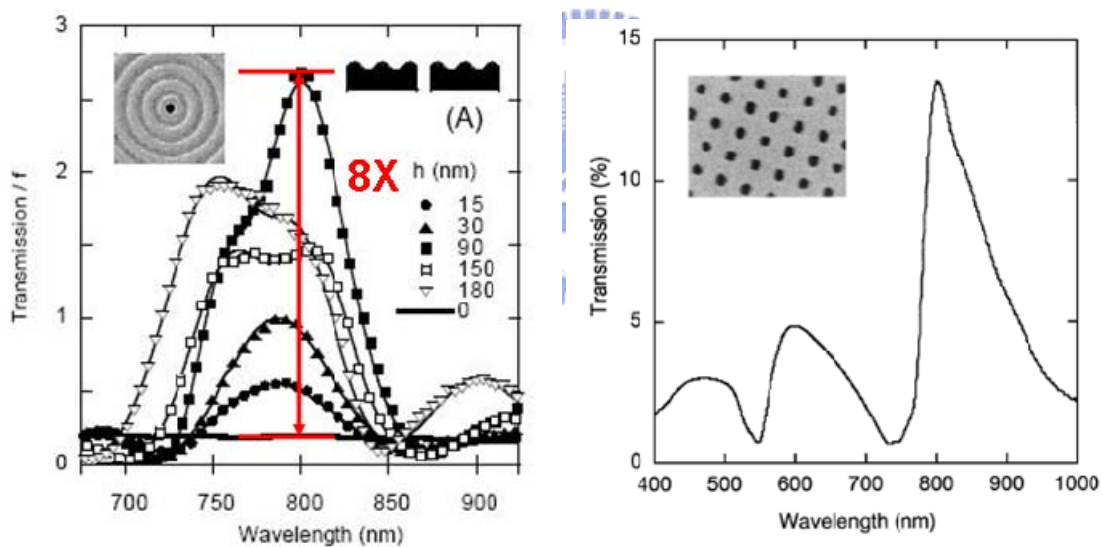


Fig. 2-10 Transmission spectrum of (a) a circular aperture surrounded with a corrugation structure and (b) a hole array

Consider a hole array in a metal film of dielectric constant  $\epsilon_m$  sandwiched with two lossless dielectric media of dielectric constants  $\epsilon_1$  and  $\epsilon_2$ , respectively, as shown in Fig. 2-11. In the absence of resonant SPP modes, the energy transfer between the photons on the opposite side is considerably inefficient and thus the transmission is extremely low. In contrast, resonant SPP modes excited by



photons at one of the interfaces enhance the transmission by the diffraction of the evanescent field resulting from SPP modes, indicating the scatter of the field leading to the formation of transmitted light.

In the case of a thin film, interaction between the opposite interfaces makes surface plasmons modes split into two types: symmetric modes of lower frequency and anti-symmetric modes of higher frequency. Only anti-symmetric SPP modes induce field enhancement near the metal surface because of longer propagation length, which is inversely proportional to the square of the film thickness. Therefore, the tunneling effect through a thin metal film has to be taken into consideration and dominates the transmitted field.

If the metal film is thick enough, the interaction between SPPs in the opposite interfaces is ignored. Then the corresponding SPP modes induced by incident light propagate independently along the surface with wave vector  $k_{sp}$  and decays from the surface exponentially with the attenuation constant  $k_z$ . The interaction between the incident light and the SPP modes will occur in three different ways.

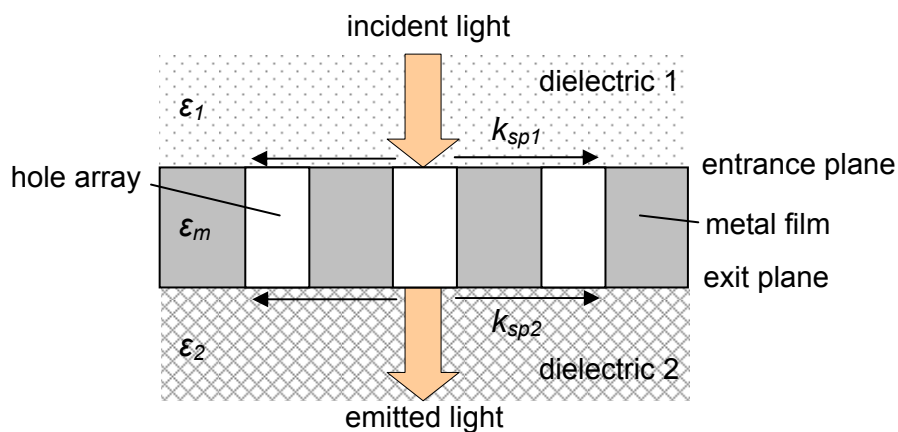


Fig. 2-11 Configuration of a hole array in a metal film sandwiched with two dielectric materials

1. In the entrance interface, incident light couples to SPP modes. The

evanescent field is enhanced by SPP modes and the transmission through the holes is increased. In the meantime, the field is also scattered by the periodic array so that some waves are produced accordingly.

2. Incident light cannot couple to SPP modes in the entrance interface. But the incident light that is weakly transmitted through the holes fulfills the boundary conditions of the exit plane so that SPP modes are induced in the exit interface. The electric field enhanced by the SPP modes increases the transmission. Some transmitted light out of the exit plane is also generated as a result of the scattering of the field.

3. If the boundary conditions allow the excitation of SPP modes to take place in both sides of the metal film, the field is influenced by the SPP modes in two interfaces. As a result, the incident field near the interfaces is enhanced by the induced field resulting from the SPP modes.

Furthermore, the interaction between double resonances on both sides delivers energy through the film without exponential decrease and thus results in strong field enhancement. Therefore, SPP modes function like an electromagnetic energy carrier. The incident energy is converted to non-radiative SPP resonance by coupling light into SPP modes and then transferred to a propagating wave in the form of re-radiation from the field induced by SPP modes. According to this model, the transmitted field is predicted to be enhanced up to  $10^4$  times than that without the SPP modes.

## 2.4 Summary

When an incident field fulfills the boundary conditions of a waveguide, the field can couple into specific propagation modes and propagate through the waveguide with less energy dissipation. If the incident field can excite the

oscillation of surface plasmon waves on both sides of a metallic film with the aid of a periodic structure or attenuated total reflection, the transmission through the film can be enhanced accordingly. Either propagation modes or surface plasmon polaritons modes can increase the transmission through a subwavelength aperture significantly and break through the theoretic limit that Bethe predicted. These literature reviews stimulate a novel idea of inducing these two effects simultaneously, which we name it as the hybrid effect.





# Chapter 3 Modeling of Hybrid Effect in Transmission Enhancement

According to the theories explained in Chapter 2, for a subwavelength aperture in a metal film, either propagation modes supported by the aperture or SPP modes on either side of the metal film can enhance the transmission through the aperture. However, the transmission enhancement is not sufficient enough for near-field storage applications. Therefore, we propose a novel design that makes both propagation modes and surface plasmon modes exist simultaneously and thus further increase the transmission through the subwavelength aperture.

In this chapter, the transmission of a C-shaped aperture surrounded with a corrugation or illuminated by obliquely incident light is modeling and investigated by employing a numerical calculation method. The coexistence of SPP modes and propagation modes that can increase the transmission is demonstrated and named as the hybrid effect. The geometric effect of a C-shaped aperture is optimized and followed by the study of the effect of either a corrugation structure on each side of the metal film or oblique illumination on the transmission through the optimized aperture. We also discuss and analyze the correspondence between those parameters and the transmission.

## 3.1 Methodologies and Parameters

The transmission and the transmitted field are calculated and investigated numerically in a simulation model by employing Finite-Difference Time Domain (FDTD) method. The FDTD method is a grid-based differential time-domain numerical modeling method. The calculation domain where the

simulation performs is divided into cells, unit spaces formed by grids. A source is assigned to launch into the domain. Inside every cell, the time-dependent Maxwell's equations in partial differential form are discretized using central-difference approximations to the space and time partial derivatives. Because the change in the time derivative of the electric field is dependent on the change in the curl of the magnetic field, the electric field vector components in a cell are solved at a given moment and then the magnetic field vector components are solved in the same cell at the next moment. The process repeats to evolve the electromagnetic fields forward in time.

Since FDTD is a grid-based numerical method, the entire calculation domain has to be gridded and the grid size must be sufficiently small to resolve the wavelength and the smallest geometrical dimension. This implies that a fine grid will unavoidably result in enormous resource consumption and computation time. Therefore, according to the simulated model, some assumptions or approximations are necessarily made to localize the computation area. In addition, perfectly matched layers (PML) are implemented as absorbing boundaries of the calculation domain to simulate an infinite domain.

In the following sections, an optical model for simulation in the transmission through subwavelength apertures is established based on the premises we made. The parameters used as an evaluating factor and simulation variables are also explained.

### **3.1.1 Optical Model and Premises**

According to the mechanism of excitation of SPP modes, the complex dielectric constants of interface materials determine the boundary condition and the SPP propagation length and consequently dominate the field enhancement

induced by the SPP modes. Higher SPP resonances will be induced as the metal material is closer to the ideal metal ( $-\epsilon' \gg \epsilon''$ ), and thus result in higher transmission [37]. Therefore, at a wavelength of 633 nm for the cut-off of single-mode optical fibers, silver is chosen as the film material due to its complex dielectric constant  $\epsilon = \epsilon' + i\epsilon''$  of  $-15.9 + 1.1i$ .

The depth of apertures which is equal to the film thickness also plays an important role on the transmission enhancement [38]. Because charges in a conductive material oscillate with the same frequency of an electromagnetic wave impinging on the surface, the interaction between the electromagnetic wave and the material induces an electric current of which magnitude decays with the depth of the material. The skin depth is defined as the distance which the current falls to  $1/e$  of its greatest value at the surface. Since the metal film is used to confine the incident field into a tiny area, it must be thick enough to prevent the incident light directly penetrating through the film. Otherwise, the penetrating field will broaden the effective spot size in near field. In addition, in the case of a thin film, the coupling between SPP modes on opposite sides of the film results in a distinct coupled mode and provides a channel that allows more energy to pass through the film. In contrast, if the film thickness exceeds a certain value so that no coupling occurs between SPP modes in two interfaces, the penetration of the field is suppressed and the transmission enhanced by the SPP modes reduces with the increase of the thickness. The sufficient thickness to suppress the coupling effect depends on the film material and the geometry of apertures. Therefore, there is a tradeoff between the effective spot size and the transmission. Since the sufficient thickness of a silver film ranges from 200 to 300 nm, we choose 200 nm in our simulation.

The incident field is assumed to be a plane wave within a calculation domain as a general study of SPP effect on the transmission. The range of the calculation domain depends on several considerable factors. The effective area

where SPP modes contribute to the transmission enhancement is determined by the illumination area and the propagation length of SPP waves along the interface. It means that outside the effective area the influence of SPP modes on the transmission can be ignored. Compared to the propagation length in a free-standing silver film typically greater than 10  $\mu\text{m}$ , the spot size of a 633-nm laser beam focused by a objective lens with NA=0.25 is estimated around 3  $\mu\text{m}$ . This indicates that, in this case, the spot size dominates the effective area. Moreover, with the increase of the calculation domain, the exponential increase of resource consumption is also unavoidable because FDTD is a grid-based numerical method. Therefore, if we consider that the dimensions of subwavelength apertures are less than 0.3  $\mu\text{m}$ , which is less than one-tenth of the spot size, the calculation domain is assigned 0.6  $\mu\text{m}$ . This plane-wave approximation can stand within the calculation domain because the focused spot illuminating the aperture is much larger than the calculation domain.

Based on the assumptions made previously, the optical model for studying the transmission through subwavelength apertures is established and all the variables are defined in Fig. 3-1. The middle point of the ridge length in the entrance plane is the origin. The XY plane denotes the entrance plane while the X axis is perpendicular to the ridge length and the Y axis is parallel to the ridge length. The Z axis denotes the propagation direction. A transverse-magnetic (TM) plane wave with a free-space wavelength of 633 nm illuminates a 200-nm silver film with an incident angle  $\Phi$  relative to the Z axis as the XZ plane is the plane of incidence. In the case of corrugation structures, the C-shaped aperture is encircled by a circular groove with a width  $w$  and a radius  $p$ . Compared to a free-standing membrane in the corrugation case, the silver film is deposited on a glass substrate with a refractive index of 1.475 at the wavelength of 633nm in the case of oblique illumination. A virtual monitor is positioned 50 nm away from the exit plane with the normal direction pointing to the Z axis to calculate



the transmitted power.

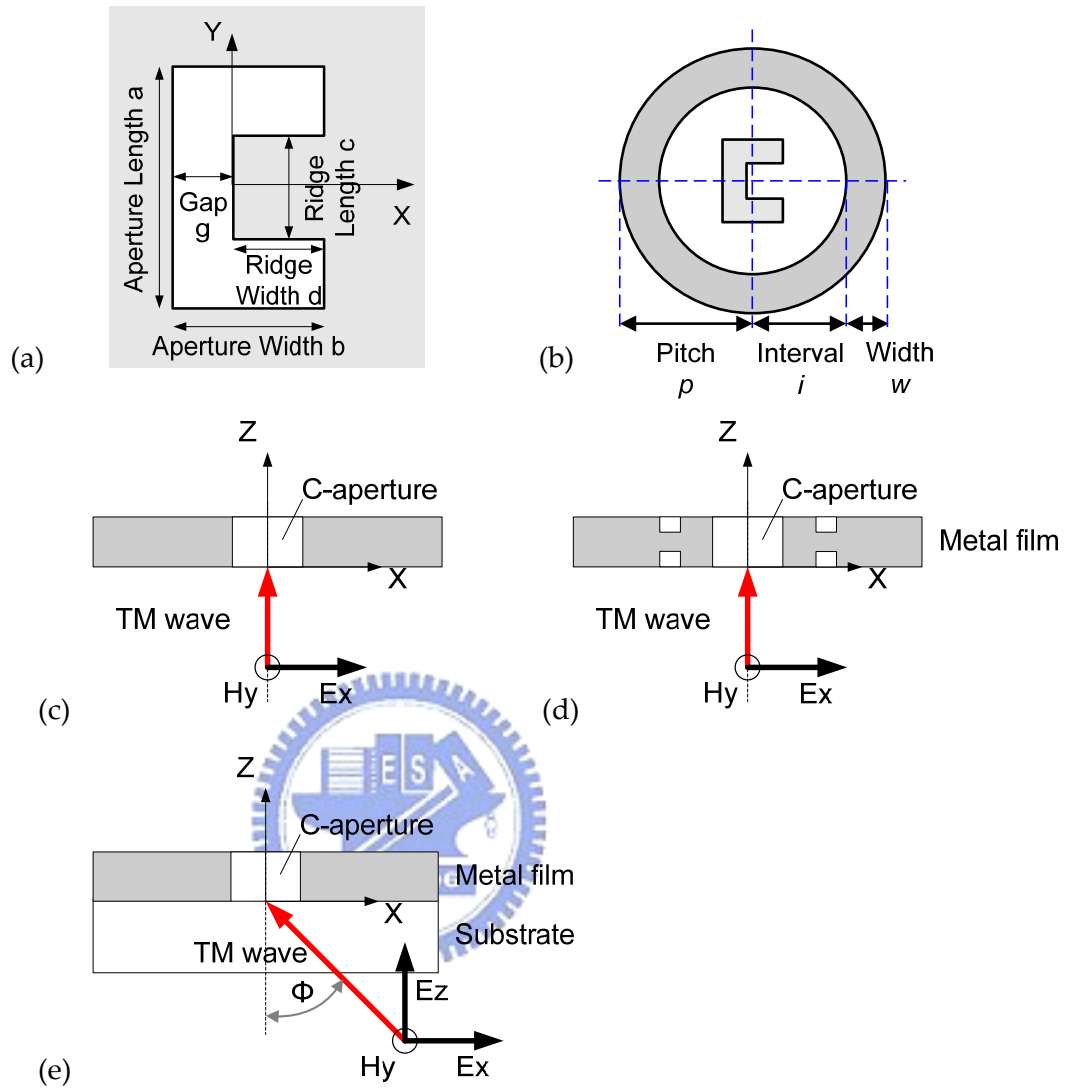


Fig. 3-1 Dimensional parameters of (a) a C-shaped aperture and (b) a groove surrounding a C-shaped aperture and transmission model through (c) a C-shaped aperture, (d) a C-shaped aperture surrounded with a corrugation, and (e) a C-shaped aperture with oblique illumination

### 3.1.2 Parameters

The power throughput (PT) is used as an evaluating factor to evaluate the performance of subwavelength apertures and to optimize the dimensions of

apertures, geometry of corrugations, and incident angles. The power throughput is defined as the ratio of the transmitted power to the incident power over the aperture, which is equal to the incident power density times the aperture area. The definition of the PT is shown in Eq. 3-1,

$$PT \equiv \frac{P_t}{P_{iS}} = \frac{P_t}{d_p \cdot S_A}, \quad (3-1)$$

where  $P_t$  is the transmitted power,  $P_{iS}$  is the incident power over the aperture area  $S$ ,  $d_p$  is the incident power density, and  $S_A$  is the aperture area.

The physical meaning of the PT represents the photon capturing capability. If the PT is equal to unity, it means all the photons impinging on the aperture area can be transported to the exit plane of the aperture. When the PT is greater than unity, some photons obstructed with the metal film can be captured by the aperture and propagates through the aperture until they reach the exit plane of the aperture. Therefore, a higher PT corresponds to higher photon capturing capability and higher transmission of the aperture.

To optimize the dimensions of a C-shaped aperture, the gap width, the ridge length and the aperture aspect ratio of the aperture width to the aperture length are simulation variables. According to waveguide theories, the gap width is a critical parameter that determines the propagation modes and the ridge length alters the boundary conditions. A large ridge length or a small gap width leads to a slit-like behavior while a small ridge length or a large gap width makes the aperture perform like a square aperture.

To investigate the hybrid effect, the optimized C-shaped aperture is surrounded with a groove or illuminated at oblique incident angles. Therefore, the dimensions of the groove, including the pitch, the interval, and the width, and the incident angle are simulation variables. Except for the PT as a function of those parameters, the field profiles and the spectral response are also

calculated to examine more information about the mechanism of the hybrid effect.

## 3.2 Nano-waveguide Design

According to waveguide theories presented in Chapter 2, propagation modes supported by a waveguide depend on the wavelength of incident light and the geometry and dimensions of the waveguide. Therefore, prior to the study of the hybrid effect, the dependence of the transmission on the dimensions of a C-shaped aperture is studied and the dimensions are optimized to obtain the maximum transmission for the incident wavelength of 633 nm.

### 3.2.1 Rectangular Apertures

The power throughput and spot sizes at 50nm away from a rectangular aperture as a function of the side length are calculated as a comparison base for following study. The simulation result in Fig. 3-1 shows that the PT through a square aperture in a finite-conducting metal film is approximated as a fourth power function of the side length. The behavior generally obeys the trend predicted by Bethe's theory. However, the exact value can only be obtained by numerical methods because of the difference between real metal materials and perfect conductors. It also implies that no propagation mode exists in a square aperture at a wavelength of 633 nm.

Spot sizes of the square apertures along X and Y axis are listed in Table 3-1. The spot sizes in the X direction generally are larger and also have higher variations in the change of aperture sizes than that in the Y direction. This is because X-polarized light is used to illuminate the aperture. Two edges of the aperture perpendicular to the polarization result in two local intensity maximums and thus broaden the spot size. The location of the two local

maximums is determined by the aperture edges so the spot size in the X direction is almost linearly proportional to the aperture size. In contrast, the spot size in the Y direction slightly decreases with the reduction of the aperture size. Since spot sizes are the dominate factor to determine the spatial resolution, we chose the 60-nm aperture whose PT is  $6.4 \times 10^{-5}$  as a comparison base.

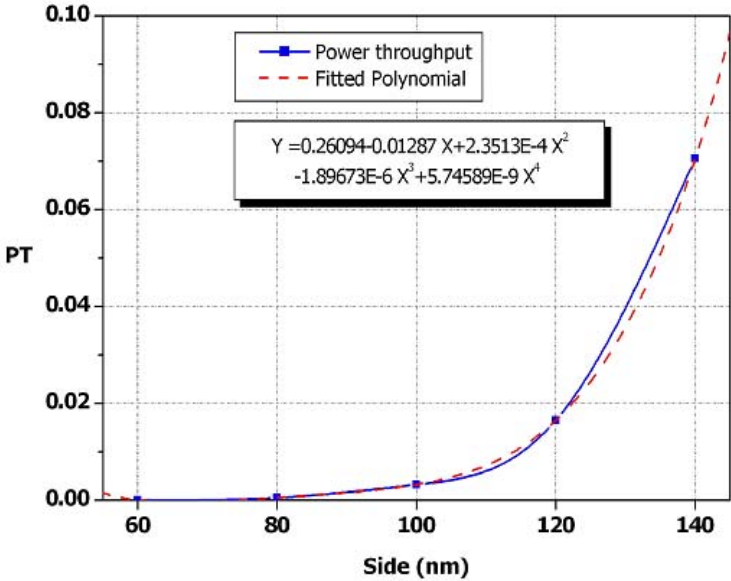


Fig. 3-2 The PT as a function of the side length of a square aperture

Table 3-1 Spot sizes at 50 nm away from square apertures

Side (nm*nm)	Spot Size (nm)	
	X	Y
60*60	147	111
80*80	164	108
100*100	185	125
120*120	222	138
140*140	231	133

### 3.2.2 Optimization of Ridge Part

The first step to optimize the C-shaped aperture is to fix the aperture

dimensional variables  $a$  and  $b$  as 210 nm and 84 nm and analyze the dependence of transmission on the ridge length  $c$  and gap  $g$ . The simulation result in Fig. 3-3 shows that gap  $g$  is a dominate parameter to determine the power throughput through the waveguide. The PT gradually increases with the decrease of the gap and reaches a peak of 1.8 when the gap is 38 nm. As the gap is less than 38 nm, the PT drops dramatically. The drop as the gap less than a specific value indicates a cut-off for the incident wavelength regardless of ridge length  $c$ . This characteristic behaves like a waveguide. The cut-off wavelength of a specific propagation mode is determined by the geometry and dimensions of the waveguide. When the incident wavelength is above the cut-off wavelength, the corresponding propagation mode can not be supported within this waveguide.

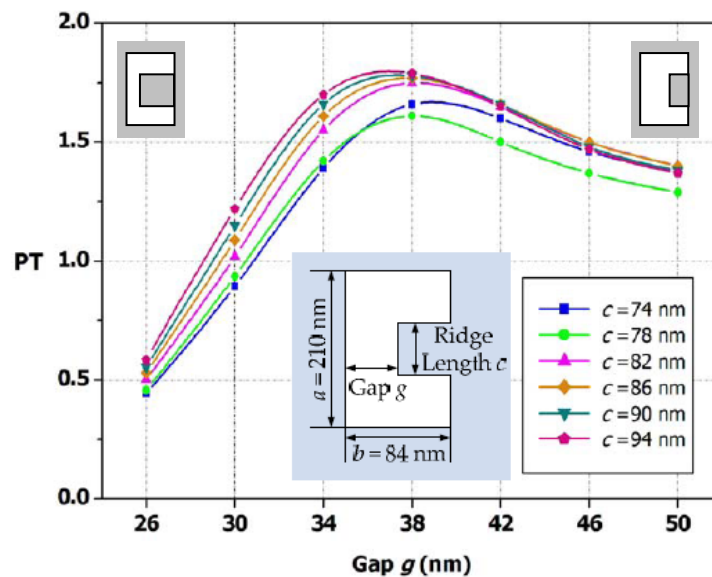


Fig. 3-3 The PT as a function of gap  $g$  with various ridge lengths  $c$

In contrast to the gap, the ridge length  $c$  has a minor influence on the transmission. Instead, the ridge length alters the boundary conditions that determine the spot size along Y axis. Therefore, the spot size along Y axis increase with the increase of the ridge length.

### 3.2.3 Optimization of Aperture Part

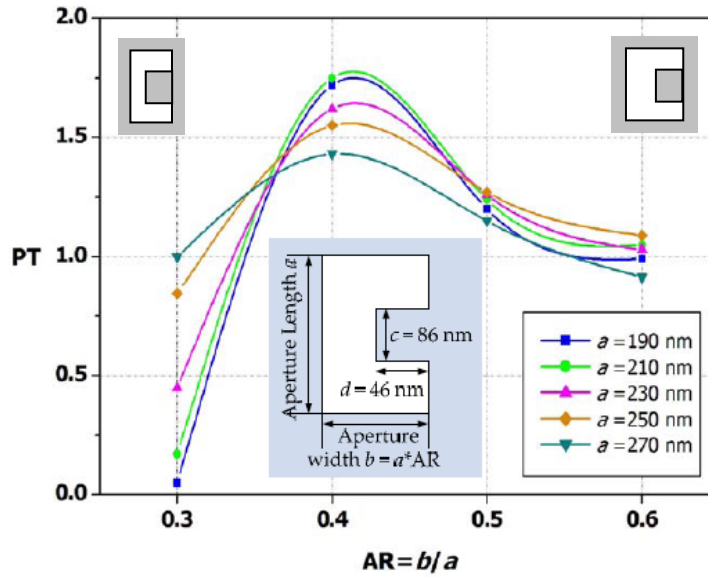


Fig. 3-4 The PT as a function of aspect ratio  $AR$  with various aperture lengths  $a$  as ridge width  $d$  is 46 nm

Based on the results in the previous section, the second step is to analyze the influence of aperture length  $a$  and aspect ratio  $AR$ , defined as the ratio of aperture width  $b$  to aperture length  $a$ , on the PT as ridge length  $c$  and ridge width  $d$  are kept 46 nm and 86 nm, respectively. The PT reaches a peak at aspect ratio of  $\sim 0.4$  regardless of various aperture lengths, as shown in Fig. 3-4. This cut-off characteristic exhibits that a C-shape aperture behaves like a single ridge waveguide. If the ridge area is relatively small compared to the aperture size, the ridge waveguide effect vanishes. The PT of the aperture will have similar tendency with that of a rectangular aperture. This explains a reduction in the maximum PT with an increase of the aperture size and a fixed ridge part. In contrast, if the aperture shrinks, the ratio of the ridge area to the aperture increases and consequently the gap is reduced. The PT of the aperture will behave like a nano slit so the PT has a sharp peak as the aperture area decreases.

Since the gap  $g$ , which is equivalent to  $(a \times AR - d)$ , is a dominant factor to determine propagation modes of a waveguide, we calculate the PT as a function of the aspect ratio with a different aperture width  $d$ . Our calculation, as illustrated in Fig. 3-5, shows a similar result as that in Fig. 3-3 but yields a higher peak value of PT. For a curve with a fixed aperture length, the change in the aspect ratio indicates the change in the ratio of the slit part and also the gap. Therefore, for a specific ridge width, there is a corresponding gap that determines corresponding propagation modes and consequently a peak PT.

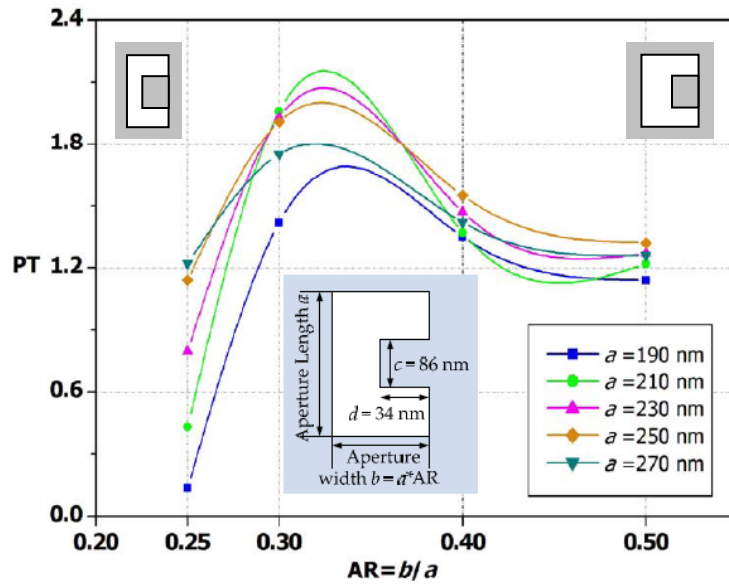


Fig. 3-5 The PT as a function of aspect ratio  $AR$  with various aperture lengths  $a$  as ridge width  $d$  is 34 nm

In summary, according to our simulation results, the maximum PT exhibits an optimized design. The dimensions of the optimal C-shaped aperture has an aperture length  $a$  of 210 nm, an aperture width  $b$  of 84 nm, a ridge length  $c$  of 86 nm, and a ridge width  $d$  of 34 nm. Since a C-shaped aperture function like a waveguide, we will study the coupling effect between SPP modes and propagation modes of the aperture by employing this optimal design.

### **3.3 Nano-waveguide with Corrugations**

The simulation results in the previous section demonstrates that a C-shaped aperture functions as a ridge waveguide and a peak of PT represents a propagation mode supported by the waveguide for a specific incident condition. Consequently, in this section, we investigate the effect of a corrugation on the transmission through the optimized waveguide. The further transmission enhancement resulting from the hybrid effect that propagation modes and surface plasmons modes coexist is demonstrated accordingly.

#### **3.3.1 Corrugations in Entrance Interface**

To yield a coupling effect between SPP modes and propagation modes in a subwavelength aperture, the optimal C-shaped aperture in a free-standing silver film is surrounded with a corrugation in the entrance interface of the film. The configuration of the optical model is shown in Fig. 3-1 (d). Our simulation, as shown in Fig. 3.6, reveals the power throughput of a C-aperture surrounded with a corrugation in the entrance interface is higher than that of a single C-aperture. The power throughput enhancement can reach as high as 3.61. According to the discussion in section 2.3, if incident light can be coupled into SPP modes in the entrance interface, the field near the interface and inside the aperture will be enhanced by the scattering of evanescent waves in the interface. As expected, if the aperture is replaced with a ridge waveguide, propagation modes inside the waveguide are also enhanced by this effect. Therefore, the transmission through the C-shaped aperture is further enhanced with the aid of SPP modes in the entrance interface.

Corrugations in the interface can be treated as an energy well and the width of the energy well determines how many and which modes exist.



Therefore, curves with different tendency in Fig. 3-6 represent different sets of SPP modes produced by different groove widths. In contrast, interval  $i$  changes the field distribution resulting from the superposition of SPP modes which carries different momentum and energy. Thus each curve in Fig. 3-6 indicates different combination of SPP modes and produce different power throughput. The higher power throughput implies a more efficient coupling between incident light and SPP modes due to momentum and energy conservation matching conditions.

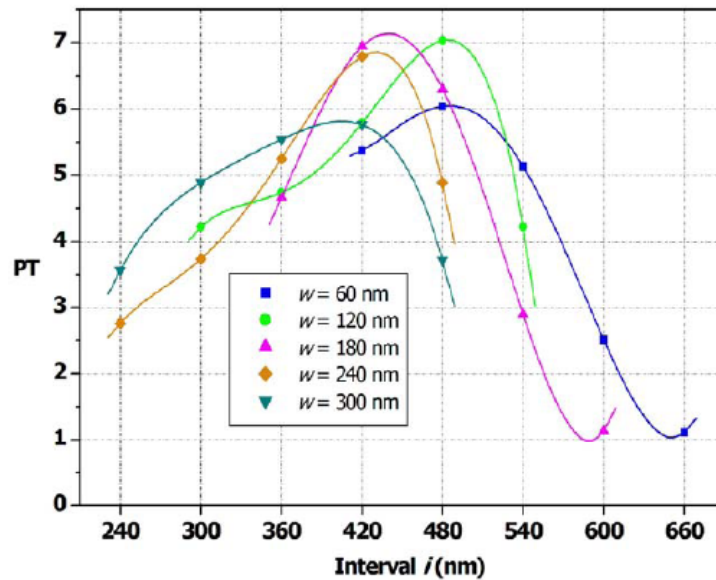


Fig. 3-6 The PT as a function of the interval  $i$  with various widths  $w$

The groove pitch  $p$  dominates the lattice momentum of the groove structure as well as the momentum matching condition of the interaction between the photons and the surface plasmons. It means the probability of the coupling between photons and surface plasmons is determined by the groove pitch. This mechanism explains a concave curve of each power throughput with a peak at pitch of 620 nm in Fig. 3-7.

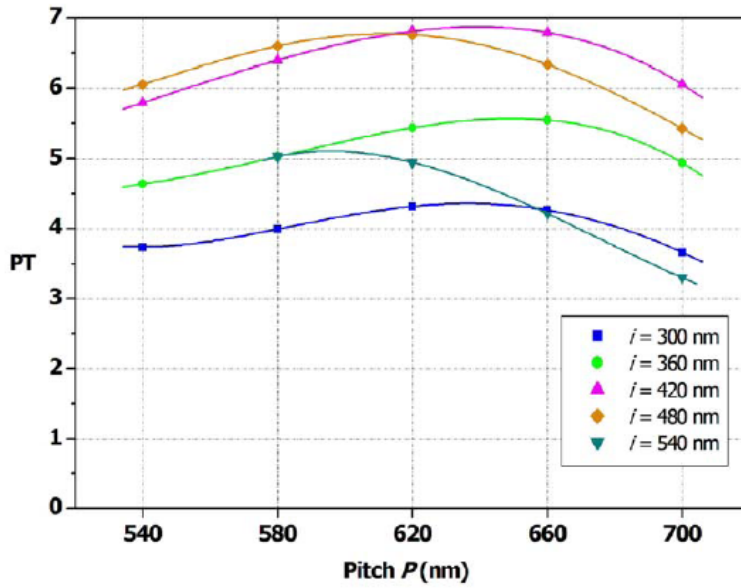


Fig. 3-7 The PT as a function of pitch  $p$  with various interval  $i$

Compared to a single C-shaped aperture, the power throughput can be further enhanced by surrounding the aperture with a corrugation. The enhancement stimulated by the corrugation structure is defined as the ratio of the power throughput of the C-shaped aperture with a groove to that without a groove. The maximum enhancement of 3.61 can be obtained in our simulation. It means that the output power through this design is 3.61 times higher than that through a conventional C-shaped aperture with the same input power. This phenomenon, the power throughput enhancement due to the coupling between propagation modes and SPP modes, is named as the hybrid effect. Moreover, the simulation results also show an ignorable variation on the spot size in near field. Therefore, we can conclude that the hybrid effect significantly increase the power throughput without degrading the spatial resolution.

### 3.3.2 Corrugations in Exit Interface

Since SPP modes on both sides of a metal film contribute to the

transmission enhancement, after investigating the effect of grooves in the entrance interface, we add a corrugation in the exit interface and study the influence of groove in the exit interface on the power throughput through the C-shaped aperture. In our optical model, the silver film thickness is 200 nm which is thick enough to suppress the tunneling effect between SPP modes on the opposite side of the metal film. Therefore, the effect of SPP modes in either interface on the transmission can be considered independently. The power throughput with various pitches, intervals, and width of the groove in the exit interface is calculated as the dimensions of the incident-side groove with the maximum PT obtained in section 3.3.1 are the optimal condition.

Because the thick film prevents the SPP modes in the entrance interface from interacting with the SPP modes at the exit face, the transmitted field through the aperture is primarily responsible for the excitation of the exit SPP modes. The propagation modes inside the aperture enhance the emitted field and thus the SPP modes in the exit interface are induced. The re-radiation and interference from the SPP modes in the exit interface contribute to the enhancement of the transmitted field out of the aperture. Therefore, the power throughput of the double-side-corrugated C-shaped aperture is as high as 8, which is further enhanced by a factor of 1.17 higher than that of the incident-side-corrugated C-aperture. Moreover, the peaks shown in Fig. 3.8 can be considered as a constructive interference of the re-radiation from the SPP modes in the exit interface while the sharp decline represents a destructive superposition of individual fields. This result indicates that the interval  $i$  is a critical factor to the field distribution.

The emitted field profile through the double-side-corrugated C-shaped aperture differs from that of the incident-side-corrugated one due to the interference of the SPP modes. This interference alters the field distribution and consequently results in the variation of the spot size. In the case of the

x-polarized incident light, the spot size in x-direction is greatly reduced over 15% while the spot size in y direction remains the same. Obviously, the groove in the exit interface functions as a focusing grating at interval  $i$  of 240 nm and then causes a more convergent emitted spot. In contrast, a narrower groove width results in a narrower potential well which makes oscillation more strongly thus causes a greater variation in field distribution of the emitted light.

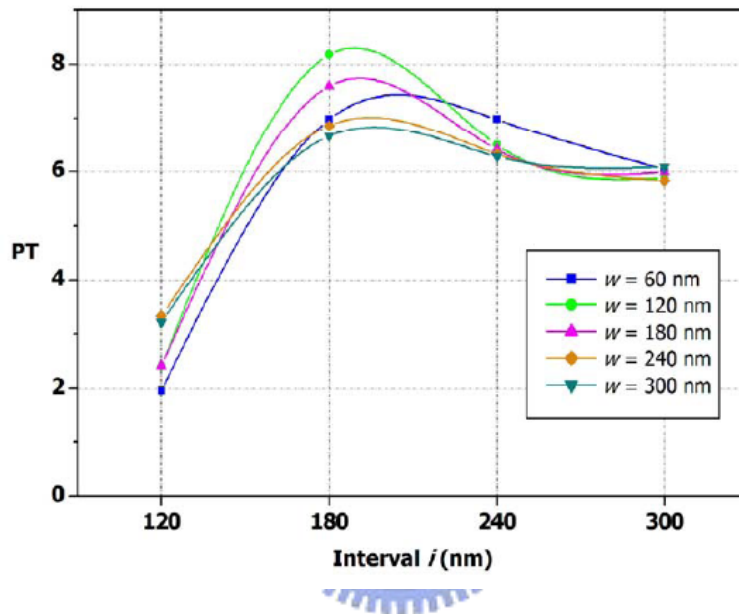


Fig. 3-8 The PT as a function of the interval  $i$  on the exit plane with various widths  $w$

The simulation results in this section demonstrate the hybrid effect induced by the coupling between the SPP modes and propagation modes inside the aperture. With a proper design of the groove surrounding the aperture on the incident plane, the incident light excites SPP modes that resonate in the interface. The interaction between the SPP modes and propagation modes results in the further power throughput enhancement. The highest power throughput occurs at interval  $i$  of 420 nm and width  $w$  of 240 nm is 6.86 at the spot size of  $118 \times 136 \text{ nm}^2$ . The groove in the exit interface functions as a grating that induces interference of SPP modes and causes a more focusing spot.

Compared to the incident-side-corrugated C-aperture, the power throughput of 8 is enhanced by a factor of 1.17; while the spot size of 102 x136 nm<sup>2</sup> is reduced by 30%.

### **3.4 Nano-waveguide with Oblique Illumination**

In the previous section, the hybrid effect is demonstrated by employing the coupling between SPP modes in the dielectric-metal interfaces and propagation modes of a C-shaped aperture. The novel design implements a C-shaped aperture in a silver film surrounded with a corrugation either in the entrance interface or on both sides of the film. Since SPP modes can also be excited in the dielectric-metal interfaces when the attenuated total reflection occurs. In this section, the hybrid effect is further studied by illuminating the C-shaped aperture with obliquely incident light. The field profiles are also simulated to investigate the mechanism of the hybrid effect.

#### **3.4.1 Effect of SPP Mode by Oblique Illumination**

According to the optical model shown in Fig. 3-1 (d), the transmission through a C-shaped aperture with oblique illumination is calculated. As the incident angle  $\Phi$  impinging on the C-shaped aperture in the metal film changed from 0 to 45 degree, the power throughput increases significantly and reaches a peak of 3.5 at 44 degree. The maximum PT is 2.3 times higher than that with normally incident light, as shown in Fig. 3-9. In the case of refractive index of the dielectric substrate of 1.475, the critical angle of the total internal reflection at the air-dielectric interface is 42.7 degree. If the dielectric substrate is covered with a metal film, the reflection coefficient of a TM wave drops suddenly to a minimum as the incident light arrive at the metal film slightly above the critical angle, which is 44.5 degree in this case. The dip in the reflectivity exhibits the

excitation of surface plasmons in the entrance interface. The coincidence between the incident angles of the minimum reflection coefficient and maximum power throughput indicates the enhancement from the hybrid effect.

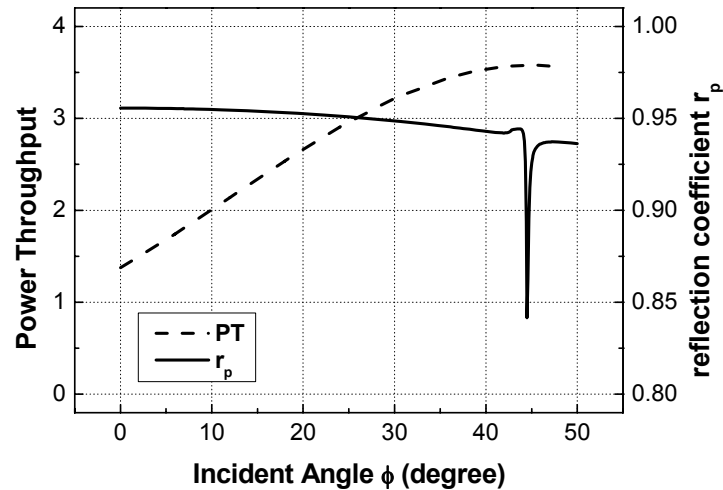
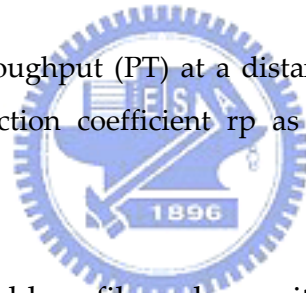


Fig. 3-9 The power throughput (PT) at a distance of 50 nm from the aperture and reflection coefficient  $r_p$  as a function of the incident angle



The calculated  $E_x$ ,  $E_z$ ,  $H_y$  field profile and magnitude of Poynting vector  $|S|$  distribution with 44-degree incident illumination also reveals the existence of the hybrid effect between propagation modes inside the aperture and SPP modes in dielectric-metal interfaces, as shown in Figs. 3-10(a) to (d). From Fig. 3-10(a), the  $E_x$  field profile shows the light propagating through the gap of the C-shaped aperture along the  $z$  direction. Compared to a conventional aperture, the C-shaped aperture remains the magnitude of the propagating wave through the aperture and thus yields a stronger emitted field at the exit of the aperture.

The  $E_z$  field perpendicular to the metal surface induces SPP modes on both sides of the metal film as shown in Fig. 3-10(b). The aperture functions as a channel to carry optical energy through the aperture. The transmitted field inside the aperture can be enhanced by SPP modes in the entrance plane and

propagates through the aperture in terms of propagation modes. Therefore, the enhanced field excites SPP modes in the exit plane and the re-radiation from the SPP modes further increase the transmitted field out of the aperture. This also explains SPP resonances on both sides of the metal film under oblique illumination. The corresponding surface plasmon wave vector  $k_x$  which lies parallel to the surface can be described as

$$k_x = k_0 \left( \frac{\varepsilon_m \cdot \varepsilon_d}{\varepsilon_m + \varepsilon_d} \right)^{1/2} \quad (3-1)$$

where  $\varepsilon_m$  is dielectric constant of the metal film,  $\varepsilon_d$  is that of the dielectric material, and  $k_0$  is the wave vector of incident light. Then the surface plasmon wavelength  $\lambda_{SP}$  along the  $x$  direction can be obtained by

$$\lambda_{SP} = \frac{2\pi}{k_x} \quad (3-2)$$

According to Eq. (3-2), the corresponding surface plasmon wavelength at the dielectric-metal interface,  $\lambda_{sp,d-m}$ , is 0.39  $\mu\text{m}$  and that at the air-metal interface,  $\lambda_{sp,a-m}$ , is 0.61  $\mu\text{m}$ . From the field profile in Fig. 3-10 (b), the estimated surface plasmon wavelengths at those two interfaces are 0.4  $\mu\text{m}$  and 0.6  $\mu\text{m}$ , respectively. The good agreement between the theoretic calculation and the FDTD simulation results, as listed in Table 3-2, reveals that SPP modes do exist on both sides of the metal film even through the film thickness is up to 200 nm.

The magnitude of Poynting vector  $|S|$  represents the energy flow in both  $\pm x$  direction and  $+z$  direction. The calculation shows that the incident energy is coupled into SPP modes in the entrance plane and propagation modes through the waveguide. The SPP modes contribute to the enhancement of the propagation field and the propagation modes carry the optical energy through the aperture. As a result, the transmission through the aperture is significantly enhanced by the hybrid effect that SPP modes and propagation modes coexist.

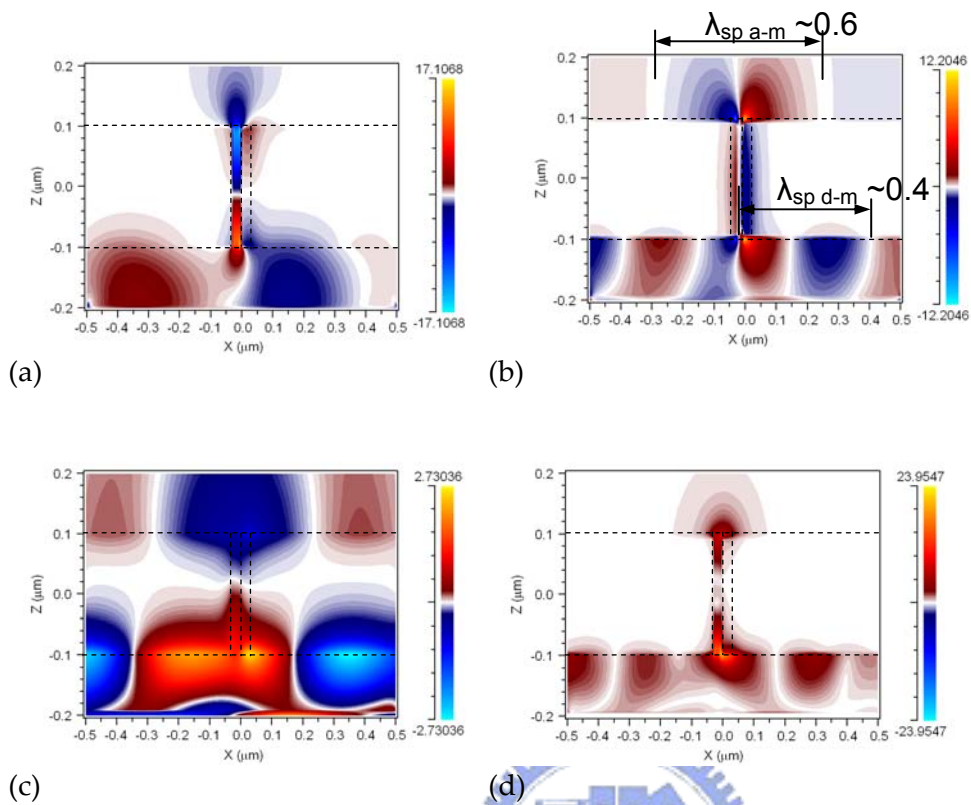


Fig. 3-10 (a)  $E_z$ , (b)  $E_x$ , and (c)  $H_y$  field profile, and (d) magnitude of Poynting vector plot when the incident angle is 44 degree. The dashed line showed the contour of the metal film and the C-aperture

Table 3-2 Comparison of SPP wavelength by using SPP theory and FDTD method

(unit: $\mu\text{m}$ )	SPP wavelength at dielectric-metal interface	SPP wavelength at air-metal interface
SPP theory	0.39	0.61
FDTD method	0.40	0.60

To further investigate the hybrid effect, the spectral response of the power throughput through the C-shaped aperture with 44-degree illumination in the



visible light region is also calculated, as presented in Fig. 3-11. The peak at the incident wavelength of 633 nm in the spectrum indicates that the power throughput enhancement results from the excitation of the SPP modes which constructively couples with the propagation wave supported inside the waveguide.

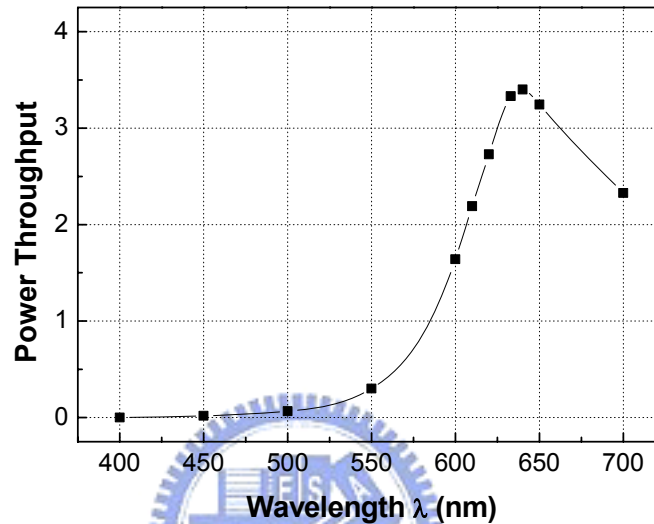


Fig. 3-11 The spectral response of the power throughput through the C-shaped aperture with a incident angle of 44 degree

### 3.4.2 Effect of Propagation Mode of Aperture

The calculated electric intensity distribution inside the C-shaped aperture confirms the existence of propagation modes along the aperture. Figs. 3-12(a), (b), and (c) represent the electric intensity distribution at a position of 1/4, 1/2, and 3/4 of the aperture depth from the entrance plane, respectively. The mode field distribution remains the same when the light propagates through the aperture. The electric field is mostly confined in the concave gap area and there is only slight penetration into the metallic ridge part. Therefore, the gap dominates the supported propagation mode and the transmission through the waveguide. Instead, the spot size of the propagating field is determined by the

ridge dimensions. This result also confirms the analysis of the transmission characteristic in section 3.1. Moreover, the propagation mode also contributes to the transmitted power propagation out of the aperture. The power throughput as a function of the distance from the aperture plotted in Fig. 3-4(d) exhibits a gradual decay with the increase of the distance and can be kept over 1 within a spacing of 300 nm.

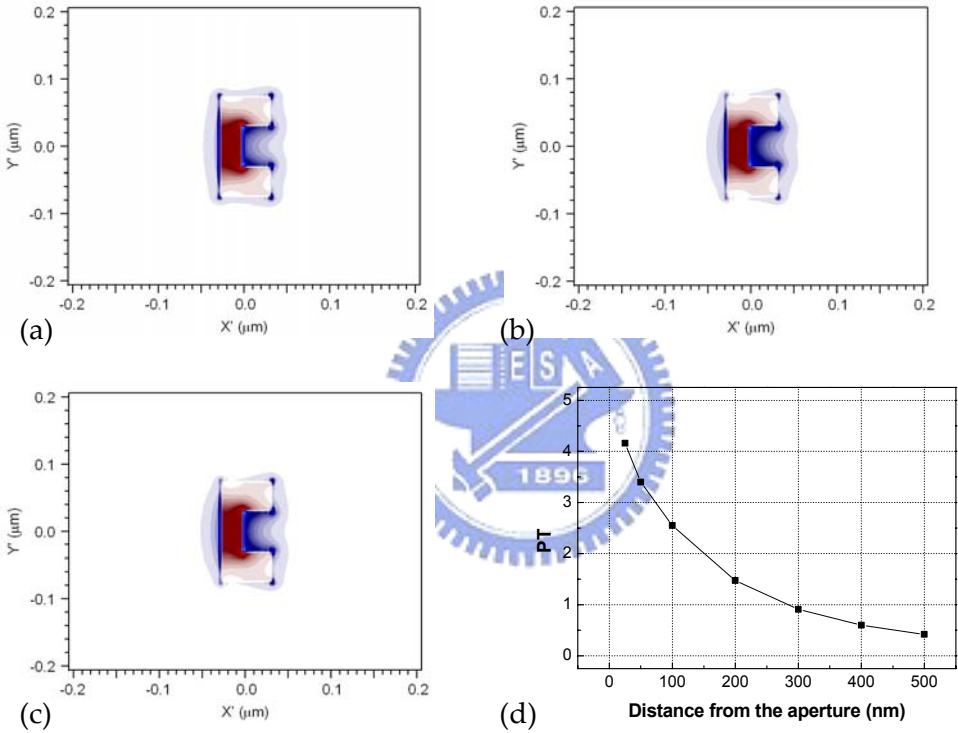


Fig. 3-12 Electric intensity distribution inside the waveguide at a position of (a) 1/4, (b) 1/2, (c) 3/4 of the length from the entrance plane when propagating along the waveguide, and (d) the power throughput decay as a function of the distance from the waveguide

The enhancement and the power throughput through the C-shaped aperture under oblique illumination are only half of that in the corrugation case with normally incident light. The mechanism is investigated and analyzed by

observing the power throughput through the C-shaped aperture illuminated with a fixed 44-degree incident angle but with various aperture dimensions. If we define a scale factor as the ratio of the modified dimension of the C-aperture to the original one, the power throughput as a function of the scale factor can be obtained, as plotted in Fig. 3-13.

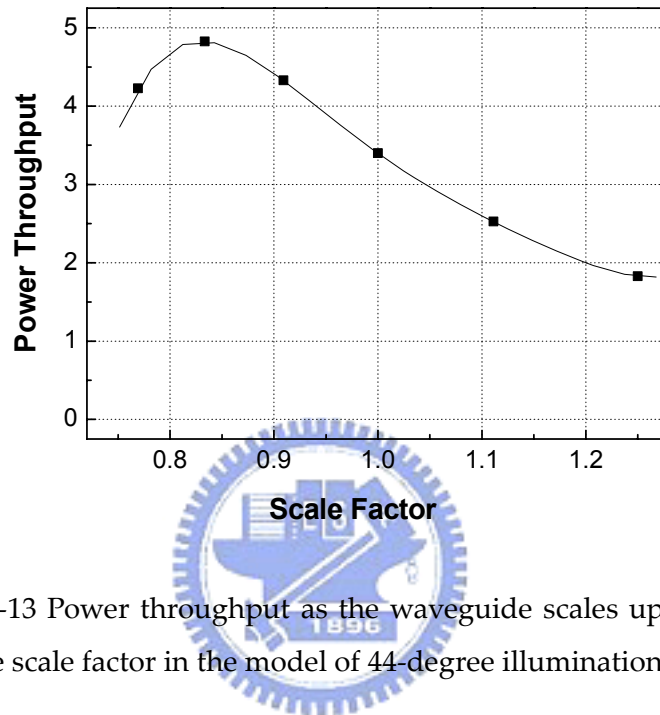


Fig. 3-13 Power throughput as the waveguide scales up or down by the scale factor in the model of 44-degree illumination

The simulation results clearly show the power throughput reaches a peak of 4.8 as the dimensions shrank by a factor of 0.83 but drops to 1.8 as the dimensions scale up by 1.25. Compared to the original design which is optimized under the condition of normal incidence, the dimensionally scale-down design further increases the power throughput by a factor of 1.42. According to waveguide theory, the dimensions of a waveguide determine the propagation modes that can be supported and the energy that can be carried through the waveguide. On the other hand, the incident angle of the beam into the waveguide dominates the coupling efficiency between the incident light and the propagation mode in the waveguide. Consequently, in the original design, the benefit from the hybrid effect is offset by a reduction in the coupling

efficiency into the propagation mode under oblique illumination. In contrast, dimensionally down-scaling alters the supported mode within the waveguide and thus enhances the power throughput at the corresponding cut-off wavelength.

### 3.5 Summary

The hybrid effect induced by coupling between SPP modes in the dielectric-metal interfaces and propagation modes of a C-shaped aperture is numerically demonstrated and thus enhances the transmission through the aperture. By employing a C-shaped aperture surrounded with a circular corrugation or illuminated with obliquely incident light, SPP modes in the dielectric-metal interfaces are excited and enhance the propagation modes inside the aperture and the emitted field out of the aperture. Compared to a single C-shaped aperture without the hybrid effect induced, the power throughput can be further enhanced by a factor of 2.4 to 4.0 by the hybrid effect, as summarized in Table 3-3.

Table 3-3 The calculated power throughput and enhancement of a single C-shaped aperture, a C-shaped aperture with corrugations, and a C-shaped aperture with oblique illumination

	Single C-aperture	C-aperture with Corrugations		C-aperture with 44° Incidence	
		Entrance Plane	Double Sides	Original Dimension	Scaled down
<b>Power Throughput</b>	<b>2.0</b>	<b>7.0</b>	<b>8.0</b>	<b>3.5</b>	<b>4.8</b>
<b>Enhancement (to C-aperture)</b>		<b>3.50</b>	<b>4.00</b>	<b>1.75</b>	<b>2.40</b>

# Chapter 4 Experiment in Enhanced Transmission of Hybrid Effect

To verify the optical model and the simulation results presented in Chapter 3, experiments in the transmission through the hybrid-effect apertures are conducted. Prior to the experiments, major technologies implemented for device fabrication and the challenging issues encountered are explained and discussed. The experimental instruments used for measurement are also introduced in details. The experimental results, including far-field power throughput and near-field intensity distribution, demonstrate the power throughput enhancement induced by the hybrid effect employing either a corrugation or oblique illumination.

## 4.1 Fabrication of Subwavelength Aperture

Subwavelength apertures are fabricated in a metal film with or without the support of a substrate behind the film. Therefore, the fabrication process of metal film preparation is given in the first section and followed by the method of perforating the metal film, the focused ion beam milling.

### 4.1.1 Preparation of Metal Film

To make a free-standing metal film, the first step is to deposit a silicon nitride membrane on both sides of a silicon wafer as etching-stop layers using low pressure chemical vapor deposition (LPCVD). The bottom side of the silicon wafer is patterned to define openings for etching. The silicon nitride layer inside the openings then is removed by using reactive ion etching. Due to the anisotropic properties of silicon, a bulk micromachining process, selectively

wet etching, uses potassium hydroxide (KOH) to dissolve silicon substrate from the bottom side until the etching-stop layer and produces a huge blind hole with a flat bottom and angled side walls. A metal film is deposited on the top surface of the silicon nitride membrane by sputtering. Finally, a free-standing metal film is generated by removing the silicon nitride layer using inductively coupled plasma reactive ion etching (ICP-RIE). The fabrication process is illustrated in Fig. 4-1.

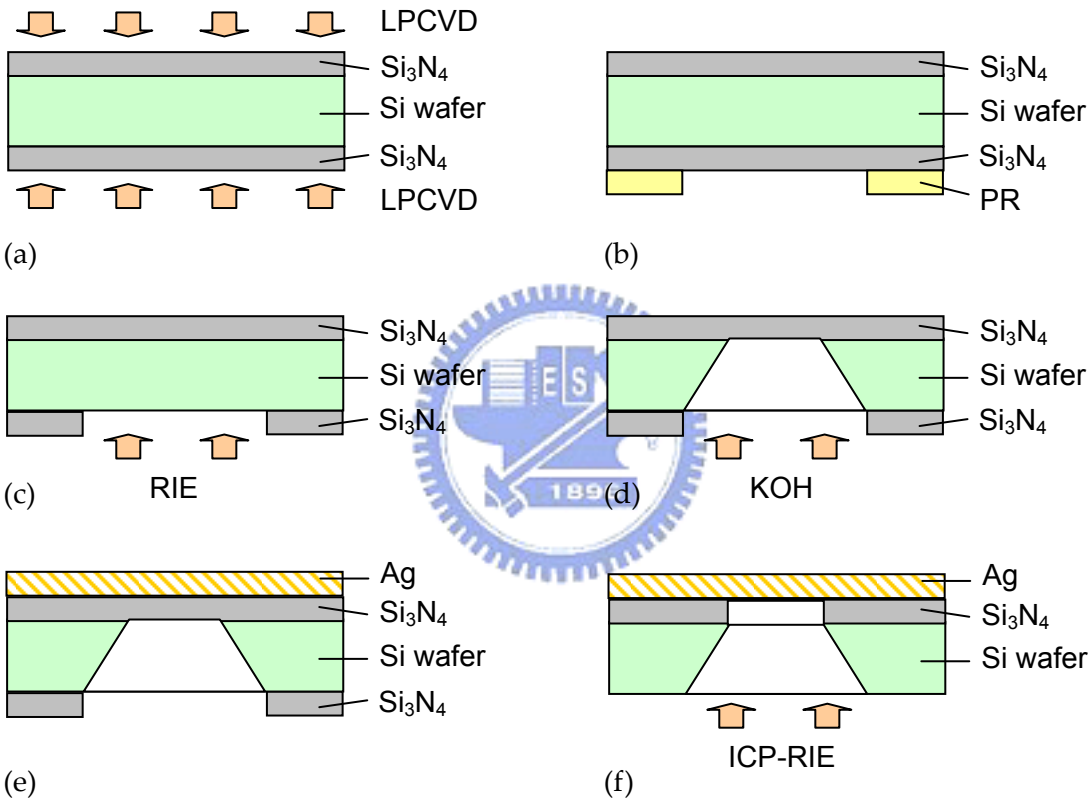


Fig. 4-1 Fabrication process of a free-standing metal film (a) deposit silicon nitride on silicon wafer, (b) pattern on photo resist, (c) remove silicon nitride by RIE, (d) wet etch using KOH, (e) deposit silver film, and (f) remove silicon nitride by ICP-RIE

Compared to the free-standing membrane fabrication process, the preparation of a metal film with the support of a substrate is much simpler. A dielectric substrate, like a glass substrate or an optical fiber, is cleaned

thoroughly with the aid of solvents and DI water. Then a metal film is deposited on the top surface of the substrate by sputtering. However, in the case of an optical fiber, since the metal film has to cover the end face of the fiber, a special fixture must be used to ensure unchanged orientation of the end face during the whole process.

#### **4.1.2 Focused Ion Beam Milling**

Considering the line width of subwavelength apertures is around 100 nm with an aspect ratio greater than 2, we choose the focused ion beam milling method (FIB) to perforate the metallic film. Ions are charged particles so they can be accelerated and redirected by an external magnetic field. It means the ion beam can be focused to a tiny spot like a light beam. A focused ion beam system usually utilizes a gallium ion source ( $\text{Ga}^+$ ) to generate ion “bullets” for bombarding target surfaces. With sufficient energy, the collision between the ion bullets and the atoms in the target surface causes the spreading out of numerous particles, including ions, atoms and electrons. Moreover, due to the secondary electrons generated during the etching process, a SEM-like image of the scanning area can also be obtained simultaneously. If the removing process repeats continuously, the material is taken away layer by layer sequentially and then a hole can be formed. The removing speed, usually called the etching rate, is dependent on the target material and the energy of the ion beam which is determined by the current density.

A special feature of holes fabricated by FIB is unavoidably tapered with round corners because of the nature of the focused beam and imperfect energy distribution in the peripheral area of the beam. It means the side wall is neither straight nor parallel to the direction of the beam axis. Practically, the line width is defined as the distance of two side walls at half of height of the hole. The

minimum achievable line width highly depends on the current density, the material, the aspect ratio, and the spot size which is determined by the aperture size of a mask used before the beam is focused. The ion beam with high current density, i.e. high energy, will sputter out larger particles. Similarly, the material itself also determines sizes of particles. A larger particle size implies higher removing speed but also worse resolution that can be controlled. Since the ion beam is naturally tapered, the higher the aspect ratio is, the larger the dimensional difference between the top and the bottom of the hole is. In addition, since the dimensions are all in a nanometer scale, any vibration will cause significant misalignment of the focused beam on target areas and degradation of dimensional errors. This explains why the theoretic minimum spot size of conventional FIB systems can be as small as 5 nm but the achievable line width is much larger than 5 nm. The minimum line width that we achieved is 50 nm in a 200-nm silver film under the condition of a 25- $\mu\text{m}$  mask aperture with a current of 5 pA.

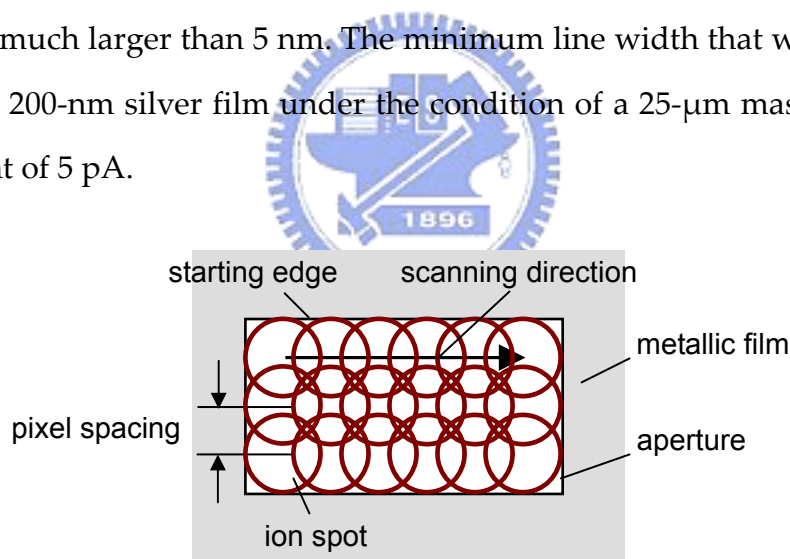


Fig. 4-2 Parameters determining the quality of a special-shaped aperture

Compared to a simple and symmetrical cross-section, such as a circle, an aperture with a special shape, especially those with straight edges and sharp corners like a C shape, is much more complicated and difficult to fabricate. Take a C shape as an example, the most challenging issue is how to maintain the



straightness of the edges and the sharpness of the corners. In the case of the aperture dimensions larger than the beam size, the ion beam will scan over the sample surface pixel by pixel discretely along a specific path to produce the designed shape. It means any shape is formed by a matrix of ion pixels, as illustrated in Fig. 4-2. Therefore, three dominant factors determine the quality of the special-shaped aperture: the scanning itinerary, the scanning direction, and the pixel spacing.

The scanning itinerary means the sequence of ion pixels on the scanning area. Typically, it is classified in two ways, a raster or a single pass. A raster means a scan starts from the first pixel, stays there for a short time, moves to an adjacent pixel and keeps moving until the entire area is scanned completely. After one scan completes, the whole process repeats until reaching the target dose. In contrast, for a single pass, the ion beam stays in the same pixel until the required dose is done and then repeats this step in an adjacent pixel. Limited by the position precision of the spot at every scan, a single pass is usually better for nano-aperture fabrication.

The scanning direction of the ion beam relative to the orientation of the aperture influences the roughness of surfaces and edges of the side wall. If the scanning direction is aligned to a starting edge, the edge will have the best surface quality, i.e. the smoothest surface, compared to that of edges perpendicular to the scanning direction. Because the gap width of a C-shaped aperture and the two sides that form the gap are the most important parameters to determine the transmission property, the ion beam must be aligned to the aperture length to obtain a well-defined aperture.

The pixel spacing means a center-to-center distance between two adjacent pixels. In a conventional FIB system, the pixel spacing along X and Y axis can be set independently. Due to a similar scale between apertures sizes and ion spot

sizes, the pixel spacing will determine the surface roughness and the actual width of the aperture. However, since ion bombardments on target material also result in spreading out of particles, some particles will be re-deposited outside the exposure area. Too dense pixel density, i.e. narrower pixel spacing, might cause redistribution of material and consequently structure distortion.

The FIBs utilized for our experiments are FEI Nova 200 at Instrument Technology Research Center (ITRC) in Taiwan and Micrion 2500 at Carnegie Mellon University (CMU) in the US, respectively. Both are dual-beam systems that can do ion etching and SEM imaging. The minimum achievable ion spot is 5 nm theoretically.

## **4.2 Measurement Instrument**

To measure the transmission properties of nano-apertures, two instruments are implemented. A transmission-mode near-field scanning optical microscope (NSOM) is used to obtain the near-field intensity distribution from apertures. A far-field optical system is also set up to measure the transmission through apertures. Comparison of the intensity distribution and the transmission among different apertures can not only demonstrate the characteristics of the proposed design and theory but also provide more information to analyze mechanisms behind the phenomena.

### **4.2.1 Near-field Scanning Optical Microscope**

To resolve an image of an object, optical components are necessary to collect the field of each image point which carries spatial frequency information. However, because the propagating light diffracts into the far field and the aperture of the component is not infinitely large enough to collect all the diffraction light, the resolving capability of an optical component is limited.

Evanescent or non-propagating waves that exist only near the object carry more high-frequency information of the object but have intensities that decay exponentially with distance from the object. Therefore, the spatial resolution beyond the diffraction limit can be obtained if a detector is placed close to the object to detect and make use of evanescent waves with high-frequency information. This theory gives birth to near-field scanning optical microscopes (NSOM).

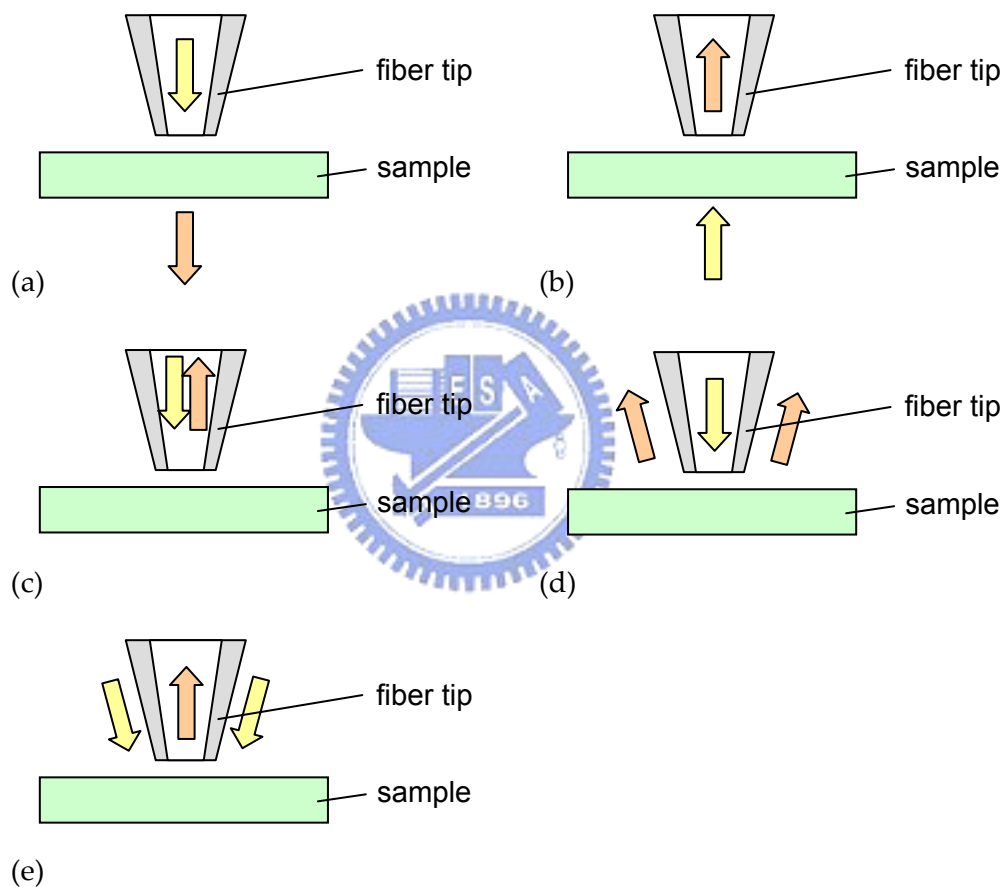


Fig. 4-3 Operation modes of an apertured NSOM (a) illumination, (b) collection, (c) illumination collection, (d) reflection, and (e) reflection collection

NSOM can be classified into two types, apertured or apertureless type. An apertured NSOM utilizes a tapered and metal-coated fiber probe with an aperture having a diameter less than a wavelength on the tip. The fiber tip

functions as a near-field light source to illuminate the sample or a near-field detector to collect and transfer evanescent fields into detectable signals in far field. Since the aperture has a finite size, the signal actually is the convolution of the field of the object and the aperture. An apertureless NSOM uses a metallic tip to scatter high-frequency evanescent fields to be converted into low-frequency propagating fields that can be detected by a far-field detector. The far-field signals are modulated by perturbations in near field. For an apertured NSOM, there are five primary operation modes, illumination, collection, illumination collection, reflection, and reflection collection, as shown in Fig. . The first two are transmission modes while the remaining three are reflection modes. Therefore, the choice of operation modes depends on sample characteristics, e.g. opaque or transparent, and total amount of light on the sample.

The essential factor to ensure the success of NSOM is the scanning system that drives a fiber tip to fly over sample surfaces at a height of a few nanometers above the surface. Two basic functions are required: capability of precise positioning on the sample surface and accurate servo control for maintaining a constant gap between the tip and the sample surface. A common way to maintain the gap is the shear force feedback method. A fiber probe is attached to one arm of a quartz crystal tuning fork and the other arm of the tuning fork is attached to a piezo-ceramics oscillator which can oscillate the tuning fork at its resonant frequency. Because of the piezoelectric effect of the tuning fork, i.e. an electrical field generated under pressure and conversely dimensions changed when an electrical field is applied, the oscillation induces an AC signal which can be monitored. When the fiber tip is approaching to the sample surface, the shear force between the tip and the surface damps the oscillation and causes a change in the induced signal amplitude. The dependence of the amplitude change on the distance then is used as a feedback servo signal to maintain the

gap. Full-range moving and positioning of the scanning head consisting of the fiber probe, the tuning fork, and the piezo oscillator are accomplished by employing a 3-axis piezoelectric tube.

The extremely low transmission through the aperture of the fiber probe results in a low signal-to-noise ratio. Thus, the illuminating light on the sample is modulated by a chopper at a fixed frequency and the optical signal detected by a photomultiplier tube (PMT) is amplified by a lock-in amplifier at the same frequency to filter out background noise. Moreover, compared to the image obtained at once from conventional far-field microscopes, the data from NSOM is built point by point. It means that only local image information is taken in a small step and the measured signal is an integral of the collected signal for a finite time period. Therefore, we can only obtain a relative near-field intensity distribution rather than an image of an absolute illumination distribution from NSOM. Furthermore, the topography also induces a significant influence on optical images because the probe cannot completely follow the contour of sample surfaces and a nonlinear effect of the boundary conditions occurs as the topography changes. It implies that the near-field intensity distribution from NSOM is not exactly the same as the real distribution of the sample. Consequently, optical and topographic images must be correlated to prevent misconstruing the data.

The NSOM used in our measurement belongs to Nano-Photonics Laboratory at Research Center for Applied Science, Academia Sinica. The measurement is conducted in collection mode. The membrane perforated with apertures is installed on a 3-axis stage and illuminated by a focused beam with a wavelength of 633 nm. The fiber tip scans over the surface of the sample to obtain the near-field intensity distribution through the subwavelength aperture in the metal film.

## 4.2.2 Far-field Transmission Measurement System

A measurement system is designed and carried out to measure the far-field power throughput. The system configuration is illustrated in Fig. 4-4. A linearly polarized laser beam with a wavelength of 633 nm is focused on apertures by an objective lens. The substrate that supports the apertures is attached to a holder on a 3-axis stage so that the apertures can be finely positioned to the focused beam. A collimating lens behind the aperture is utilized to collect and collimate the transmitted light. In the optical path lies a CCD camera to capture optical images through apertures, or an optical power sensor to measure the transmitted power. In the case of oblique illumination measurement, the laser diode and the objective lens are installed on a rotation stage that can rotate with respect to the aperture.

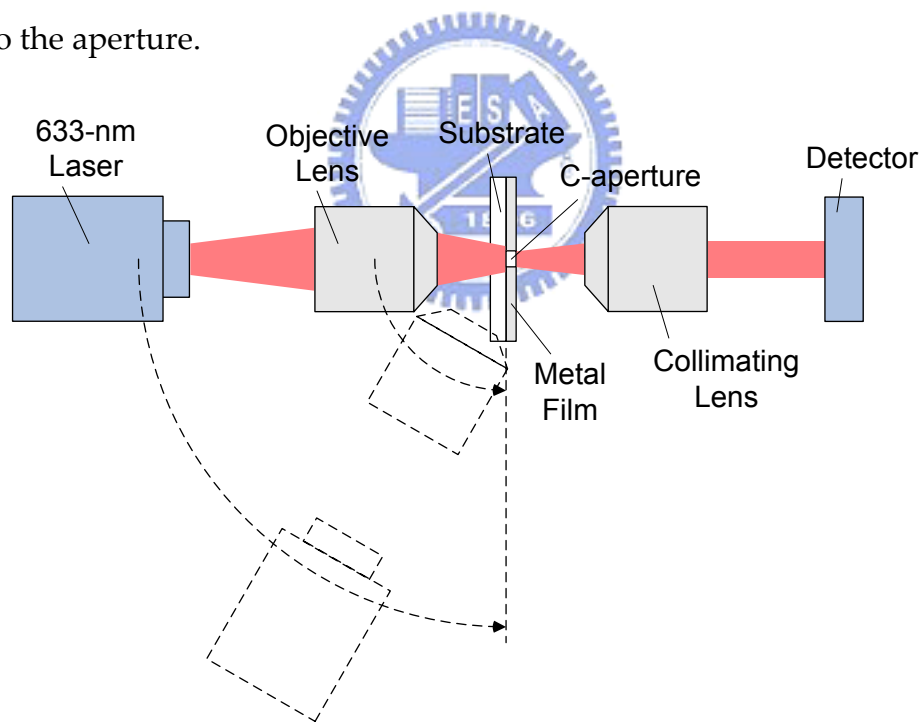


Fig. 4-4 Configuration of far-field measurement system

To align the aperture to the focal point of the incident beam, a microscope is necessary to zoom in the illuminated area of the substrate. With the aid of alignment keys around the aperture on the substrate, the position of the focused

spot can be ensured to be on the aperture area. However, the aperture is too small to be seen under a microscope so that we are not sure whether the aperture is exactly in the optical axis and the focal plane of the incident beam. The real-time images captured by the CCD camera provide sufficient information to finely tune the position. With respect to the center of the aperture, the misalignment of the incident beam causes a symmetric change in the image pattern. It means that there are two mirror images in opposite positions relative to the center of the aperture. Consequently, by moving the aperture back and forth until two mirror images occur, the middle position of two mirror images will be the target central position.

A laser beam at the focal plane is supposed to have a Gaussian distribution. However, within the effective area around the aperture, the incident field is assumed to be a plane wave because the focused spot size is much larger than the dimensions of the aperture. In addition, the ratio of the measured transmitted power to the total incident power represents the overall power transmission. To coincide with the power throughput used in the simulation, the central peak of the Gaussian beam is assumed as the incident amplitude at the aperture. The transmitted power is measured and then the power throughput is calculated and compared to the simulation results accordingly.

### **4.3 Experimental Results**

Both far-field transmission and near-field intensity distribution through a corrugated C-shaped aperture and a C-shaped aperture with oblique illumination are measured by means of the instruments mentioned in the previous section. The experimental results demonstrating the transmission enhancement by the hybrid effect are presented and discussed in this section.

### 4.3.1 Preparation of Aperture

To evaluate the power throughput enhancement induced by the hybrid effect, two groups of apertures with specific geometry and dimensions are fabricated in a silver film by focused ion beam milling method (FIB). As shown in Fig. 4-5 (a), (b), and (c), the first group consists of a circular aperture, a C-shaped aperture, and a C-shaped aperture surrounded by a groove in a 200-nm free-standing silver film. It is for the study of the hybrid effect induced by a corrugation structure. The second group is a single C-shaped aperture to demonstrate the enhancement resulted from the hybrid effect induced by oblique illumination on a nano-waveguide. In this group, a 200-nm silver film is coated with a glass substrate with a refractive index of 1.475 and perforated with a C-aperture, as shown in Fig. 4-6.

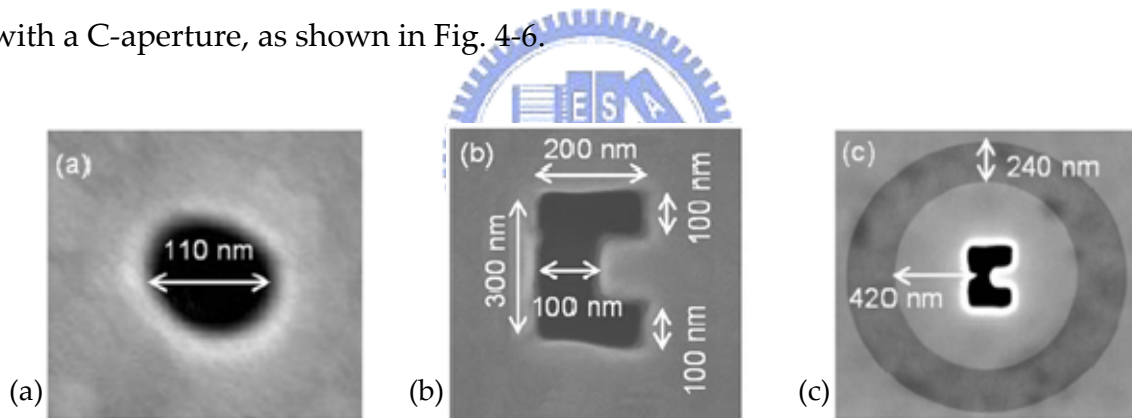


Fig. 4-5 SEM photos of (a) a circular aperture, (b) a C-shaped aperture, and (c) a C-shaped aperture surrounded by a groove

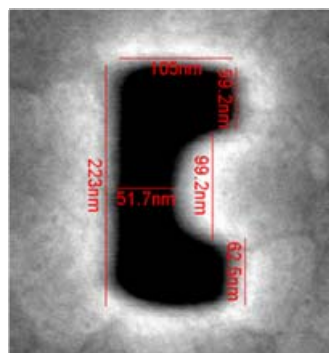


Fig. 4-6 SEM photo of a single C-shaped aperture for oblique illumination



Because the line width resolution of FIB is around 100 nm and there are repeatability issues, the dimensions of the apertures fabricated for the experiments are not the same as that of the optimal design in the simulation. The minimum diameter of the circular aperture is 110 nm. The outer dimensions of the C-shaped apertures for corrugation study are 300 nm x 200 nm with a line width of 100 nm while that for oblique illumination experiment are 220 nm x 105 nm. In contrast, the designed groove width of 240 nm is able to be achieved since it is larger than the minimum line width of 100 nm.

### **4.3.2 Far-field Power Throughput**

The measurement results in the following tables demonstrate the hybrid effect predicated by our proposed model and reveal the enhancement resulting from this novel effect. Table 4-1 exhibits the existence of the propagation mode in the far-field enhancement of 17.8. Moreover, the incident-side-corrugated C-aperture yields enhancement of 33 in transmittance. Compared to a single C-aperture, the hybrid effect can further enhance the PT by a factor of 1.9. The result also indicates that the SPP field can couple to the propagation mode of the C-aperture and propagate to the far-field region. The hybrid effect consisting of propagation modes along the waveguide and surface plasmon wave at the exit plane of the waveguide reduces the energy decay from the exit of the waveguide and thus makes the far-field power throughput detectable.

The measurement of the far-field power throughput through a C-aperture with different illumination angles also obeys our simulation model, as shown in Table 4-2. The far-field power throughput with normal incidence is 0.25 while that with 44-degree incidence is 0.33. The hybrid effect induced by a C-aperture with oblique illumination yielded an enhancement factor of 1.3.

Compared to the results in the previous chapter, the measured PT and

corresponding enhancement are not as high as that in our simulation. The most critical factor obviously is the dimensional difference between the optimal design and the fabricated ones. In addition, since the transmitted intensity through the circular aperture is considerably low, the detected power is easily disturbed by the light leakage from the ambience. Furthermore, the simulated enhancements are calculated in the near-field region, 50 nm from the aperture; while this measurement is taken in the far-field region, usually several centimeters from the aperture. Consequently, the dissipation of transmitted energy through the C-aperture reduces the measured enhancement. Although the measured enhancement is not as large as the designed one due to fabrication limitation, the experimental result successfully demonstrates the hybrid effect we discovered in simulation.

Table 4-1 Far-field transmission of a circular aperture, a C-aperture, and a C-aperture with a corrugation and calculated power throughput enhancement induced by the hybrid effect

Sample	Circular	C-aperture	C-aperture with corrugation
Transmission (%)	0.01	0.83	1.54
Power Throughput	9.33E-03	0.17	0.31
Measured Enhancement (Far-field, to the circular)		17.8	33.0
Measured Enhancement (Far-field, to the C-aperture)			1.9

Table 4-2 Far-field transmission of a circular aperture, a C-aperture with two different illuminating angles and calculated power throughput enhancement induced by the hybrid effect

Sample	Circular	C-aperture (0 degree)	C-aperture (44 degree)
Transmission (%)	0.01	1.34	1.79
Power Throughput	9.33E-03	0.25	0.33
Measured Enhancement (Far-field, to circular)		26.8	35.4
Measured Enhancement (Far-field, to 0 degree)			1.3

### 4.3.3 Near-field Intensity Distribution

The near-field intensity distribution was picked up by means of a near-field scanning optical microscope. The convolution of the near-field intensity with the aperture of the fiber tip is converted to an optical signal detected by a photo-multiplier tube (PMT) and amplified by a lock-in amplifier. Therefore, the magnitude of measured signal represents the relative intensity in the near field. In addition, because the transmitted energy through the circular aperture is too weak to be recognized from the background noise, the optical image of the circular aperture is null.

The optical signal of the single C-aperture, shown in Fig. 4-7 (a), reaches 2.5V, indicating a signal-noise-ratio of 40 dB compared to background noise of 0.02V. Moreover, the peak intensity of the C-aperture surrounded with a corrugation is up to 7V, which is 2.8 times higher than that of the single C-aperture. The experimental result under oblique illumination also confirms the enhancement. Figs. 4-8(a) and (b) show the near-field distribution with normal and 44-degree incidence. By comparing the signal voltage of 1.1V in the normal-incidence model to that of 1.8V model under 40-degree incidence, the near-field enhancement factor can be as high as 1.6.

Due to finite spatial resolution of NSOM, the measured spot size is unavoidably larger than the actual size. In the case of the aperture size of the fiber probe used in this experiment ranging from 50 to 100 nm and the theoretic spot size of this fabricated C-aperture of 150 nm x 150 nm, the measured spot as a result of convolution is estimated around 300~400 nm, which is in agreement with the measured result.

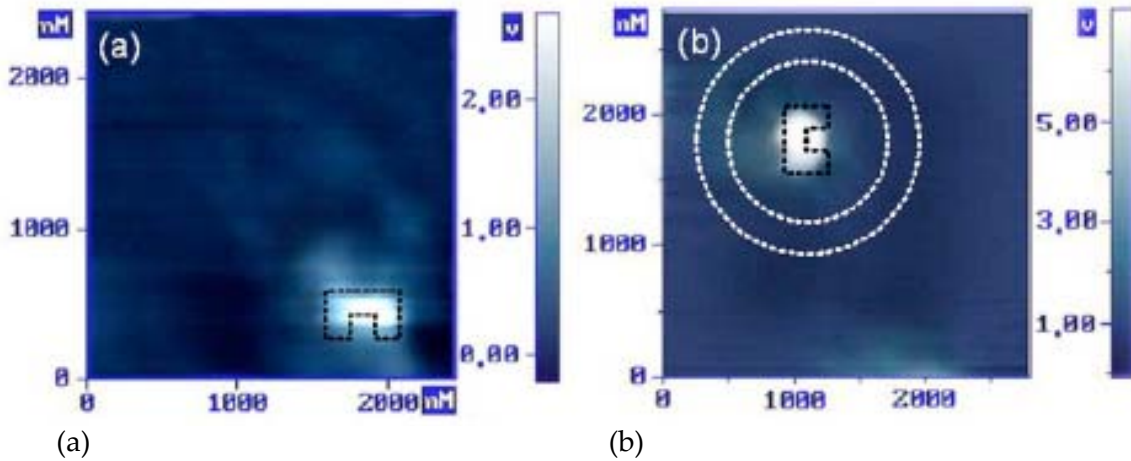


Fig. 4-7 Intensity distributions measured by NSOM (a) background noise and (b) the C-shaped aperture

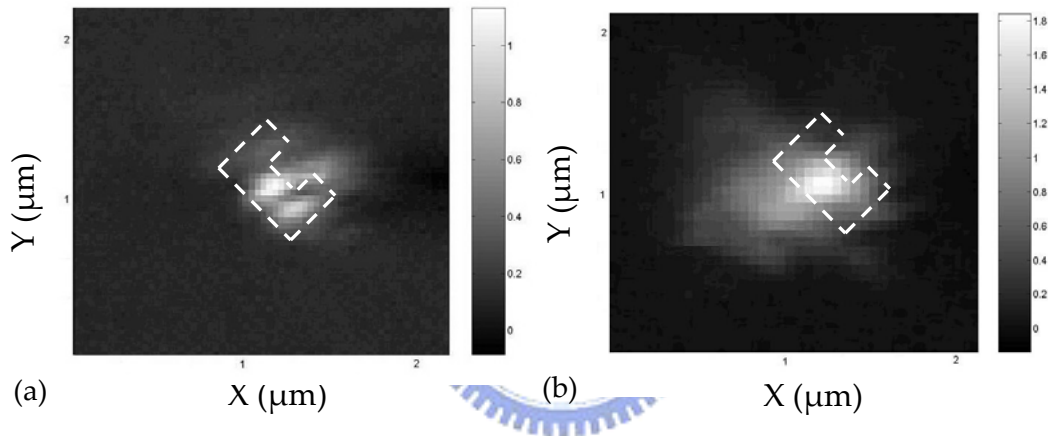


Fig. 4-8 Near-field distribution observed by NSOM with (a) normal and (b) 44-degree incidence

To further examine the consistence of the experimental results with simulation, the power throughput and intensity distribution at 50 nm from the C-aperture, of which the dimensions are the same as that of the fabricated one, are calculated with normal and 44-degree incident illumination, respectively. The simulation results are shown in Fig. 4-9. The output spot with 44-degree incidence has a smaller size with higher peak intensity than that with normal incidence. The calculated power throughput enhancement as a result of the hybrid effect is 2.2. Moreover, the calculated  $E_x$  and  $E_z$  field profile under 44-degree illumination also shows the hybrid effect in Fig. 4-10, even though the

dimensions of the fabricated waveguide were larger than the designed one. The incident light propagates through the waveguide with the aid of the surface plasmon wave propagating along the dielectric-metal surface. Therefore, although the measured enhancement is not as high as the simulated one of 2.2, the results demonstrates that the hybrid effect contributes to the enhancement of the transmitted power propagated along the C-shaped aperture which functions as a ridge waveguide.

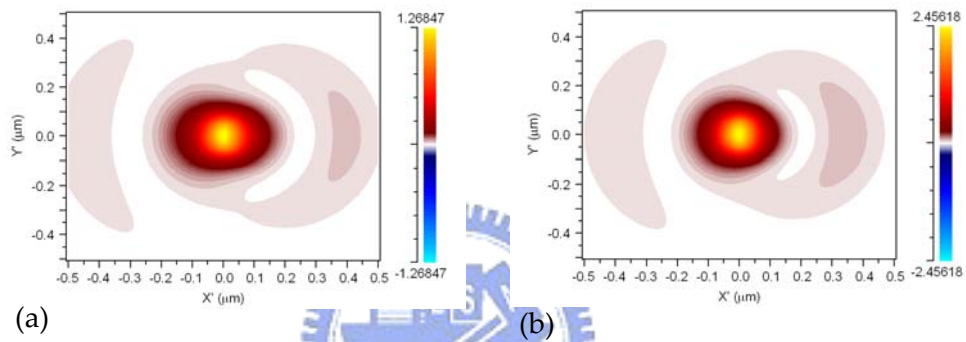


Fig. 4-9 Calculated electric intensity distribution at 50nm from the nano-waveguide with the experimental dimensions at (a) normal incidence and (b) 44-degree incidence

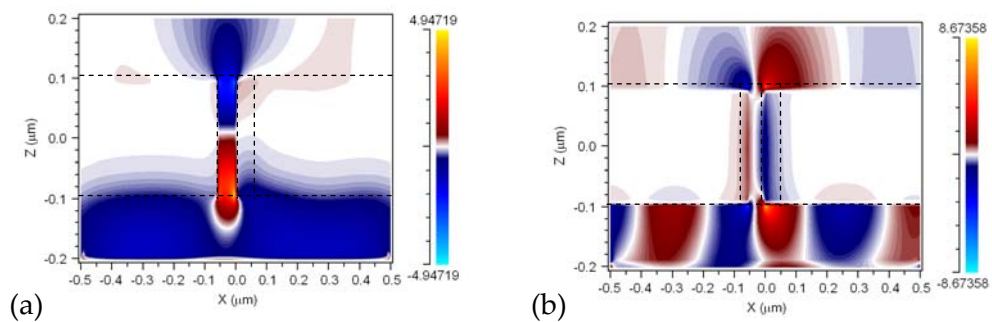


Fig. 4-10 Calculated (a)  $E_x$  and (b)  $E_z$  field profile with the experimental dimensions

## 4.4 Summary

The experimental results successfully confirm the existence of the hybrid effect. The far-field transmission of a waveguide with corrugation in incident interface is 1.9 times higher than a single C-shaped aperture and 33 times higher than a circular aperture with a similar spot size. In the case of the aperture with oblique illumination, the far-field transmission measurement demonstrates an enhancement factor of 1.3, while the near-field intensity distribution measurement shows that the enhancement can be as high as 1.6. The measurement results are summarized in Table 4-3. These results give the birth of our proposed straw-shaped fiber probe employing the hybrid effect induced by illuminating the waveguide with obliquely incident light.

Table 4-3 Comparison between the measured power throughput enhancement of a C-shaped aperture with corrugations and a C-shaped aperture with 44-degree illumination

<b>Enhancement (to C-aperture)</b>	<b>C-aperture with Corrugation</b>	<b>C-aperture with 44° Illumination</b>
<b>Far-field PT</b>	<b>1.9</b>	<b>1.3</b>
<b>Near-field intensity</b>	<b>2.8</b>	<b>1.6</b>

# Chapter 5 Near-field Servo Control System Employing Self-mixing Sensor

For a near-field storage system, the optical head has to be put in proximity to the surface of the recording medium because the optical energy decays exponentially with an increase of the distance from the head. Conventional near-field servo control requires a complicated system to process signals. Therefore, we proposed a novel servo control system by employing a self-mixing laser sensor. The dependence of the laser output on the spacing between the laser and the target makes the laser itself function as a sensor and thus self-mixing interferometers can reduce the system complexity [40-42]. Furthermore, the use of a laser diode has an advantage of compact package because the modulation in the emitted power can be detected directly by the photodiode inside the laser diode package. Therefore, laser diodes can be used as a compact optical sensor and easily integrated into other systems.

In this chapter, the proposed near-field servo control system employing a self-mixing laser sensor is developed. To characterize the self-mixing signal, a simplified coupling formula is derived and compared to the measured signal of a laser sensor which is obtained by modifying a conventional laser diode. A biaxial actuator is used to drive the laser sensor. The approach limit of this system, the theoretic minimum spacing that a laser sensor can achieve, is also estimated base on the alignment precision and measured angular variation of a spinning disk. According to the measured dynamic response of the actuator, a PI controller is designed and implemented into the servo system. Finally, the system is tested under a spinning disk to evaluate its performance.

# 5.1 System Configuration

In the system configuration shown in Fig. 5-1, the disk surface and the laser diode output facet function as an external cavity Fabry-Perot interferometer. The laser diode is used as a position sensor by employing and sensing self-mixing interferometry. A part of the light emission from the laser is reflected by the disk surface and then injected back into the laser cavity. The reflected beam is mixed with the optical field inside the cavity. This self-mixing effect causes strong modulation of the optical output power, and is dependant on the distance between the reflecting surface and the laser and is detectable by the photodiode in the laser package. Therefore, the laser diode itself can function as a direct high-accuracy position sensor and thus no external optical interferometer is required. Given the highly sensitive correspondence between the gap width and the optical power output, this laser position sensor can be used to determine the gap width with nanometer scale precision. The monitor current from the photodiode is used as the feedback signal to control the pickup and hence gap distance.

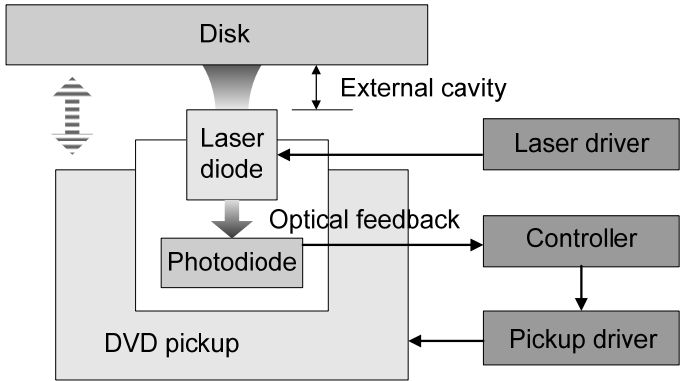


Fig. 5-1 Schematic illustration of system configuration

# 5.2 Characterization of Self-mixing Signal

The gap between a laser sensor and a surface functions as an external



cavity of the laser diode. As the gap width changes, emitting light from the laser experiences optical path difference on its way back to the laser and phase shift at the interface coupling into the cavity. Based on assumption on multiple reflections, we derive a simplified formula to model self-mixing interferometric signals. An experiment is also made to characterize the signal and compare to the simulation.

## 5.2.1 Modeling of Self-mixing Signal

By means of the self-mixing interferometric effect, laser diodes functions as a position sensor. However, to further improve integration capability and dynamic response characteristics, a length of fiber is attached to the laser diode sensor as a gap sensing probe. To characterize the feedback signal from the gap sensing probe, we consider a laser diode of length  $L_D$  connected to a single-mode fiber (SMF) of length  $L_F$  and a target surface being gap  $d$  in front of the fiber end, as shown in Fig. 5-2(a). If we assume that the reflector is only a few wavelengths away from the laser, i.e.  $d \ll L$ , the effect of the external cavity modes due to the presence of the external cavity can be ignored [43]. The coupling condition from the reflected light into the laser cavity alters the effective reflectivity of the laser emitting facet and then results in the interference with the field inside the cavity. A complex coupling factor, which consists of a phase and an amplitude factor, is employed to describe the coupling condition [44-45]. The effective reflectivity in terms of reflection coefficients and coupling coefficient is used to present an equivalent laser diode, as shown in Fig. 5-2(b), and written as

$$r_e = r_{D2} - \frac{(1 - R_{D2})}{r_{D2}} \sum_{n=1}^{\infty} [C_{n1} (-r_{D2} \cdot r_{F2} \cdot e^{i\phi_{F1}})^n + C_{n2} (-r_{D2} \cdot r_{F2} \cdot (1 - R_{F1})^2 \cdot e^{i\phi_2})^n + C_{n3} (-r_{D2} \cdot r_t \cdot (1 - R_{F1})^2 \cdot (1 - R_{F2})^2 \cdot e^{i\phi_i})^n] \quad (5-1)$$

where  $r_{D1}$ ,  $r_{D2}$ ,  $r_{F1}$ ,  $r_{F2}$ , and  $r_t$  denote the amplitude reflection coefficients of the

laser facets, fiber facets, and the external reflector, and  $R_{D2}$ ,  $R_{F1}$ , and  $R_{F2}$  denote the power reflectivity of the laser diode facet and fiber facets, respectively.

$$R_i = |r_i|^2 \quad \text{where } i = D1, D2, F1, F2, \text{ and } e \quad (5-2)$$

The phase shift  $\Phi$  resulted from the gap  $d$

$$\phi = \frac{4\pi \cdot d}{\lambda} \quad (5-3)$$

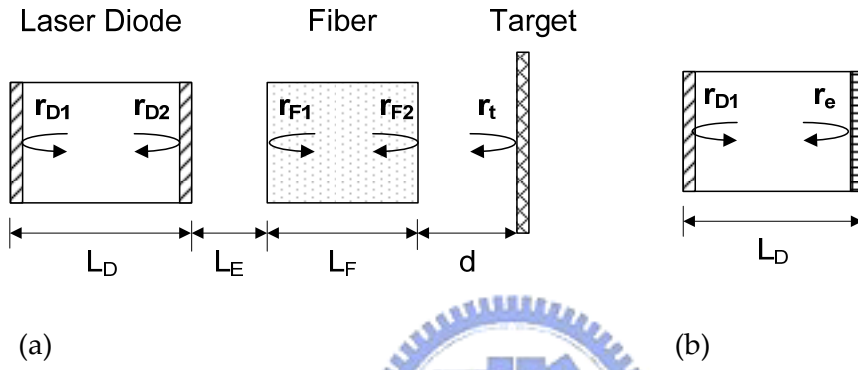


Fig. 5-2(a) Configuration of an external-cavity laser diode with a length of fiber and (b) an equivalent laser diode

If we assume the reflectivity of the target surface is much higher than that of fiber facets, i.e.  $r_t \gg r_{F1} = r_{F2}$ , and the reflectivity coefficient term decreases exponentially and much more rapidly than the coupling coefficient as the reflection increases, we assume that the reflectivity coefficient term dominates the amplitude and the coupling coefficient is a function of the spacing  $d$  and independent of the reflection. The coupling coefficient  $C_n$  represents the ratio of reflected light coupling into the laser diode at the  $n$ th reflection. Then we can derive the effective reflectivity as follows,

$$\begin{aligned} r_e &= r_{D2} - \frac{(1-R_{D2})}{r_{D2}} \sum_{n=1}^{\infty} C_{n3} (-r_{D2} \cdot r_t \cdot (1-R_{F1})^2 \cdot (1-R_{F2})^2 \cdot e^{i\phi_d})^n \\ &= r_{D2} - \frac{(1-R_{D2})C_{n3} \cdot r_t \cdot e^{i\phi_d}}{1 + r_{D2} \cdot r_t \cdot e^{i\phi_d}} \end{aligned} \quad (5-4)$$

The coupling coefficient  $C_n$  is in terms of an amplitude factor and a phase factor. The amplitude factor represents the fraction of reflected light that can couple back to the cavity and the phase factor is a phase shift at the coupling interface. Therefore, the coupling coefficient can be written as

$$C = A(d) \cdot e^{i\phi_c} = C_c \cdot (1 - e^{-2(\frac{1}{1+(2 \cdot d \cdot \lambda / (\pi \cdot \omega_0^2))^2})}) \cdot e^{i\phi_c} \quad (5-5)$$

where  $C_c$  is a proportional constant.

If we assume a constant drive current applied to the laser diode, the output power can be represented in terms of the applied current  $I$  and the threshold current  $I_{th}$

$$P_e \propto (I - I_{th}) \propto [P_C - \ln(\frac{1}{\sqrt{R_1 \cdot R_e}})] \quad (5-6)$$

where  $P_C$  is a constant.

In the case of  $r_1 = 0.99$ ,  $r_2 = 0.9$ ,  $r_3 = 0.8$ ,  $\lambda = 0.635 \mu\text{m}$  and  $w_0 = 1 \mu\text{m}$ , we calculated the power output as a function of the spacing between the laser and the target surface according to the equations derived above, as shown in Fig. 5-3.

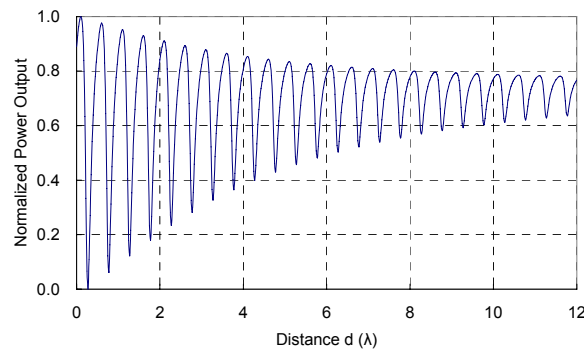


Fig. 5-3 Simulated self-mixing interferometric fringe

### 5.2.2 Experiment of Characterizing Self-mixing Signal

To generate a self-mixing signal, a silicon wafer coated with an aluminum film is placed in close proximity to the output facet of the laser diode. The laser diode is fixed in a mount attached to a piezo actuator that provides a back-and-forth motion to generate the interference signal waveforms. The experimental setup is shown in Fig. 5-4(a). According to the optical alignment method that we develop, angular alignment precision between the two surfaces is within 50  $\mu$ rad.

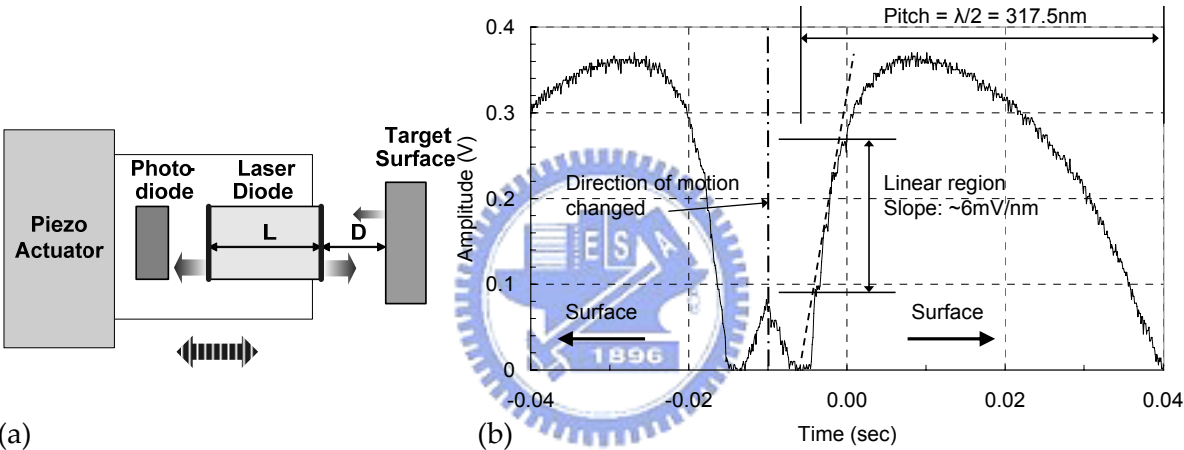


Fig. 5-4 (a) Experimental setup for feedback signal characterization and (b) measured signal from the photodiode

The monitor current of the photodiode was converted into a voltage signal and then displayed and saved by the digital oscilloscope. The measured result is shown in Fig. 5-4(b) when the operating current was 35 mA and the sampling rate was 10 ks/s. The signal is a periodic function of the distance with the maximum amplitude of 0.37 V and the pitch, a complete interferometric fringe, corresponds to a displacement of  $\lambda/2$ , which is 317.5 nm in this case. Although within a fringe, the signal varies nonlinearly with respect to the displacement, it can be approximated as a linear function in the middle half region, as indicated in Fig. 5-4(b).

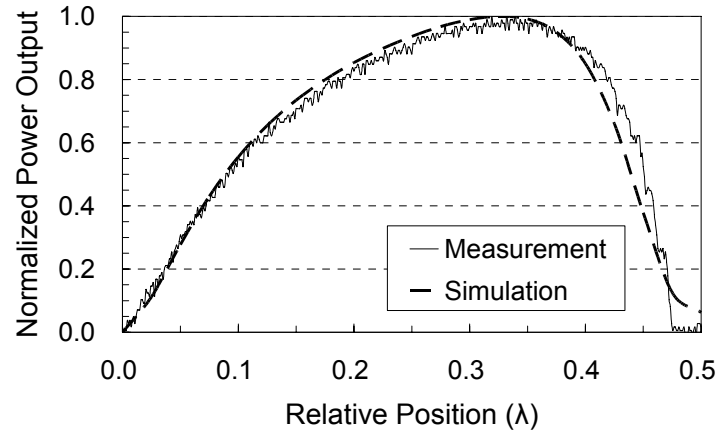


Fig. 5-5 Comparison of a measured feedback signal and a calculated self-mixing interferometric signal

Because the absolute value of output signals is highly dependent on gain of the control system, we normalize both measured and calculated signals to unity and convert them to a function of relative position in terms of wavelength. The comparison in Fig. 5-5 shows that the proposed model agrees well with the measurement. The result also clearly exhibits an asymmetry in the output power. This phenomenon results from a phase shift that the reflected field experiences as it is coupled into the laser cavity. The phase shift is dependent on the optical path difference as a result of change in the gap width. Therefore, the coupling coefficient is a complex function of the gap width consisting of an amplitude reduction term and a phase shift term. The degree of asymmetry rises with an increase of the reflectivity of the target surface. In contrast, in the absence of the target surface, the peak of the signal will locate at the relative position of  $0.25\lambda$ , i.e. the output power is a symmetric curve. Consequently, the asymmetry in the signal also identifies the moving direction of the target surface. Moreover, the slope of the signal, the sensitivity of the signal to the position variation and also the minimum displacement resolution that the sensing probe can achieve, is obtained by finding the derivative of the signal function. This characteristic implies that the deeper the slope of the signal is, the

finer the displacement resolution is. Calculated position accuracy can theoretically be as small as 2 nm, which is competitive with other control methods.

### 5.3 Fabrication of Laser Diode Sensor

This system comprised, a commercial Sanyo laser diode, DL3148-025, with  $\lambda = 635 \text{ nm}$  and a maximum output power of 5 mW mounted on a conventional DVD pickup provided by Philips, as shown in Fig. 5-6(a). The laser was driven by a Melles Griot laser diode driver, 06 DLD 203A, and the signal from the photodiode was sent to the analog-to-digital input port of a dSPACE DS1103 system in which the controller was implemented. To actuate the pickup the drive signal from the dSPACE system was converted into a current signal by the pickup drive circuit.

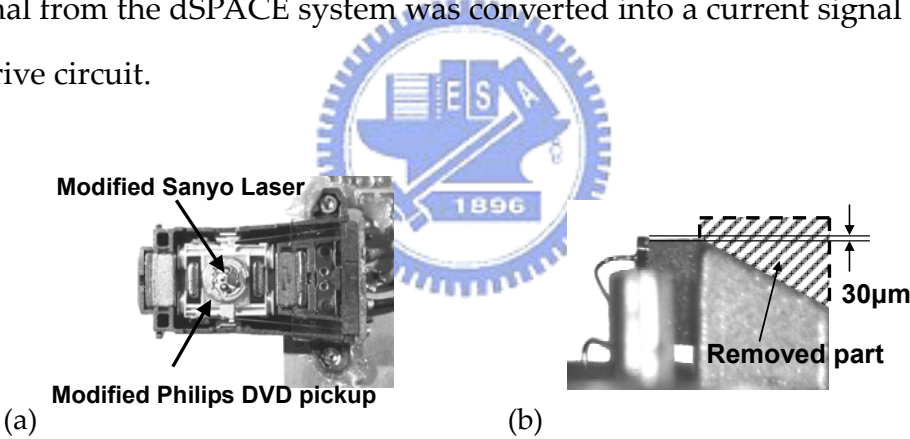


Fig. 5-6 (a) photo of the pickup with laser diode mounted and (b) side view of modified laser package

To bring the laser close to the disk surface and into the near field, some modifications were made to the commercial laser mount. Fig. 5-6 (b) shows a side view of the modified laser diode mount. In addition to the cap that was removed from the standard package, the corner of the stem was filed to obtain a 30- $\mu\text{m}$  clearance between the package and the top of the laser.

## 5.4 Approach Limit

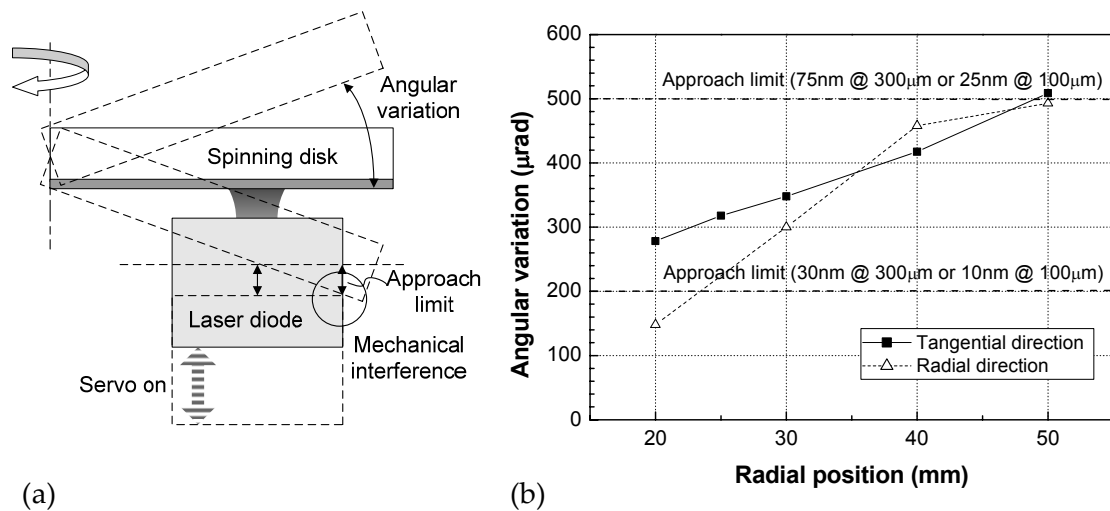


Fig. 5-7 (a) Angular variation of the disk and the laser size determines the approach limit and (b) the measured angular variation of the glass disk at different radial position along tangential and radial direction

Due to the angular variation of a spinning disk shown schematically in Fig. 5-7 (a), there will be mechanical interference between the laser diode and the disk when the laser approaches the surface. Therefore, we define the approach limit as the closest distance that the laser can achieve without mechanical interference. If the disk surface is assumed to be planar locally then from the geometry, the approach limit at a radial position is determined by the maximum angular variation in a revolution and the size of the laser. To measure the angular variation, a laser beam along the tangential or radial direction of the measured disk illuminated the disk surface and the reflected beam was projected onto a screen. Using the optical lever method, the angular variation was obtained by measuring the position of the reflected beam on the screen. From the measured angular variation of the disk at different radial positions shown in Fig. 5-7(b), the approach limit is around 75 nm when the laser size is

300  $\mu\text{m}$ . To approach to the near field, the laser size should be reduced to less than 100  $\mu\text{m}$  to achieve an approach limit of less than 25 nm.

## 5.5 Controller Design

To control outputs of a dynamic system to follow a desired state, a controller is implemented to manipulate inputs and compensate for disturbances to the system. Thus, a transfer function has to be used to describe the response of the system to inputs. Then the dynamic response of the actuator has to be analyzed. Accordingly, a PI controller and a compensator is designed and implemented into the feedback control system. An active gap control system employing a self-mixing laser sensor is realized. The system is tested under an actuated surface and a spinning disk to demonstrate the operation of the active gap control system with nanometer-scale precision.

### 5.5.1 Dynamic Response of Actuator

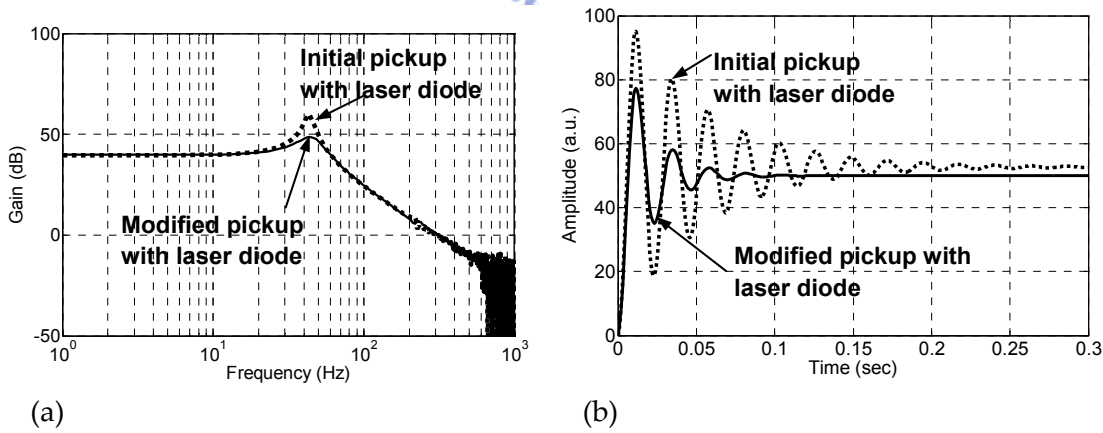


Fig. 5-8 (a) Measured open-loop frequency response of the actuator and (b) calculated step response of the actuator according to the modeling transfer function

Prior to the controller design, the open-loop frequency response of the



actuator, consisting of the pickup with the laser sensor installed and the pickup drive circuit, was measured. As shown in Fig. 5-8(a), the first resonance frequency is 42Hz and the transfer function of the actuator was modeled accordingly. Then the step response of the pickup was calculated, as shown in Fig. 5-8(b). From these results, it is clear that both the settling time and the overshoot can not meet the system requirements. The dynamic performance which determines the control precision was degraded because the laser diode doubles the weight of the moving part of the pickup.

To improve the frequency characteristics, high-viscosity resin was added in the damping area of the suspension wires of the pickup. As a result, the damping coefficient was increased by 200% which was accompanied by a 15% increase in the spring constant. Compared to the initial pickup, the response shown in Fig. 5-8(b) was obtained. The modification reduced the overshoot by 40% and the settling time by 70% while the first resonance frequency was moved to a slightly higher frequency of 43Hz.

### 5.5.2 Controller Design

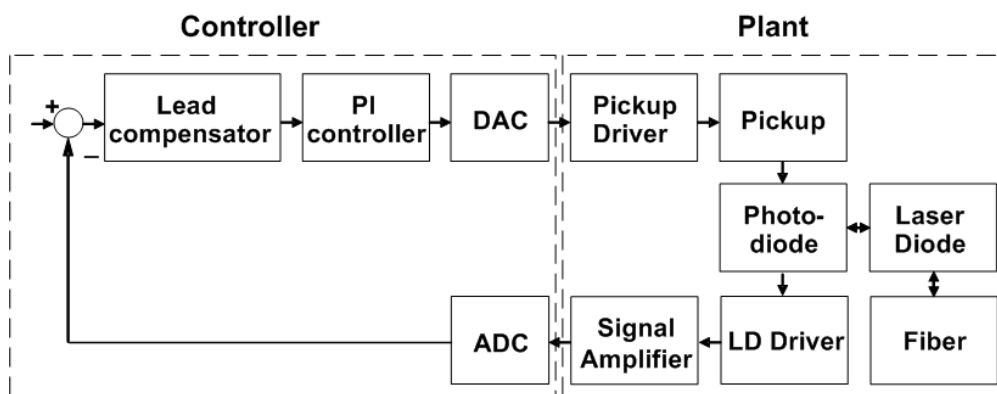


Fig. 5-9 Block diagram of the gap sensing probe system

The block diagram of the gap sensing probe system shown in Fig. 5-9

consists of two major parts, a plant and a controller. The laser driver provides the laser sensor a constant current and monitors the output power of the sensor. The light reflected from the target surface couples into the laser sensor and results in modulation of the output power. The feedback signal detected by the photodiode is amplified by a amplifier to improve the signal-to-noise ratio and then sent to the controller which is implemented in a digital system. After being processed by a proportional integral (PI) controller and a compensator, the drive signal is converted into analog form and feed back to the laser driver.

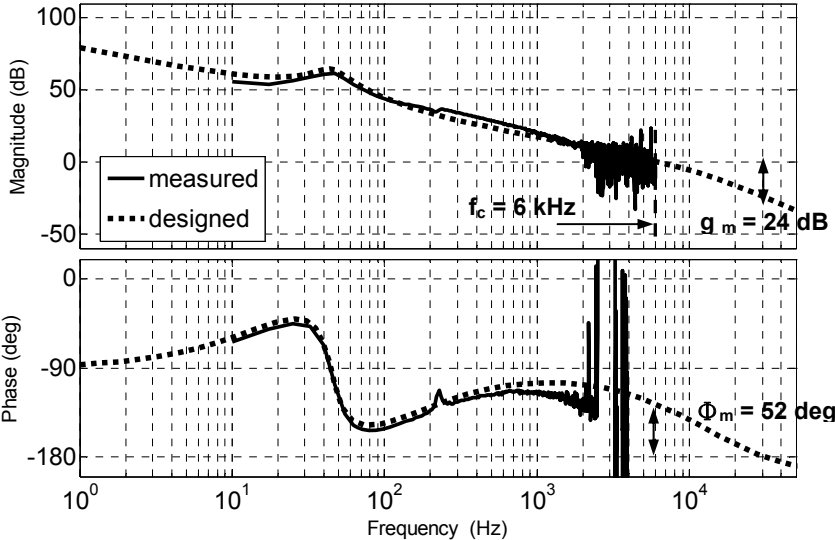


Fig. 5-10 Open-loop frequency response of the active height control system

Using a linear approximation of the feedback signal and given the frequency response of the actuator, a proportional integral (PI) controller was designed to actively control the distance of the laser from a spinning disk at a rotation speed of 1200 rpm or greater and with runout of 20  $\mu\text{m}$  or less. The controller was digitally implemented in a dSPACE DS1103 system at a sampling rate of 100 kHz. In Fig. 5-10, the dashed curve shows the open-loop dynamic characteristics of the active height controller system as designed. From the calculated data, the bandwidth is 6 kHz and the phase and gain margins are 52°

and -24dB, respectively. To evaluate the performance of the entire system, the controller was implemented in the dSPACE system and then the open-loop frequency response was measured. Compared to the designed characteristic, it is clear that the controller meets the design requirements and the frequency response agrees well with the design.

## 5.6 Operation Test

To evaluate the performance of the gap control system, we conduct two experiments, an actuated surface test and a spinning disk test. The purpose of the first experiment is to optimize the system so a simple back-and-forth movement of a surface in front of the laser sensor is activated by a piezo driver. Then the second one successfully demonstrates the operation of the system under a spinning disk.

### 5.6.1 Actuated Surface Test



To evaluate the control system and avoid having the laser diode crash into the disk surface, an actuated surface test was employed prior to operation under a spinning disk. The configuration of the actuated surface test system is shown in Fig. 5-11(a). A silicon wafer coated with an aluminum film was attached onto a piezo actuator in proximity to the laser sensor and the two surfaces were aligned to be parallel. A Polytech OFV-3001 laser interferometer was used to detect the real-time vertical movement of a spinning glass disk with an aluminum film coating at a radial position of 50 mm. The detected signal from the interferometer was sent to the piezo driver to synchronize its movement to the silicon wafer.

At a rotation speed of 1500 rpm, the vertical runout at the radial position of 50mm is measured to be around 16  $\mu\text{m}$ , as shown by the results in Fig. 5-11(a).

Due to the gains of the interferometer and the piezo actuator, the actual displacement of the silicon wafer was around 4.8  $\mu\text{m}$ . From the experimental result shown in Fig. 5-11(b), when the servo was turned on, the control system was able to precisely follow the motion of the silicon wafer and reduce the residual position error to  $\pm 1.5 \text{ nm}$ .

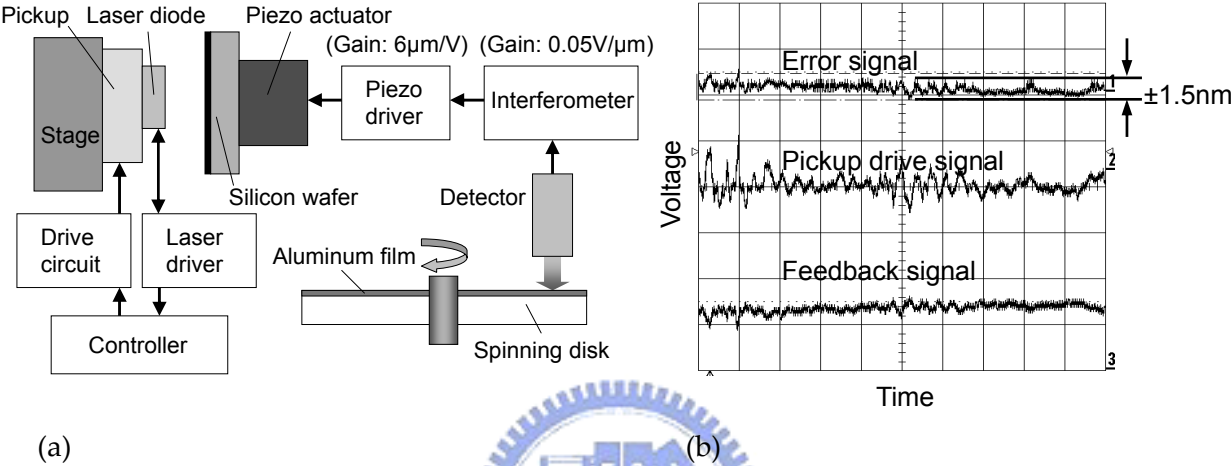


Fig. 5-11 (a) Configuration of actuated surface test system and (b) experimental results when the displacement of the actuated surface is 4.8  $\mu\text{m}$  at 1500 rpm

### 5.6.2 Spinning Disk Test

Finally, the control system was tested under a spinning disk. The configuration of the disk test system is shown in Fig. 5-12 (a). The pickup with the laser sensor installed was mounted on a stage that provided 3-axis positioning and 2-axis tilt adjustment which can compensate the angular variation of the disk surface. A 120-mm diameter glass disk coated with an aluminum film was clamped on an air-bearing spindle. In order to align the laser to the disk surface, a laser beam was used to illuminate an open window at the disk edge. Through the open window, the incident light was split into two beams at the glass-air interface. One was reflected by the interface and the

transmitted light was reflected by the laser diode. The orientation of the pickup was adjusted until these two reflected beams were parallel ensuring alignment of the laser to the disk surface.

The system was tested at rotation speeds ranging from 200 rpm to 1500 rpm. Fig. 5-12 (b) illustrates the error signal, pickup drive signal and feedback signal when the servo was in closed-loop operation at rotation speeds up to 1500 rpm. From the data, the residual position error was about  $\pm 9$  nm when the vertical runout was  $16 \mu\text{m}$  and the linear velocity at the servo radius was about 7.8 m/s. The residual error is much larger than the actuated SIL has achieved and we believe that this is due to noise in the electrical system which may yet be reduced.

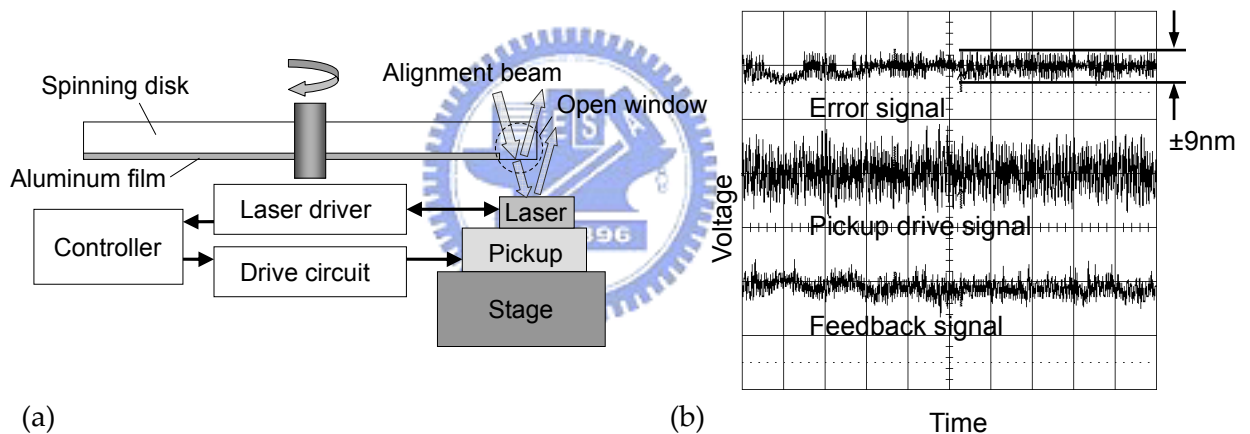


Fig. 5-12 (a) Configuration of spinning disk test system and (b) experimental results with a disk runout of  $16 \mu\text{m}$  at 1500 rpm

## 5.7 Summary

We design and characterize a laser sensor employing the self-mixing effect. Based on open cavity theory and complex coupling coefficients, we derive a simplified formula to model the self-mixing signal of the laser sensor. The experimental result is in agreement with the simulation. According to the measured signal, the theoretic position precision can be as small as  $\pm 1$  nm.

Then the laser sensor is fabricated accordingly by modifying a commercial laser diode. The approach limit, defined as the closed distance that the laser sensor can achieve, is 75 nm when the angular variation of a spinning disk is 500  $\mu$ rad and the width of the laser sensor is 300  $\mu$ m.

To design a controller for the laser sensor, we measure the dynamic response of the actuator used in our experiment. The measured open-loop frequency response of the control system fulfills the requirement of our design. The bandwidth is 6 kHz and the phase and gain margins are 52° and -24dB, respectively. The control system is then tested under an actuated surface and a spinning disk. When the spinning speed is up to 1500 rpm, the residual position error is  $\pm 1.5$  nm and  $\pm 9$  nm in the case of the actuated surface with the displacement of 4.8  $\mu$ m and the spinning disk with the displacement of 16  $\mu$ m, respectively. As listed in Table 5-1, compared to conventional near-field servo control methods, the self-mixing method has advantages of high precision as well simple and compact configuration.

Table 5-1 Comparison of near-field servo control methods

	Gap signal method (Solid immersion lens)	Shear force method (Fiber probe)	Self-mixing method (Writing probe)
Theory	Polarization change as a function of gap	Resonance change as a function of gap	Output power as a function of gap
Major Devices	1) Polarized beam splitters 2) Photodetectors 3) Biaxial actuator	1) Fiber probe 2) Tuning fork 3) Lock-in amplifier 4) Piezo actuator 5) PMT	1) Laser sensor 2) Fiber probe 3) Biaxial actuator
Scanning velocity (m/s)	5.6*	0.1**	7.9
Residual error (nm)	$\pm 1.0^*$	<1**	$\pm 1.5$

# Chapter 6 Conclusions and Future Works

## 6.1 Conclusions

To resolve issues of low efficiency, complex configuration, and low integration capability that conventional near-field light source systems encounter, in this thesis, we demonstrated a novel dual-probe near-field fiber head consisting of a straw-shaped writing probe and a flat gap sensing probe as a near-field light source for either optical or magnetic recording. We also discovered the hybrid effect that enhances transmission through a waveguide by inducing propagation modes and surface plasmons modes simultaneously as well as introduced the self-mixing effect that makes a laser diode function as a precise position sensor. Based on these two effects, this system takes advantage of fiber probes to achieve high transmission, compactness, and integration capability and opens a new avenue for near-field applications. We would like to highlight achievements and contributions this thesis made.

1. The theoretic limitation on transmission of a subwavelength aperture is a bottleneck that constrains the development of storage density. By inducing surface plasmons polaritons modes on a ridge waveguide, we discovered the hybrid effect in a subwavelength aperture that enhances the transmission by a factor of  $10^3$  higher than that of a conventional aperture. The surface plasmons polaritons modes are excited by incident light introducing a corrugation structure or attenuated total reflection and coupled into the propagation modes within the ridge waveguide. We investigated the mechanism and showed the evidence of the existence of this effect. This effect breaks the theoretic limit and provides a new approach for near-field

community.

2. According to the hybrid effect, a straw-shaped fiber probe was demonstrated to achieve a compact near-field light source with high efficiency. The power throughput of the straw-shaped fiber probe is  $10^3$  higher than that of a conventional fiber probe. Compared to the power throughput of a single C-shaped waveguide, the enhancement resulting from the hybrid effect is 3 and 1.6 in simulation and experiment, respectively. Since this high-performance straw-shaped fiber probe is simple and compact for integrating into other systems, such as actuators or magnetic heads, it is a practical solution to the demand for high density recording systems and also can be widely used for other applications, like image detecting and lithography.
3. Although the self-mixing effect of a laser diode has been used in sensing displacement, velocity, or acceleration, it was the first time to be applied in nano-scale servo control for near-field data storage systems, including detecting subwavelength position and achieving nano-scale precision. The theoretic position precision of our laser sensor can be as low as  $\pm 1$  nm; while with a proper design, we demonstrated experimental precision of  $\pm 1.5$  nm, which is competitive to and even lower than conventional methods that have bulky and complicated configuration.
4. By introducing a fiber to deliver laser beam to the medium and reflected light back to the cavity, the gap sensing probe can be easily installed on any miniaturized actuators, optical or magnetic heads for precise gap control. The simple configuration makes the gap sensing probe possible to be integrated into other systems without degrading dynamic response and feed back a sensitive and precise servo signal. A gap control system with  $\pm 1.5$  nm position precision can be easily realized by only installing the gap sensing



probe on a conventional biaxial pickup. Compared to the complicated configuration of near-field control systems, the system demonstrated provides a simple, economic, and high-performance solution.

In summary, the dual-probe near-field fiber head demonstrated is an efficient, miniaturized, and compact integrated optical head with simple and precise gap servo control. By introducing the hybrid effect and self-mixing effect, we achieve the design goal we set for a near-field light source for optical and magnetic storage systems. The innovative and novel results that this thesis presented open a new avenue to near-field transmission and servo control, and indeed make a significant contribution to near-field optics and data storage systems.

## 6.2 Future Works

Based on the achievements made, we will suggest the following topics as extensions of our research.



1. If correspondences and coupling mechanisms between existing propagation modes and surface plasmons modes can be analyzed and figured out, the energy probably can be transferred more efficiently and the overall transmission might be further enhanced accordingly. To increase the efficiency of the system, a practical solution is to focus the propagating field inside the fiber into a smaller spot on the nano-waveguide. Therefore, a fiber lens is also suggested to be inserted between the nano-waveguide and the fiber.
2. In this thesis, both the simulation and experiment on the near-field light source were conducted in the absence of the disk. However, the actual field will be altered if a surface is moving to the proximity of the exit plane of the

nano-waveguide. Therefore, the interaction between the external surface and the emitted field from a nano-waveguide should be studied to characterize the effect of the surface on the field and the transmission. In addition, although we have demonstrated the operation of our fiber head system on a spinning disk, we would like to suggest a writing test on the storage medium according to the study on the interaction between the emitted field and the disk surface.



# Reference

- [1 ] M. Mansuripur, *The Physical Principles of Magneto-optical Recording*, Cambridge University Press, United Kingdom, 1995
- [2 ] W. A. Challener, T. W. Mcdaniel, C. D. Mihalcea, K. R. Mountfield, K. Pelhos, and I. K. Sendur, "Light delivery techniques for heat-assisted magnetic recording," *Jpn. J. Appl. Phys.* 42, pp. 981-988 (2003)
- [3 ] D. W. Pohl, W. Denk, and M. Lanz, "Optical stethoscopy: image recording with resolution  $\lambda/20$ ," *Appl. Phys. Lett.* 44, pp. 651-653 (1984)
- [4 ] E. Betzig, A. Harootunian, A. Lewis, and M. Isaacson, "Near-field diffraction by a slit: implications for superresolution microscopy," *Appl. Opt.* 25, pp. 1890-1990 (1986)
- [5 ] Y. Leviatan, "Study of near-zone fields of a small aperture," *J. Appl. Phys.* 60, pp. 1577-1583 (1986)
- [6 ] E. Betzig and J. K. Trautman, "Near-field optics: microscopy, spectroscopy, and surface modification beyond the diffraction limit," *Science* 257, pp. 189-195 (1992)
- [7 ] E. Betzig, J. K. Trautman, R. Wolfe, E. M. Gyorgy, P. L. Finn, M. H. Kryder and C.-H. Chang, "Near-field magneto-optics and high density data storage," *Appl. Phys. Lett.* 61, pp. 142-144 (1992)
- [8 ] B. D. Terris, H. J. Mamin, and D. Rugar, "Near-field optical data storage," *Appl. Phys. Lett.* 68, pp. 141-143 (1995)
- [9 ] E. Betzig, S. G. Grubb, FL J. Chichester, D. J. DiGiovanni, and J. S. Weiner, "Fiber laser probe for near-field scanning optical microscopy," *Appl. Phys. Lett.* 63, pp. 3550-3552 (1993)
- [10] L. Novotny, D. W. Pohl, and B. Hecht, "Scanning near-field optical probe with ultrasmall spot size," *Opt. Lett.* 20, pp. 970-972 (1995)
- [11] W. Noell, M. Abraham, K. Mayr, A. Ruf, J. Barenz, O. Hollricher, O. Marti, and P. Guthner, "Micromachined aperture probe tip for multifunctional scanning probe microscopy," *Appl. Phys. Lett.* 70, pp. 1236-1238 (1997)
- [12] R. D. Grober, R. J. Schoelkopf, and D. E. Prober, "Optical antenna: Towards a unity efficiency near-field optical probe," *Appl. Phys. Lett.*, 70, pp. 1354-1356 (1997)

- [13] K. Sendur and W. Challener, "Near-field radiation of bow-tie antennas and apertures at optical frequencies", *J. Microsc.* 210, pp. 279-283 (2002)
- [14] P. Muhlschlegel, H.-J. Eisler, O. J. F. Martin, B. Hecht, and D. W. Pohl, "Resonant Optical Antennas," *Science* 308, pp. 1607-1609 (2006)
- [15] X. Shi, L. Hesselink, "Mechanisms for Enhancing Power Throughput from Planar Nano-Apertures for Near-Field Optical Data Storage," *Jpn. J. Appl. Phys.* 41, pp. 1632-1635 (2002)
- [16] X. Shi, R. L. Thornton, L. Hesselink, "Ultrahigh light transmission through a C-shaped nanoaperture", *Opt. Lett.* 28, pp. 1320-1322 (2003)
- [17] X. Shi and L. Hesselink, "Design of a C aperture to achieve  $1/10$  resolution and resonant transmission", *J. Opt. Soc. Am. B* 21, pp. 1305-1317 (2004)
- [18] A. V. Itagi, D. D. Stancil, J. A. Bain, and T. E. Schlesinger, "Ridge waveguide as a near-field optical source," *Appl. Phys. Lett.* 83, pp. 4474-4476 (2003)
- [19] K. Tanaka and M. Tanaka, "Simulation of confined and enhanced optical near-fields for an I-shaped aperture in a pyramidal structure on a thick metallic screen," *J. Appl. Phys.* 95, pp. 3765-3771 (2004)
- [20] D. E. Grupp, H. J. Lezec, T. Thio, and T. W. Ebbesen, "Beyond the Bethe Limit: Tunable Enhanced Light Transmission Through a Single Sub-Wavelength Aperture," *Adv. Mater.* 11, pp. 860-862 (1997)
- [21] T. W. Ebbesen, H. J. Lezec, H. F. Ghaemi, T. Thio and P. A. Wolff, "Extraordinary optical transmission through sub-wavelength hole arrays," *Nature* 391, pp. 667-669 (1998)
- [22] T. Thio, K. M. Pellerin, R. A. Linke, H. J. Lezec and T. W. Ebbesen, "Enhanced optical transmission through a single subwavelength aperture," *Opt. Lett.* 26, pp. 1972-1974 (2001)
- [23] E. Popov, M. Nevriere, J. Wenger, P.-F. Lenne, H. Rigneault, P. Chaumet, N. Bonod, J. Dintinger and T. Ebbesen, "Field enhancement in single subwavelength apertures," *J. Opt. Soc. Am. A* 23, pp. 2342-2348 (2006)
- [24] [http://www.ntmdt.com/SPM-Techniques/Principles/SNOM/Shear\\_Force\\_Microscopy\\_mode23.html](http://www.ntmdt.com/SPM-Techniques/Principles/SNOM/Shear_Force_Microscopy_mode23.html)
- [25] S. M. Mansfield and G. S. Kino, "Solid immersion microscope," *Appl. Phys. Lett.* 57, pp. 2615-2617 (1990)
- [26] S. M. Mansfield, W. R. Studenmund, G. S. Kino, and K. Osatot,

- “High-numerical-aperture lens system for optical storage,” *Opt. Lett.* 18, pp. 305-307 (1993)
- [27] B. D. Terris, H. J. Mamin, D. Rugar, W. R. Studenmund and G. S. Kino, “Near-field optical data storage using a solid immersion lens,” *Appl. Phys. Lett.* 65, pp. 388-390 (1994)
- [28] T. Ishimoto, K. Saito, M. Shinoda, T. Kondo, A. Nakaoki and M. Yamamoto, “Gap servo system for a biaxial device using an optical gap signal in a near field readout system,” *Jpn. J. Appl. Phys.* 42, pp. 2719-2724 (2003)
- [29] J.I. Lee, M.A.H. van der Aa, C.A. Verschuren, F. Zijp and M.B. van der Mark, “Development of an air gap servo system for high data transfer rate near field optical recording,” *Jpn. J. Appl. Phys.* 44, pp. 3423-3426 (2005)
- [30] T. Ishimoto, K. Saito, and T. Kondo, “Near field readout system for a high density optical ROM disc,” *Proc. SPIE* 4342, pp. 294-303 (2002)
- [31] H. A. Bethe, “Theory of diffraction by small holes,” *Phys. Rev.* 66, pp. 163-182 (1944)
- [32] C. R. Pollock, *Fundamentals of Optoelectronics*, Richard D Irwin, 1994
- [33] X. Shi and L. Hesselink, “Mechanisms for enhancing power throughput from planar nano-apertures for near-field optical data storage,” *Jpn. J. Appl. Phys.* 41, pp. 1632-1635 (2002)
- [34] H. Raether, *Surface Plasmons on Smooth and Rough Surfaces and on Gratings*, Springer-Verlag, Berlin, 1986
- [35] Tineke Thio, K. M. Pellerin, R. A. Linke, H. J. Lezec, and T. W. Ebbesen, “Enhanced light transmission through a single subwavelength aperture,” *Opt. Lett.* 26, pp. 1972-1974 (2001)
- [36] L. Martín-Moreno, F. J. García-Vidal, H. J. Lezec, K. M. Pellerin, T. Thio, J. B. Pendry, and T.W. Ebbesen, “Theory of extraordinary optical transmission through subwavelength hole arrays,” *Phys. Rev. Lett.* 86, pp. 1114-1117 (2001)
- [37] D. E. Grupp, H. J. Lezec, T. W. Ebbesen, K. M. Pellerin, and T. Thio, “Crucial role of metal surface in enhanced transmission through subwavelength apertures,” *Appl. Phys. Lett.* 77, pp. 1569-1570 (2000)
- [38] A. Degiron, H. J. Lezec, W. L. Barnes, and T. W. Ebbesen, “Effects of hole depth on enhanced light transmission through subwavelength hole

- arrays," *Appl. Phys. Lett.* 81, pp. 4327-4330 (2002)
- [39] W. M. Wang, K. T. V. Grattan, A. W. Palmer, and W. J. O. Boyle, "Self-mixing interference inside a single-mode diode laser for optical sensing applications," *J. Lightwave Technol.* 12, pp. 1577-1587 (1994)
- [40] G. Giuliani, M. Norgia, S. Donati, and T. Bosch, "Laser diode self-mixing technique for sensing applications," *J. Opt. A: Pure Appl. Opt.* 4, pp. S283-S294 (2002)
- [41] G. Plantier, C. Bes, and T. Bosch, "Behavioral model of a self-mixing laser diode sensor," *IEEE J. Quantum Electron.* 41, pp. 1157-1167 (2005)
- [42] R. O. Miles, A. Dandridge, A. B. Tveten, and T. G. Gialloenzi, "An external cavity diode laser sensor," *J. Lightwave Technol.* LT-1, pp. 81-93 (1983)
- [43] J.-Y. Kim, and H. C. Hsieh, "An open-resonator model for the analysis of a short external-cavity laser diode and its application to the optical disk head," *J. Lightwave Technol.* 10, pp. 439-447 (1992)
- [44] J.-Y. Kim, and H. C. Hsieh, "Asymmetry in the optical output power characteristics of a short-external-cavity laser diode," *IEEE Photon. Technol. Lett.* 4, pp. 537-539 (1992)

